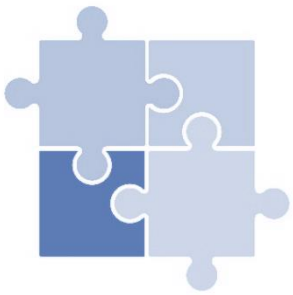

Structure-property correlation of cerium doped bismuth vanadate for energy application.

Dennis Buli Malihase

A dissertation submitted to the Faculty of Science, University of the Witwatersrand, School of Chemistry, in fulfillment of the requirement for the degree of Master of Science.

Johannesburg, 09 June 2022

DECLARATION

I declare that this dissertation is my own, unaided work. It is being submitted for the Degree of Master of Science at the University of the Witwatersrand, Johannesburg. It has not been submitted before for any degree or examination at any other University.

_____

(Signature of candidate)

_09_day_of _**June_2022**_at_**Johannesburg, Theta**__

Abstract

The demand for electricity is rapidly growing and electrochemical devices such as solid oxide fuel cells (SOFCs) have shown promising developments to mitigate this energy demand. SOFCs are devices that can convert chemical fuels such as CO, H_2 and ethanol directly into electrical energy more efficiently than any combustion process. Bismuth vanadate ($Bi_2VO_{5.5}$) is commonly doped or co-doped with transitional metals to enhance the material ionic conductivity and function as a SOFC electrolyte. The study of $Bi_2VO_{5.5}$ doped with rare-earth metals is sparsely reported and this dissertation addresses the current literature gap. In this work, the impact of doping $Bi_2VO_{5.5}$ and $Bi_2Cu_{0.1}V_{0.9}O_{5.35}$ electrolytes with different Cerium (Ce^{4+}) concentrations, using the soft chemistry (the citrate method) and the solid state method was investigated. This study focused on understanding how Ce^{4+} doping/substitution into $Bi_2VO_{5.5}$ and $Bi_2Cu_{0.1}V_{0.9}O_{5.35}$ affected these material properties such as thermal stability, phase transition behaviour and ionic conductivity.

The $Bi_2VO_{5.5}$ electrolyte synthesized using the citrate method (cit-BiVO) was determined to be a multi-phase material exhibiting the α- and β-phases at room temperature and undergoes reversible phase transitions from α → β → γ after thermal cycles. It was discovered using the Rietveld method that by doping cit-BiVO with different concentrations of Ce^{4+} using the citrate method to produce $Bi_2Ce_xV_{1-x}O_{5.5-\delta}$ electrolytes or cit-$BiCe_xVO$ samples, the β-phase was the most stable phase in cit-$BiCe_xVO$ samples at room temperature. Additionally, the ionic conductivity increased with increasing Ce^{4+} doping concentrations. However, a drop in conductivity was observed for cit-$BiCe_{0.18}VO$ sample. It was noticed that the PXRD peaks associated with the α-phase of cit-BiVO gradually disappeared with increasing Ce^{4+} doping concentrations. The Raman spectra measured at room temperature showed that Ce^{4+} ions substituted for V^{5+} lattice sites in the crystal structure. Overall, it was determined that doping cit-BiVO with Ce^{4+} at increasing concentrations improved cit-BiVO ionic conductivity but not the material phase stability since all doped samples had reversible phase transitions from α → β → γ phases as seen by the STA analyses.

The $Bi_2Cu_{0.1}V_{0.9}O_{5.35}$ electrolyte was synthesized using the solid-state method to produce sol-$BiCu_{0.10}VO$ sample which was doped with 10% mol Ce^{4+} to produce sol-$BiCu_{0.10}Ce_{0.10}VO$ sample. It was determined from the VT-EIS analyses that doping sol-$BiCu_{0.10}VO$ with Ce^{4+} destabilized and reduced the material ionic conductivity by ≈ 11% between 300 °C – 600 °C on heating. It was noted that the solid-state method favoured less formation of the α-phase (the less conductive phase) in sol-$BiCu_{0.10}VO$ and sol-$BiCu_{0.10}Ce_{0.10}VO$ samples compared to the same electrolyte $Bi_2Cu_{0.1}V_{0.9}O_{5.35}$, prepared using the citrate method to produce cit-$BiCu_{0.10}VO$ and cit-$BiCu_{0.10}Ce_{0.10}VO$ samples. It was apparent from the study that sol-$BiCu_{0.10}VO$ was already a good ionic conducting electrolyte and doping the material with 10% mol Ce^{4+} ions negatively affected the material ionic conductivity and crystal structure.

"There is still very much a need to discover and develop novel ionic conducting materials that operate at lower temperature and to characterize the connection between structure and conductivity in order to move toward the rational design of optimal materials."

Matthew T. Dunstan

Variable-Temperature Multinuclear Solid-State NMR Study of Oxide Ion Dynamics in Fluorite-Type Bismuth Vanadate and Phosphate Solid Electrolytes

Acknowledgements

I would like to express my deepest gratitude to my supervisors, Prof Dave Billing and Prof Caren Billing for their guidance, support and advice throughout this dissertation. I have learnt a great deal about research skills and ethics which I have treasured. I had the opportunity to present my dissertation as a poster at the SA-ESRF conference in Johannesburg thanks to my supervisors encouragement and motivation to push beyond boundaries.

I was part of an amazing team and made friends and colleagues who have assisted and made a positive impact into my studies. From the casually group meetings and presentations which were fruitful, I have improved my critical thinking skills, presentation and research fundamentals. To the energy materials group, Dr. Tumaini, Dr. Rudolph, Skhumbuzo, Adam, Michelle, Mathias, Gugulethu, Daniel and Masilo your presence has made this journey full of joy.

I would like to extend my gratitude and give thanks to the National Research Foundation for Center of Excellence (NRF-CoE) in strong materials and the University of the Witwatersrand for their two-year financial support because all this work would have not been possible without their funding and generosity. The funding reduced my financial burden and allowed me to focus more on my project and learning.

Contents

List of figures

List of tables

Abbreviations

SOFC – Solid oxide fuel cell

BiVO – Bismuth vanadate

BiMeVOx – Bismuth metal vanadium oxide

BiCeVO – Bismuth cerium vanadium oxide

BiCuVO – Bismuth copper vanadium oxide

BiCuCeVO – Bismuth copper cerium vanadium oxide

PXRD – Powder X-ray diffraction

EIS – Electrochemical impedance spectrum

PDF – Pair distribution function

GOF – Goodness of fit

R_{wp} – Weight profile residual

Chapter 1

General introduction.

1.1 Energy demand and alternative energy resources.

Electricity is vital for human activities and necessary to maintain our modern standard of living. Since its discovery in 1879, electricity has driven innovative technologies and improved the quality of life[1]. The global consumption of electricity was estimated to be ≈ 606.7 x 10^{18} J in 2015 and projected to grow by 28% in 2040. The demand for electricity is rapidly increasing in developing countries due to new technologies to drive economic and sustainable growth[1]. The International Energy Agency (IEA) reported that fossil fuel-energy will dominate for decades to come as the primary energy resource and estimated to provide nearly 58% of the global electricity in 2040. Meanwhile renewable energy is estimated to provide more than 31% of the global electricity by 2040 and the remaining 11% of the global electricity will be generated from nuclear and other energy resources[1].

Fossil fuel-energy production has been an ongoing social, political and environmental debate due to the significant contribution of greenhouse gases and associated environmental impacts it assets. Fossil fuels are finite and expected to diminish quicker if the current high consumption of electricity continues[1]. In recent years, fossil fuel restrictions have been implemented to carefully manage the usage and production of electricity, however the high price and demand for electricity threatened this mitigation strategy[1]. Fig 1.1 shows the estimated natural gas, coal and oil reserves left to produce electricity at the current consumption levels according to worldometer..

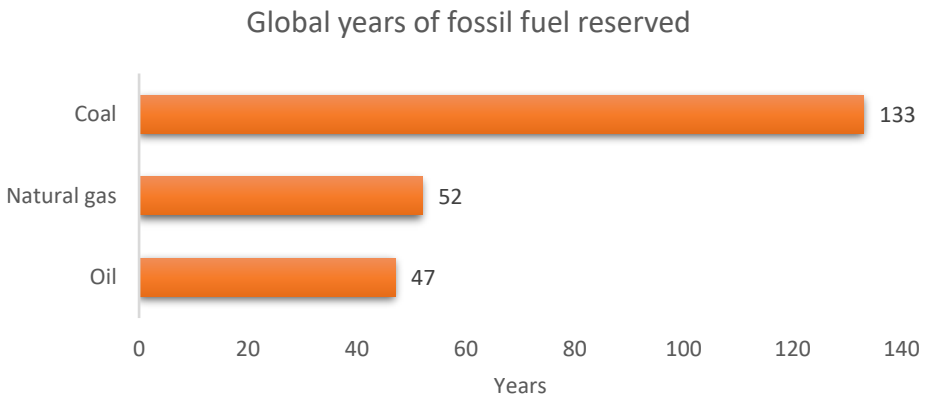

Figure 1.1: Estimated global coal, natural gas and oil reserved measured as the number of years[2].

The estimated reverse years can change at any moment based on the discovery of new reserves which makes it difficult to accurately predict the reserved years because factors such as the geographical region where the reserves are located and the possible recoverability constantly change[18]. Renewable energy such as solar, wind and hydropower have captured the global interest to produce sustainable and reliable electricity that will potentially replace fossil fuels. The advantages of renewable energy include the reduction in the environmental impact of electricity transmission from power plants, air pollution and the dependence of imported fuels[1]. To meet the current electricity demand, renewable energy must have high capacity, stable performance, and operation as well as cost-effectiveness. With the current human population growing at 1.07% per year, the demand for electricity is increasing and electrochemical devices such as solid oxide fuel cells (SOFCs) have shown promising developments to assist in managing the energy crisis[1].

1.2 Solid oxide fuel cell (SOFC).

At present, ionic conductors that can operate at temperatures between 400 °C - 600 °C have become a prominent research topic for SOFCs[3]. Common SOFCs conductors such as Yttrium stabilised Zirconia (YSZ) have optimal operation at temperatures > 1000 °C[3].. SOFCs are devices that can power a vehicle, generate medium to large scale power, provide off-grid power and micro combined heat (CHP) energy[1]. They consist of two electrodes (anode and

cathode) separated by an electrolyte material (ionic conductors) covered with sealing materials (if required) and a fuelling distribution system[5]. The electrolyte is one of the major component in SOFC and Yttria stabilised zirconia (YSZ) is a frequent example that typically operates at temperatures above 900 °C[5].The electrolyte material transports oxide ions (O^{2-}) from the cathode to the anode to react with fuel (e.g. H_2, methanol and biomass) which generates electricity and CO_2 depending on the type of fuel used[6]. Fig 1.2 shows the general working principle of a SOFC.

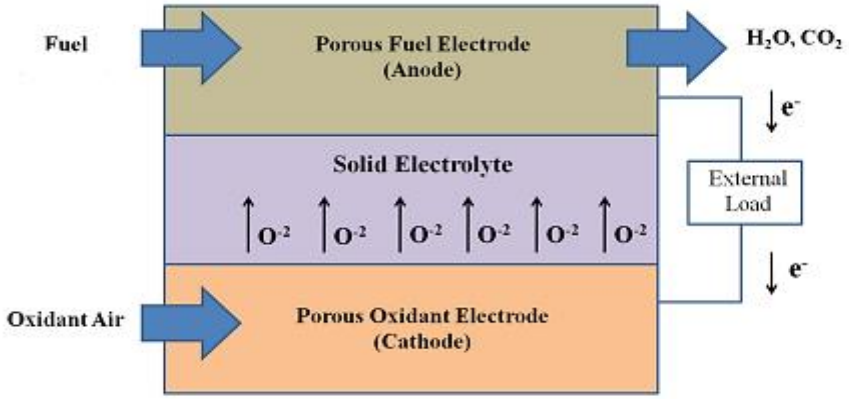

Figure 1.2: The functioning process in a SOFC[6].

For SOFCs to operate efficiently, high oxygen ion flux and migration is required which is usually achieved at relatively higher temperatures (> 800 °C)[4]. At such temperatures, performance degradation, corrosion, chemical reaction and thermal expansion mismatch between various SOFC components occurs[7]. Therefore by designing electrodes with high activity polarization resistance and reduced ohmic resistance[8] in addition to increasing the number of oxygen vacancies in the electrolyte material will reduce SOFC's operating temperature while maintaining efficiency. However, excessive vacancies in an electrolyte decreases the material ionic conductivity due to the association of the oxygen vacancies with interstitial oxygen ions. Therefore oxygen vacancies are preferred over maximum oxygen vacancies[9].

SOFCs are largely pollutant-free fuel devices that reduce the dependence on coal and oil to produce electricity.[1] They offer many advantages over conventional energy power generation systems such as low levels of toxic NOx and SOx gas emissions, high efficiency, fuel adaptability and no external reformer systems are required[10]. A global challenge for the current generation is to produce electricity that is sustainable, cost less to manufacture and does not damage the environment and devices like SOFCs are part of the solution.

The objective of this project was to synthesis an electrolyte material that exhibits high ionic conductivity at temperatures (400 °C - 600 °C) and Bismuth vanadate ($Bi_2VO_{5.5}$) was the proposed material. The focus was to stabilise the most conductive phase of $Bi_2VO_{5.5}$ by substituting vanadium (V^{5+}) sites with Cerium (Ce^{4+}) ions at different concentrations using the citrate method. The second objective was to synthesis a well-known electrolyte $Bi_2Cu_{0.1}V_{0.9}O_{5.35}$ and dope it with 10 % mol Ce^{4+} using the solid state method. This project involved investigating the impact of Ce^{4+} in $Bi_2VO_{5.5}$ and $Bi_2Cu_{0.1}V_{0.9}O_{5.35}$ materials and how doping would affect these material properties, in particular the thermal stability, phase transition behaviour and ionic conductivity.

1.3 Bismuth vanadate ($Bi_2VO_{5.5}$).

Bismuth oxide (Bi_2O_3) exhibits various interesting chemical and physical properties e.g. bismuth tungstate (Bi_2WO_6) and bismuth molybdate ($Bi_2Mo_2O_9$) act as catalysts for the oxidation and ammoxidation of alkenes and unsaturated hydrocarbons[11].Meanwhile, $Bi_2Mo_2O_9$ thin films can be used as gas sensors for ketones and alcohol. The gamma phase (γ) of thin-film bismuth niobite ($BiNbO_4$) and bismuth vanadate ($Bi_2VO_{5.5}$) are good photoconductors[11].

$Bi_2VO_{5.5}$ is known to exhibit three reversible polymorphic phases. The α-phase (monoclinic) exists below 450 °C, the β-phase (orthorhombic) exists between 450 °C to 570 °C and the γ-phase (tetragonal) exists above 570 °C. The γ-phase of $Bi_2VO_{5.5}$ has found extensive application in SOFCs and rechargeable lithium batteries[4]. The β-phase and γ-phase of $Bi_2VO_{5.5}$

consist of $(Bi_2O_2)^{2+}$ layers sandwiched between $(VO_6)^{2-}$ sheets (see fig 1.3). The Bi-O layer forms asymmetric square pyramidal geometries while the V-O layer forms octahedra which contain O^{2-} vacancies to maintain electroneutrality[4].

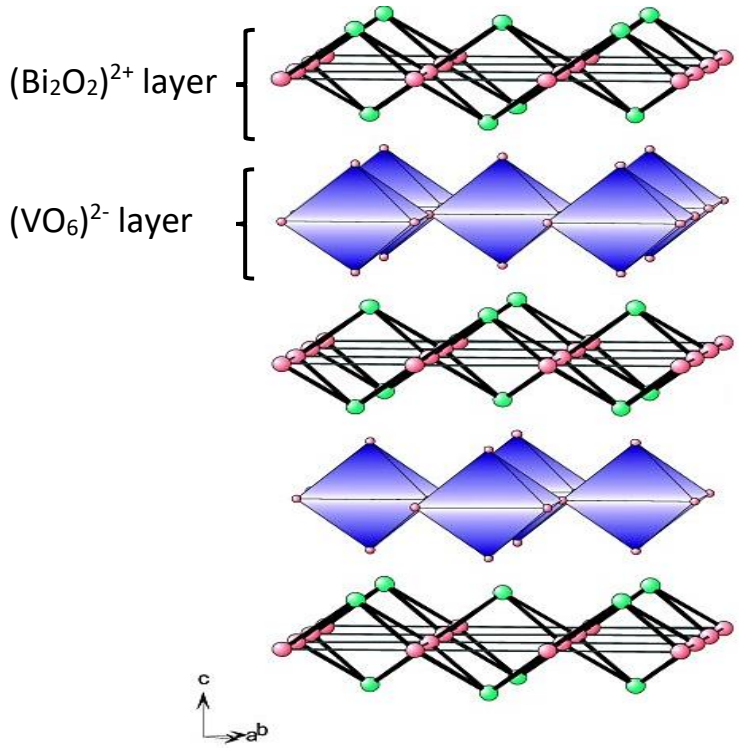

Figure 1.3: The crystal structure of the β-phase of $Bi_2VO_{5.5}$[13].

The edges of the $(Bi_2O_2)^{2+}$ layers in the β-phase structure are shared by BiO_4 groups in which the Bi^{3+} ions are positioned at the apex of the square pyramid and the four oxygen atoms form the base of the plane[4]. At lower temperatures, the oxygen vacancies are associated with vanadium atoms forming alternating vanadium-centred octahedral and tetrahedral structures. Meanwhile, at higher temperatures (>570 °C), the oxygen vacancies are mostly vanadium-centred octahedral structures resulting in the material high ionic conductivity[4].

Previous studies have shown that below 550 °C, $Bi_2VO_{5.5}$ is metastable and decomposes to $BiVO_4$ (α-phase) and $Bi_{3.5}V_{1.2}O_{8.25}$ after 12 days and completely forms $BiVO_4$ after 7 weeks[3]. The γ-phase of $Bi_2VO_{5.5}$ is the most conductive phase with ionic conductivity reaching 3×10^{-1} S cm^{-1} at ≈700° C, which is higher than other well-known electrolytes such as $(Bi_2O_3)_{0.8}(Er_2O_3)_{0.2}$ (EDB), $(ZrO_2)_{0.92}(Y_2O_3)_{0.08}$ (YSZ), $(CeO_2)_{0.85}(SmO_{1.5})_{0.15}$ (SDC) and $La_{0.8}Sr_{0.2}Ga_{0.8}Mg_{0.115}Co_{0.085}O_3$ (LSGMC) at 700 °C[3]. Fig 1.4 shows the measured ionic

conductivity of $Bi_2VO_{5.5}$ as a function of temperature against other potential SOFCs electrolytes. Notice how $Bi_2VO_{5.5}$ undergoes phase transition as the temperature increases which affects the material conductivity.

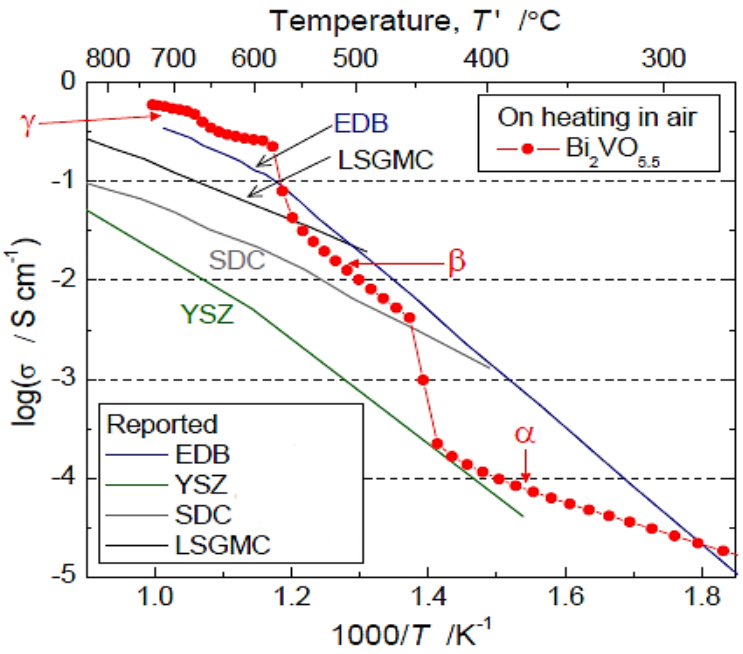

.

Figure 1.4: Conductivities of shown electrolytes obtained at a heating rate of 1 K/min [3].

The crystal structure of $Bi_2VO_{5.5}$ is strenuous to solve due to the difficulty of determining the position of the oxygen atoms using X-ray diffraction since the X-rays scattered from the metal ions overshadow the scattering of the surrounding oxygen atoms[14]. The atomic arrangements of Bi-O and V-O layers in distinct phases are shown in fig 1.5 and are drawn based on precise crystalline data. As shown in the diagrams, the oxygen vacancies in the γ-phase are positioned at the edges, sharing oxygen octahedrons within the V-O layers. Meanwhile the β- and α-phases form far more complex and disordered trigonal bipyramidal structures due to the ordering of oxygen vacancies[3].

Monoclinic (α-phase) $Bi_2VO_{5.5}$

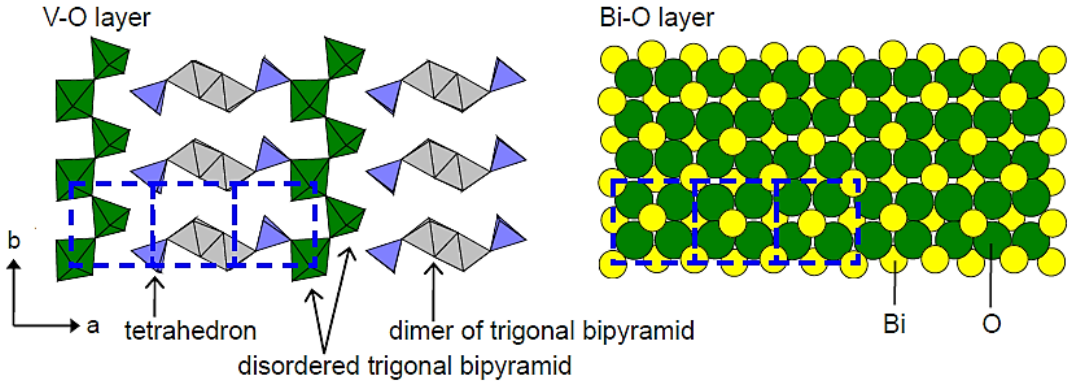

Orthorhombic (β-phase) $Bi_2VO_{5.5}$

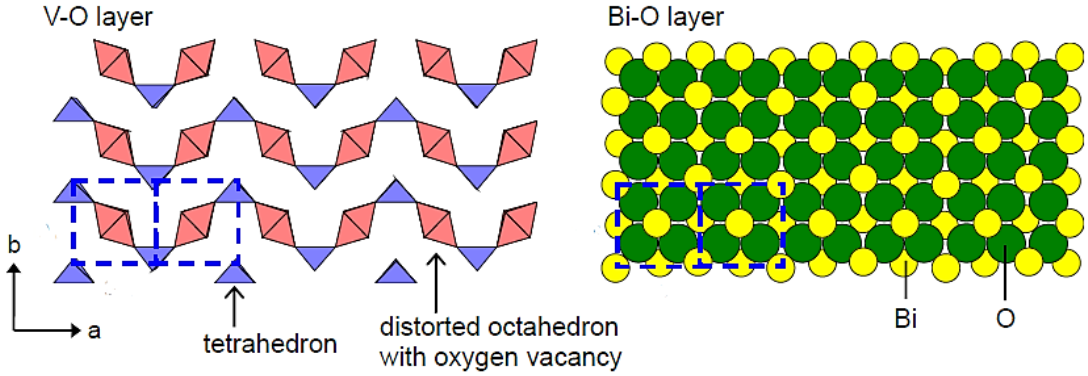

Tetragonal (γ-phase) $Bi_2VO_{5.5}$

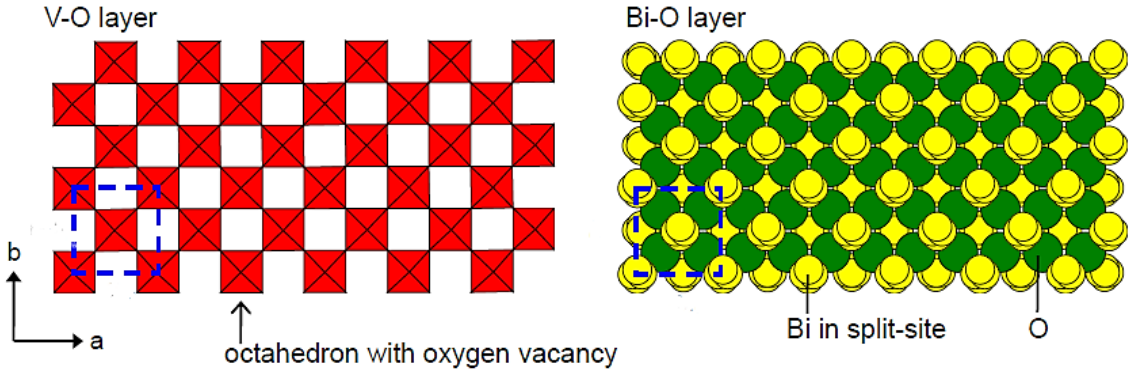

Figure 1.5: Atomic arrangements of the Bi-O and V-O layers in $Bi_2VO_{5.5}$ in different phases. The blue boxes represent the cell unit lattice parameter[3].

The VO_x polyhedral structure in $Bi_2VO_{5.5}$ plays a vital role in the migration of oxide ions between the V-O and Bi-O layers[12]. During a phase transition from the α → β phases, the dimeric V-O bipyramidal coordination connected to the VO tetrahedral breaks and form oxygen vacancies that closely resemble a distorted perovskite-like structure. The phase transition from the β → γ phases involves the rearrangements of the oxide ion network within the distorted perovskite-like structure. The arrangement of the oxygen vacancies in the V-O layer in the α-phase are far more complicated than that of the β-phase[15]. The β → γ phase transition not only involves the V-O layer transformation but also the oxygen atomic positions in the Bi-O layer merge and Bi sites split as indicated in fig 1.5[15].

Numerous literature studies have shown that substituting (or doping) bismuth or vanadium sites in $Bi_2VO_{5.5}$ with a different metal ion significantly improves the material ionic conductivity[3] forming a large family of electrolytes known as the BiMeVOx (Bi-bismuth, Me-metal ion, V-vanadium, OX-oxide). A study was carried to investigate attributes that affected BiMeVOx ionic conductivity using Me: Ti, Zr, Sn, and Pb at 0.2 mol dopant concentration and it was found that conductivity decreased in the order Ti > Sn > Zr > Pb at 227 °C[3]. There are various arguments about which factors affect BiMeVOx conductivity and whether the nature of the substituent or the oxygen vacancy concentration or some other variable stabilises the most conductive phase in this materials[3].

Amongst the BiMeVOx materials, the γ-phase of $Bi_2Cu_{0.1}V_{0.9}O_{5.35}$ is the most conductive material known to date synthesized via the solid-state method[3]. Unlike the $Bi_2VO_{5.5}$ electrolyte, $Bi_2Cu_{0.1}V_{0.9}O_{5.35}$ does not undergo phase transitions upon heating as shown in Fig 1.6. Previous studies have indicated that around 500 °C $Bi_2Cu_{0.1}V_{0.9}O_{5.35}$ undergoes a phase transition from a pseudo-tetragonal (γ'-phase) to tetragonal (γ-phase), hence the slight discontinuity in the material conductivity at 500 °C (see Fig 1.6). However, there is still insufficient evidence to comprehensively prove such a claim[3].

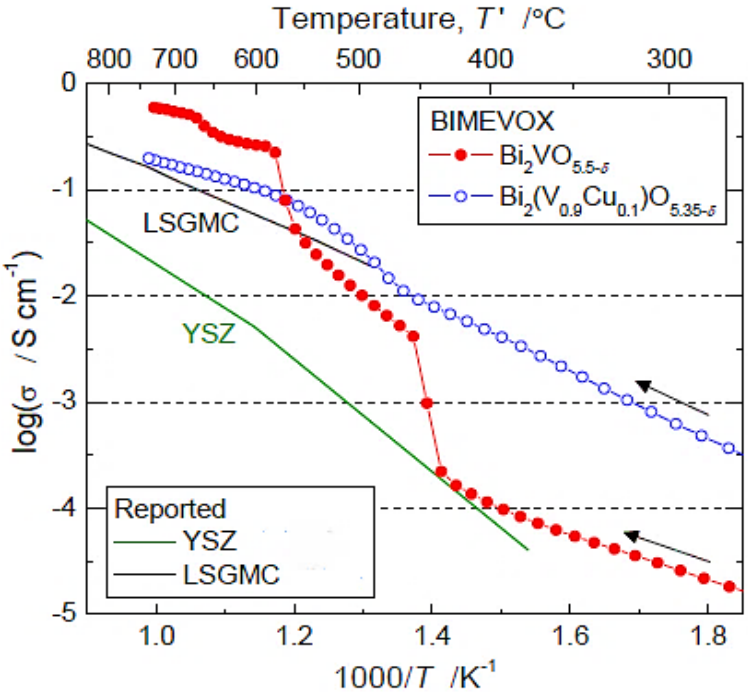

Figure 1.6: Conductivities of shown electrolytes measured at a heating rate of 1 K/min [3].

The long-term phase stabilities of BiMeVOx is notably short with the γ-phase of $Bi_2Cu_{0.1}V_{0.9}O_{5.35}$ and $Bi_2Co_{0.1}V_{0.9}O_{5.35}$ exhibiting a significant time-dependent conductivity due to the slow phase transition from the γ → α-phase (the least conductive phase)[3]. For practical use of BiMeVOx as SOFC electrolyte, the most conductive phase must be stable over a wide range of lower temperatures.

1.4 Outline of the study.

Electrolytes with high ionic conductivity at low temperatures are commonly Bi^{3+} or Ce^{4+} based electrolytes. However, under low oxygen partial pressure doped Ce^{4+} electrolytes exhibit mixed ionic and electronic conductivity due to the reduction of Ce^{4+} to Ce^{3+} meanwhile Bi^{3+} based electrolytes decompose to metallic bismuth[8]. Ce^{4+} has become an attractive ion to dope electrolytes due to the element corrosion resistant[16].

CeO_2 is a traditional electrolyte with good thermal stability, high oxide ion conductivity between 400 °C – 600 °C and an effective kinetic stabilizer[17]. In this study, the Kroger-Vink notation below shows that the γ – and β-phases of $Bi_2VO_{5.5}$ contains two inherent oxygen vacancies as illustrated by equation (1). By doping Ce^{4+} into V^{5+} sites as proposed, the material would result in additional oxygen vacancies as desired in this work (see equation 2). Thus Ce^{4+} was selected as a suitable dopant to improve $Bi_2VO_{5.5}$ conductivity.

Kroger-Vink notation

$$Bi_2O_3 + V_2O_5 \rightarrow 2Bi_V'' + 3O_O^x + 2V_O^{\cdot\cdot} \quad (1)$$

$$CeO_2 + Bi_2VO_{5.5} \rightarrow 2Bi_{Bi}^x + Ce_V' + 2O_o^y + 3.5V_{\ddot{O}} \quad (2)$$

$V_O^{\cdot\cdot}$ represents oxygen vacancies while Bi_v'' and Ce_v' represents metal-metal substitutions. O_o^y and Bi_{Bi}^x represents oxygen and bismuth atoms in their regular positions in the crystal structure.

1.5 Aims and objectives.

- Synthesis of $Bi_2VO_{5.5}$ using the citrate method (cit-BiVO).
- Doping of cit-BiVO with Ce^{4+} at different concentrations using the citrate method to produce cit-$BiCe_xVO$ ($0.04 \leq x \leq 0.28$) samples.
- Determine the crystalline phases present in cit-BiVO and cit-$BiCe_xVO$ samples as a function of temperature.
- Study the crystal structures of cit-BiVO and cit-$BiCe_xVO$ to reveal the impact Ce^{4+} doping has induced.
- Compare the ionic conductivity of cit-BiVO and cit-$BiCe_xVO$ at various temperatures.
- Compare the thermal stability and phase transition behaviour of cit-BiVO and cit-$BiCe_xVO$.
- Synthesis of $Bi_2Cu_{0.10}V_{0.90}O_{5.35}$ using the solid-state method (sol-$BiCu_{0.10}VO$).

- Doping of sol-$BiCu_{0.10}VO$ with 10 % mol Ce^{4+} using the solid-state method to produce sol-$BiCu_{0.10}Ce_{0.10}VO$ sample.
- Compare the conductivity and phase transition behaviour of sol-$BiCu_{0.10}VO$ and sol-$BiCu_{0.10}Ce_{0.10}VO$ samples at different temperatures.
- Compare the thermal stability and phase transition behaviour of sol-$BiCu_{0.10}VO$ and sol-$BiCu_{0.10}Ce_{0.10}VO$.

1.6 Hypothesis and questions.

A hypothesis was made that "Doping/substituting Ce^{4+} into cit-BiVO and sol-$BiCu_{0.10}VO$ samples will improve the material structural stability and ionic conductivity" and this were the essential questions for this project:

- Does doping cit-BiVO with Ce^{4+} using the citrate method improve the sample conductivity?
- Will Ce^{4+} stabilize or destabilize the crystal structure of cit-BiVO?
- Which phase transitions occur on thermal cycles of cit-BiVO versus cit-$BiCe_xVO$?
- Will Ce^{4+} substitute for Bi^{3+} , V^{5+} or Cu^{2+} lattice sites or deposit on the surface of cit-BiVO and sol-$BiCu_{0.10}VO$ samples as coating?
- Does doping sol-$BiCu_{0.10}VO$ with 10 % mol Ce^{4+} improve the material ionic conductivity?
- Which phase transitions occur on thermal cycles of sol-$BiCu_{0.10}VO$ versus sol-$BiCu_{0.10}Ce_{0.10}VO$?

Chapter 2

Basic principles underlying method of analysis used.

2.1 Powder X-ray diffraction (PXRD).

Powder X-ray diffraction (PXRD) is a common tool used to determine the crystal phases present in solid materials. It is a frequent technique used for the study of powdered samples which contains a large number of small, randomly oriented crystals[1]. Crystalline powders consist of periodic arrays of atoms or ions with interatomic spacing of around 100 pm. When an incident X-ray radiation interact with a crystal sample, X-rays scattering occurs resulting in destructive and constructive interferences referred to as diffraction[1]. For diffraction to take place the incident wavelength must have the same order of magnitude to the interatomic spacing between atoms[2].

For scattered X-ray beams (C and H) to interfere constructively (see fig 2.1), the X-ray beam H must travel further than beam C which is equal to an integral multiple of the wavelength (nλ)[1]. The difference in the path length between these beams can be calculated using a trigonometrical function; 2d sinθ. Therefore, for constructive interference to occur the scattered waves C and H must be defined as nλ = 2d sin θ known as Bragg's law[1].

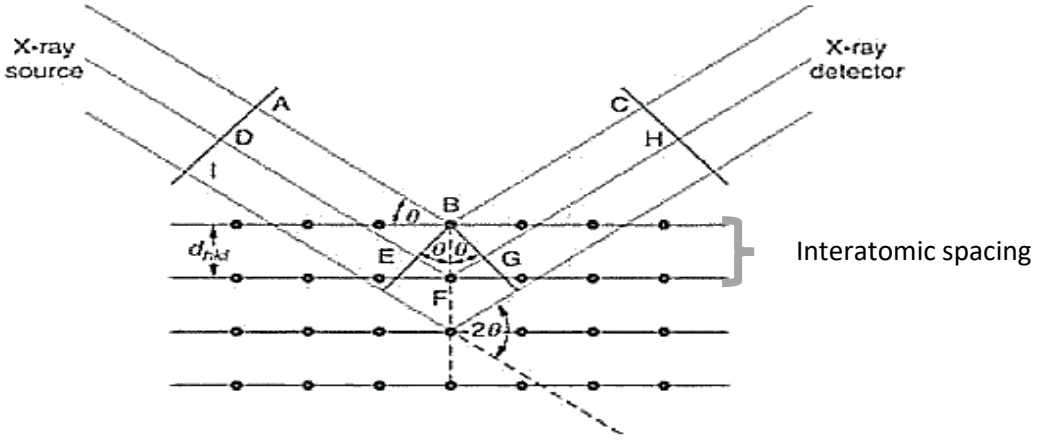

Figure 2.1: The interaction of a crystalline material with x-rays[1].

According to Bragg's Law, the angle of reflection/diffraction depends on the wavelength, the interatomic spacing and the dimensions of the unit cell[1]. The intensities of the reflected beams depend solely on the nature of the atoms, heavier atoms have a greater number of electrons thus exhibit stronger scattering than light atoms. The positions of the atoms within the unit cell also contribute to the unique X-ray diffraction patterns[1].

The PXRD instruments employed in this study had a fixed X-ray wavelength and the data was collected by an automatic diffractometer which recorded the angle and intensity of the diffracted beams into a 1D diffraction patterns. The 1D diffraction patterns allowed phase identification, lattice parameter determination and structural refinement (Rietveld) easy to process. Although 2D patterns contain far more valuable information than 1D patterns, 2D patterns require unique interpretation and data collection procedures and expensive detectors[1]. Fig 2.2 shows the difference between a 1D vs 2D XRD patterns.

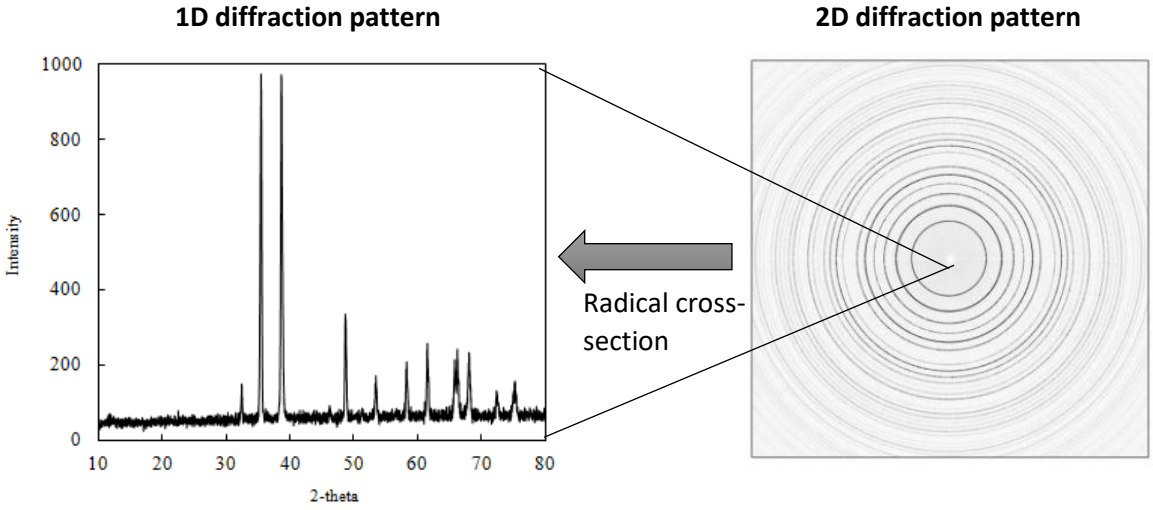

Figure 2.2: 1D and 2D powder diffraction patterns[3].

2.2 The Rietveld method.

The Rietveld method is a powerful tool for structural refinement of polycrystalline materials. As a result of the overlapping of X-ray diffractions in powder patterns, the Rietveld method involves curve-fitting procedures that model the entire diffraction pattern to refine the crystal

structure according to the measured PXRD data[1]. The least-square refinement technique is the most common refinement where the difference between the measured PXRD and the calculated Rietveld pattern are minimized rather than individual reflections[1]. Fig 2.3 shows an example of a Rietveld refinement of $Bi_2V_{1-x}Ti_xO_{5.5-(x/2)-\delta}$ (x = 0.125).

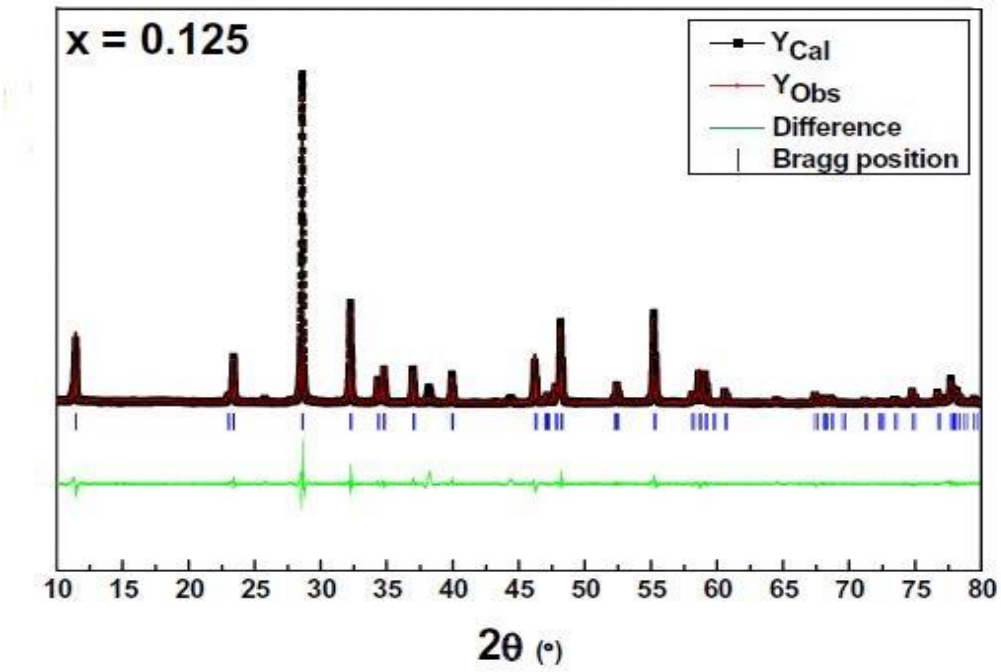

Figure 2.3: Rietveld refined PXRD pattern for the β-phase of $Bi_2Ti_xV_{1-x}O_{5.5-(x/2)-\delta}$ (x = 0.125) [4].

The weighted profile residual (R_{wp}), indicates the difference between the observed and calculated patterns and thus measure how well the crystal structure fits the measured data and is calculated as follows[1]:

$$R_{wp} = \left\{ \frac{\sum_i W_i \left(Y_{i(obs)} - Y_{i(cal)} \right)^2}{\sum_i W_i \left(Y_{i(obs)} \right)^2} \right\}^{\frac{1}{2}}$$

$$Y_{i(cal)} = \sum_k I_k \Omega(2\theta_i, 2\theta_k)$$

$Y_{i\ (cal)}$ represents the calculated intensity of a given reflection in the diffraction pattern meanwhile I_K is the integrated intensity of the K_α reflections. Ω ($2\theta_i$, 2θk) is a function that

describes an individual peak and W_I is the weight of an individual point which is typically $1/Y_{i(obs)}$.

The R_{wp} value is used as a guide to check the quality of the refinement performed and the lower the value the better the structural determination[1]. However, this value should be used with caution since some structures with low R_{wp} value can be incorrect. In this study, Rietveld refinement was conducted using Topas v5.0 and Topas v 6.0 academia programs.

It is overly critical to measure a good PXRD pattern for better Rietveld refinement since the geometry set for the diffractometer, sample preparation, sample thickness, the quality of the instrument alignment and calibration, wavelength and slit sizes all play a key role. If a poorer PXRD measurement is performed then no amount of Rietveld refinement would yield sensible results. Long data measurements amplify the low peak intensities and using a smaller slit at high angles and a wider slit at low angles also improve PXRD data[14].

The PXRD patterns in this study were complex with high degree of peak overlapping and V^{5+} fluorescence which made it difficult to resolve peaks and accurately refine each sample crystal structure. The background was re-estimated several times during the Rietveld refinement to improve peak fitting. The synchrotron data obtained had excellent signal-to-noise discrimination and the peaks were more sensitive to structural disorders.

A successful Rietveld refinement depends on the peak shapes of the pattern, if the peaks are poorly described then the refinement will not be satisfactory. The pseudo-Voigt function which is a linear combination of Lorentzian and Gaussian function is the most used analytical peak-shape function[14]. It describes the symmetrical part of an PXRD peak quite well in addition to the asymmetric peak due to the axial divergence of the diffracted beams.

Topas v5.0 program contained the pseudo-Voigt function and the Goodness of fit (GOF) and Rwp values were used to access the refinement performed. The rule of thumb was that before any Rietveld refinement was performed, the difference between the positions of the

observed and calculated peaks must match well[14]. Fig 2.4(a) shows an example of a good fit between calculated and observed peak shape and fig 2.4(b)/(c) shows the effect of intensity difference where the calculated peak is too high or too low at the peak center. The effect of incorrect peak width can be seen in fig 2.4(d)/(e) with significant mismatch of the background line. Fig 2.4(f) shows the effect of peak asymmetry and the two peaks at fig 2.4 (g)/(h), shows the effect of a 2θ mismatch which is commonly caused by peak reflection overlap. fig 2.4 (i)/(j) shows the effect of misfits caused by incorrect crystal structure parameters.

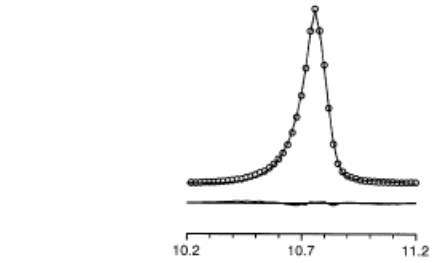

(a)

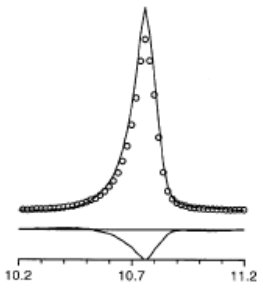

(b)

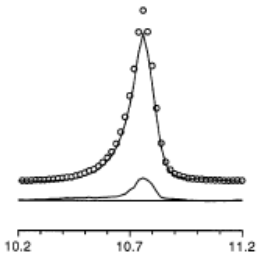

(c)

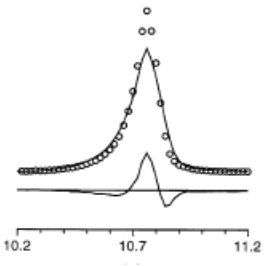

(d)

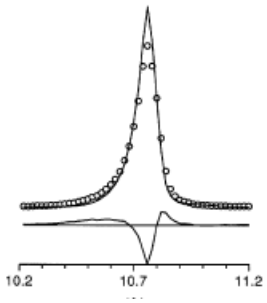

(e)

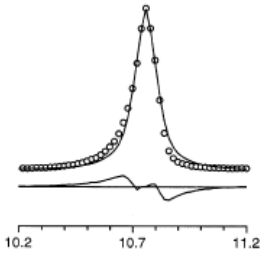

(f)

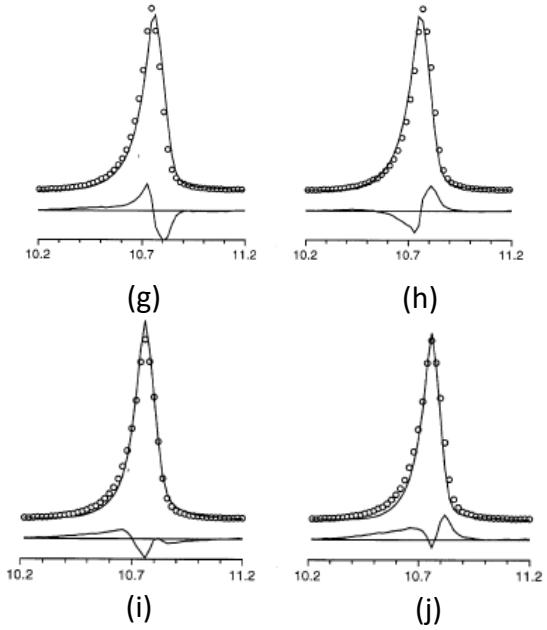

Figure 2.4: Different peak-shape profile mismatch. Observed data (circles), calculated data (line) and difference (bottom line).

During the Rietveld refinement, it is advisable to start refining the lattice parameters, unit scale and unit angles first before refining any atomic position or thermal parameter if necessary. Heavier atoms must be refined first then lighter atoms next.

2.3 Electrochemical impedance spectroscopy (EIS).

Impedance spectroscopy (IS) evaluates the electrical properties of materials such as; semiconductors, ionic and mixed electronic materials[1]. IS measures the ability of a circuit to prevent the flow of charge by a complex network of circuits[1]. Alternating current electrochemical impedance spectroscopy (AC-EIS) measures impedance by applying alternating voltage or current which produces an alternating current which is shifted in phase from the voltage by an angle θ. The phase difference is due to the sample delay in the electrical response to the applied voltage[1]. Fig 2.5 shows the alternating waveforms of voltage (V) and current (I) in AC-EIS measurement. V_0 and I_0 represent the amplitude of the voltage and current respectively.

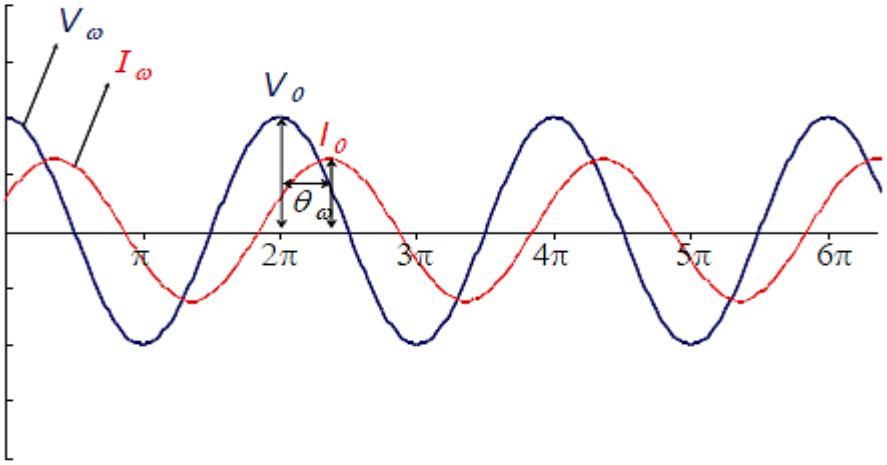

Figure 2.5: Waveforms of the voltage and current produced during AC-EIS[1].

The standard definition of impedance Z (ω) is given by:

$$Z(\omega) = \frac{V_\omega}{I_\omega} = \frac{v(t)}{i(t)}$$

V (t) = V_0 sin (ωt) represent the applied monochromatic signal frequency at ω/2π and I (t) = I sin (ωt + θ) is the measured current. Θ is the phase difference between the current and voltage.

Assuming that the current has a linear response to the applied voltage, the waveforms of the voltage and current can be described as vectors which are sinusoidal and given by equation 1 and 2 which can be simplified to equation 3 to explain impedance of AC circuit with multiple components[1];

$$V(t,\omega) = V_0\big(\cos(\omega t) - t\sin(\omega t)\big) = V_0 e^{i\omega t} \qquad \text{equation 1}$$

$$I(t,\omega) = I_0\big(\cos(\omega t + \theta) - t\sin(\omega t + \theta)\big) = I_0 e^{i\omega t + \theta} \qquad \text{equation 2}$$

$$Z(\omega) = \frac{V(\omega)}{I(\omega)} = |Z|e^{j\varphi} = Z' + jZ'' \qquad \text{equation 3}$$

$Z^{'} = |Z|\cos\theta$, $Z^{''} = |Z|\sin\theta$ When $\theta = 0$, $Z' = R_e$ and when $\theta = \pi/2$, $Z^{''} = 1/\omega C$. R_e is the frequency independent resistance and C is the capacitance.

Z (ω) can be plotted with polar coordinates as shown in Fig. 2.6. When measuring impedance the |Z| and phase θ values for real and imaginary components Z' and Z'' can be calculated respectively. R_1 represents the bulk resistance of the sample and R_3 is the grain boundary resistance of the sample (see fig 2.6).

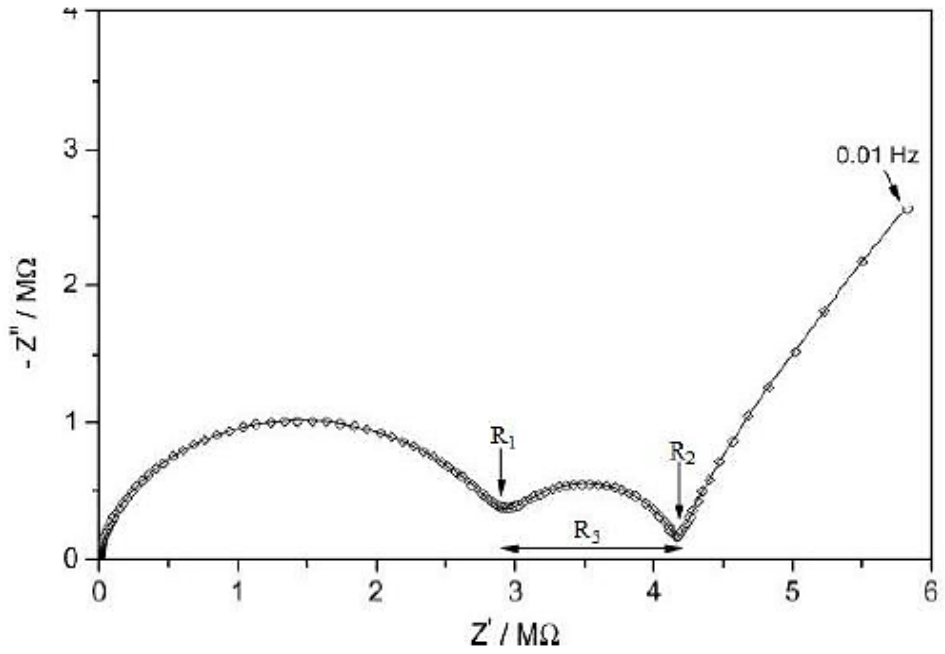

Figure 2.6: Ionic conductor impedance spectrum[1].

Using a combination of basic components such as resistors (R), capacitors (C), constant phase elements (CPE) and Warburg (W) diffusion elements, an impedance of a material can be modeled with an electrical equivalent circuit (EQC). These circuit elements can be connected in parallel or series. Table 2.1 shows the individual electrical components used in the modeling of EQCs and fig 2.7 shows examples of EQCs and the resultant spectra they produce.

Table 2.1: Common circuit elements used in EQC models[5].

Element	*Description*	*Impedance*
C	Capacitor	$1/j\omega C$
L	Inductance	$j\omega L$
R	Resistance	R
Q	Constant phase element (CPE)	
	α = 1: CPE = capacitor	
	α = 0.5: CPE = Warburg	$1/Y_0(j\omega)^{\alpha}$
	α = 0: CPE = resistance	
	α = -1: CPE = capacitor	
W	Warburg (Semi-infinite diffusion)	$1/Y_0\sqrt{j\omega}$
G	Gerischer	$R_G/\sqrt{1+2\pi JG_f}$
M	Restricted linear diffusion	$R_{dt}(\coth(\sqrt{\tau_d i2\pi f}))/\sqrt{\tau_d i2\pi f}$

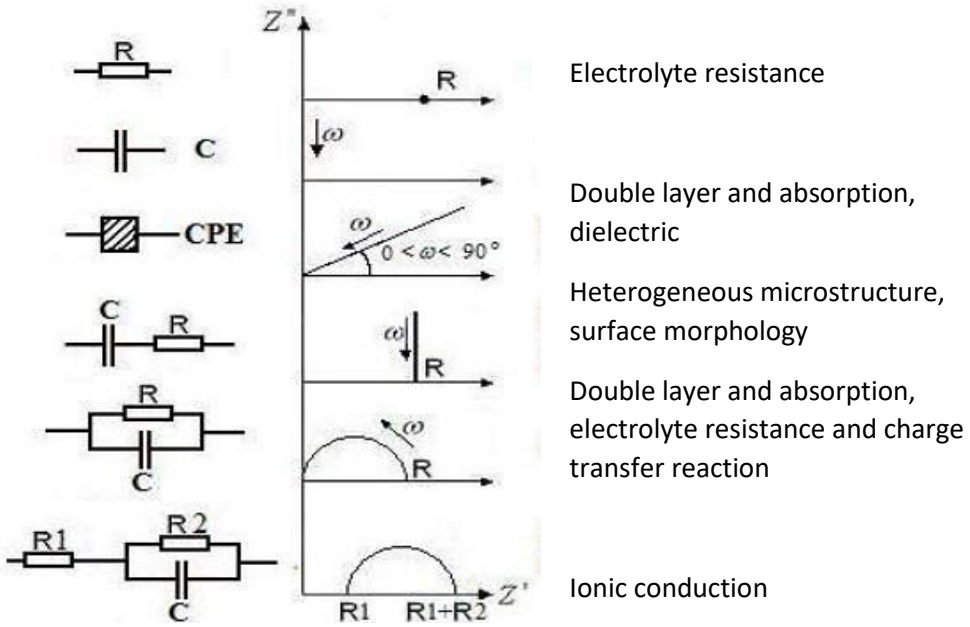

Figure 2.7: Electrical components and their respective impedance spectra[1].

2.4 Simultaneous thermal analysis (STA).

The simultaneous thermal analysis (STA) measures both the heat flow and weight change in materials as a function of temperature in a controlled environment. In a single experiment, the STA can measure the Thermogravimetric (TG) and Differential scanning calorimetry (DSC) simultaneously. In this study, the STA was used to monitor the heat flow and weight changes in samples during the heating and cooling cycles. These results were displayed in a plot of heat flow against temperature in which endothermic and exothermic peaks were observed.

The endo/exothermic peaks are commonly associated with growing new crystal grain, nucleation of reacting species, phase transition or a change in state from solid → liquid → gas of samples. Fig 2.8 shows an example of $MgAl_2O_4$ STA diagram. The observed weight loss of the sample during the heating cycle was associated with the evaporation of the absorbed water and dehydration reaction of $Al(OH)_3$ and $Mg(OH)_2$ to form the final product $MgAl_2O_4$. The weight loss was accompanied by endothermic peaks at 245 °C and 356 °C respectively (see diagram below).

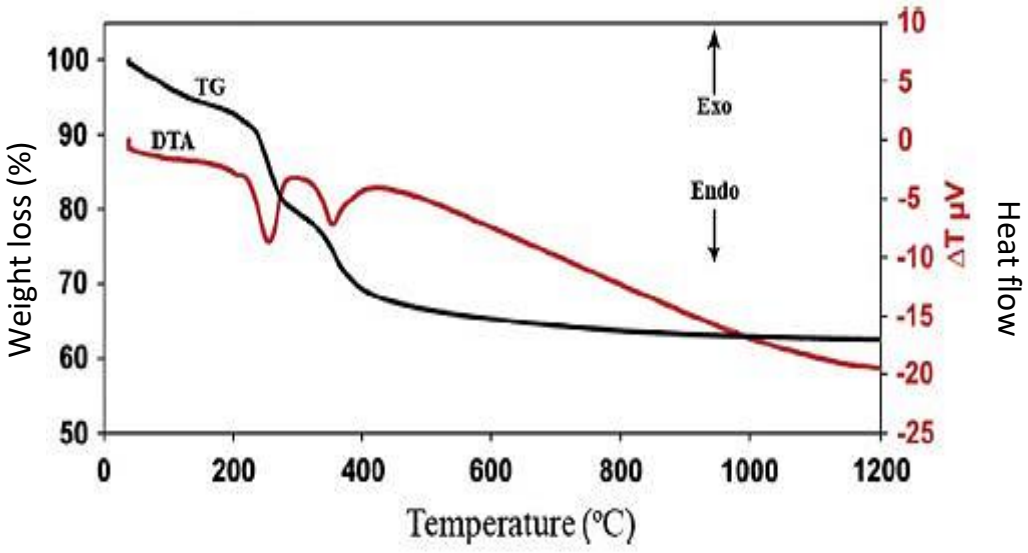

Figure 2.8: The simultaneous thermal analysis of $MgAl_2O_4$[6].

2.5 Raman spectroscopy (RS).

The Raman spectroscopy (RS) assist in determining metal oxides bulk phases with characteristic Raman bands providing basic information on the structure and bond length of atoms in materials[7]. RS is different from Infrared spectroscopy (IR), IR is based on the absorption of photons meanwhile RS measures light scattering [8].

During an RS analysis, a sample is irradiated with a light source usually a laser light and the sample emit oscillating dipole moment in phase with the frequency of the incident light, a process known as Rayleigh scattering[8]. The scattered rays have two different frequencies modulated by the frequency of the exciting vibration of the molecules and the phase shift. In simple terms, the scattered light have higher or lower frequency as the incident light[8].

According to classical models where α_o is the polarizability of a molecule at the equilibrium position and q_o is the vibration amplitude[9], if the rate of change of α_0 to q_0 is equal to zero $((\partial_\alpha/\partial_q)_0 = 0)$, the vibration is not Raman-active. Raman-active peaks/bands are observed if the rate of change of α_0 to q_0 is not equal to zero $((\partial_\alpha/\partial_q)_0 \neq 0)$[9]. Fig 2.9 shows the Raman spectrum of CCl_4 showing the Stokes and anti-Stoke lines under ambient conditions. Since Stokes lines have higher intensity compared to anti-Stokes lines only the Stokes side of the spectrum is commonly presented. Stokes lines are measured scattered radiation from the sample showing the different geometries of the material.

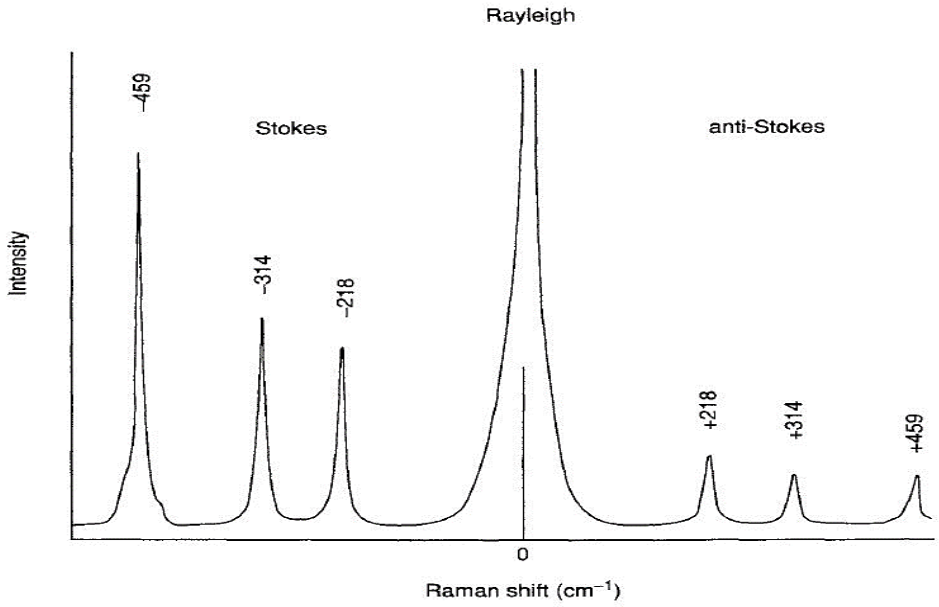

Figure 2.9: The Raman spectrum of CCl_4 (excitation = 488.0 nm)[9].

2.6 X-ray pair distribution function (PDF)

Pair distribution function (PDF) is a Fourier transformation of the total scattering of the Bragg and diffuse diffractions[10]. PDF can measure short-ra**nge structural disorders in amorphous materials, crystalline and nanomaterials. It gives the probability** of finding an atom at a distance "r (Å)" in real space from the selected atom[10]. The total scattering factor S (Q) is determined from the scattering intensity equation 1.

$$S(Q) = \frac{I_{coh}(Q) - \sum c_i |b_i|^2}{|\sum c_i b_i|^2} + 1 \qquad \text{equation 1}$$

$$Q = 4\pi \mathrm{Sin}Q/\lambda$$

I_{coh} (Q) represent the coherent scattering intensity which is corrected for background scattering and self-absorption. $\sum c_i |b_i|^2$ represent the scattering length for a neutron or the atomic form factor for X-ray[10]

To transform the above equation 1 to real space to allow quantitative analysis of PDF data the momentum transfer (Q -space or reciprocal space) must be Fourier transformed into real space to give equation 2. PDF data is commonly collected for longer periods in reciprocal space with very small-time steps.

$$G(r) = \frac{2}{\pi}\int_{Q_{min}}^{Q_{max}} Q[S(Q) - 1]\,\mathrm{Sin}(Q_r)dQ \qquad \text{equation 2}$$

To achieve good data collection and resolution, the momentum transfer must be maximum (Qmax) but high Q values results in peak width broadening which causes damping in real space11. Fig 2.10 shows the Sine-Fourier transformation of the total scattering diffraction with noticeable damping at higher Q values and poor resolution.

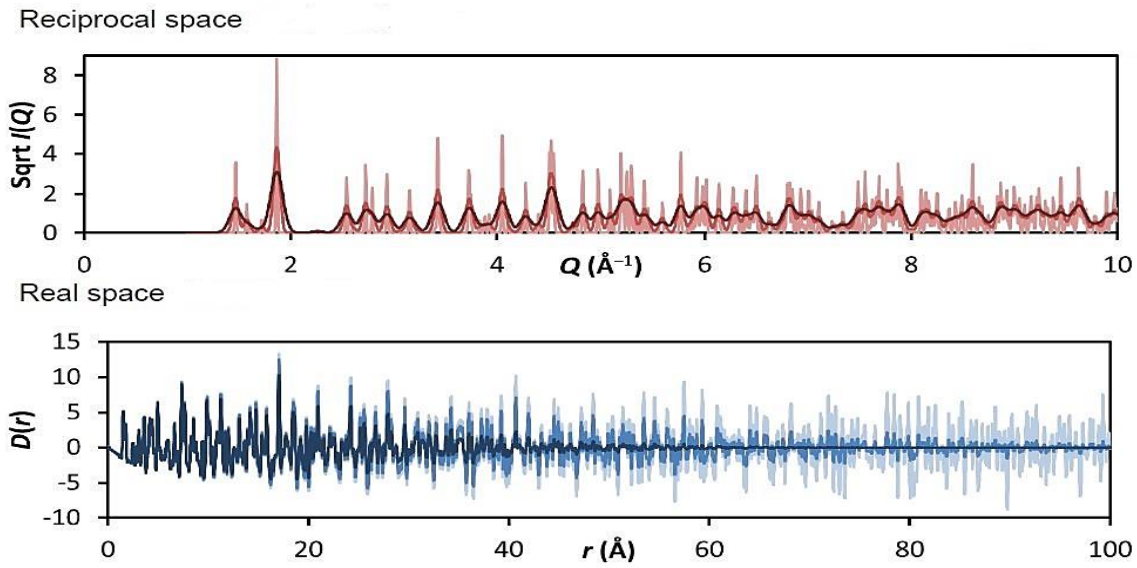

Figure 2.10: Fourier transformation of the total scattering diffraction [12].

PDF analysis involves data modelling and refinement to determine the local disorders in crystal structures[11]. In addition, real space PDF plot can revel other structural parameters as shown in fig 2.11. Two most important methods of PDF modelling are Small box modelling (SBM) and Big box modelling (BBM). The SBM method requires a starting structure preferably with periodicity. This method is very quick and has low entry barriers. The BBM method can simultaneously fit real and reciprocal space data and account for diverse types of disorders in the structure. However, the process is time consuming and computational intensive[13].

Often there are discrepancies between the observed and calculated data due to incorrect model or poor resolution caused by instrument limitations[10]. During data modelling, a residual factor (R_{wp}) was used to check the accuracy of the PDF refinement.

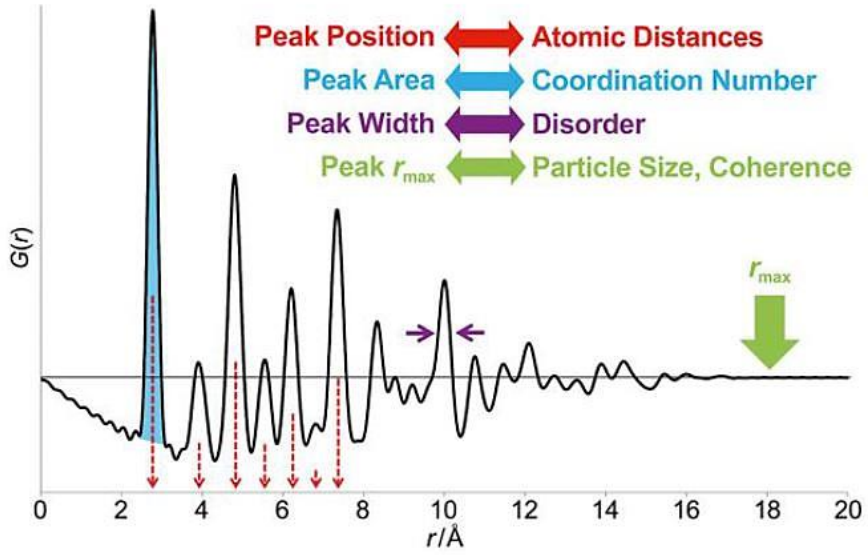

Figure 2.11: PDF analysis plot in real space[12]

Chapter 3

Determination of samples crystal phases and thermal analysis.

3.1 Introduction and outline.

A good solid oxide electrolyte or ionic conductor has good thermal stability and high oxygen vacancies at low temperatures (400° C – 600° C). In this study, $Bi_2VO_{5.5}$ was synthesized using the citrate method to produce cit-BiVO sample which was doped with Ce^{4+} at different concentrations to prepare cit-$BiCe_xVO$ samples. Chapter 3 was dedicated to determining the crystallographic phases and thermal analysis of cit-BiVO and cit-$BiCe_xVO$ materials.

According to literature, the ɣ-phase of $Bi_2Cu_{0.10}V_{0.90}O_{5.5}$ is the most conductive BiMeVOx material to date and this project was interested in doping $Bi_2Cu_{0.10}V_{0.90}O_{5.5}$ with 10% mol Ce^{4+} using the solid-state method to prepare sol-$BiCu_{0.10}Ce_{0.10}VO$ sample and study the impact of Ce^{4+} doping.

3.2 Experimental procedures:

3.2.1 Synthesis of cit-BiVO and cit-$BiCe_xVO$ ($0.04 \leq x \leq 0.28$) samples.

Sigma-Aldrich $Ce(NO_3)_3{\cdot}6H_2O$, $Bi(NO_3)_3{\cdot}5H_2O$ and $VOCl_3$ chemicals were separately dissolved in 100 ml beakers in acetic acid under mild heating and gently stirring on a magnetic stirrer for ≈10 min. This process was done to dissolve the chemicals into V^{5+}, Ce^{4+} and Bi^{3+} metal ions separately. Then a mixture of metal ions was created by mixing all three dissolved solutions into a single 500 ml beaker. Citric acid was added to the mixture (note that the Citric acid was first dissolved in a 100 ml beaker of acetic acid under mild heating and gently stirring on a magnetic stirrer).

The mixture of metal ions and Citric acid formed a green paste-like substance due to the complexation of the metal ions and Citric acid. Then a light blue paste was produced as the final product. The colour change observed during the synthesis was due to the oxidation of vanadium from $V^{3+} \rightarrow V^{4+}$. All samples were calcined at 480°C for 16 hours using ceramic crucibles in the furnace to decompose the organic matter and form metal oxides. During the calcination the oxidation of vanadium changed from $V^{4+} \rightarrow V^{5+}$ (noted by the sample colour change to a bright yellow). Later all samples were annelid at 780°C for 24 hours in the furnace.

Table 3.1: Weighed masses for the synthesis of cit-BiVO and cit-$BiCe_xVO$ using the citrate method.

No.	*Targeted composition*	*sample*	*$Bi(NO_3)_3{\cdot}5H_2O$ /(g)*	*$Ce(NO_3)_3{\cdot}6H_2O$ /(g)*	*$VOCl_3$ /(µl)*	*Citric acid /(g)*
1	$Bi_2VO_{5.5}$	cit-BiVO	1.7420	0.0000	169	10.1220
2	$Bi_2Ce_{0.04}V_{0.96}O_{5.48}$	cit-$BiCe_{0.04}VO$	3.4639	0.0620	323	10.3180
3	$Bi_2Ce_{0.07}V_{0.93}O_{5.465}$	cit-$BiCe_{0.07}VO$	3.4489	0.1081	311	10.2010
4	$Bi_2Ce_{0.13}V_{0.87}O_{5.435}$	cit-$BiCe_{0.13}VO$	3.4193	0.1990	289	10.0011
5	$Bi_2Ce_{0.18}V_{0.82}O_{5.41}$	cit-$BiCe_{0.18}VO$	3.3950	0.2735	270	10.3320
6	$Bi_2Ce_{0.23}V_{0.77}O_{5.385}$	cit-$BiCe_{0.23}VO$	3.3711	0.3470	252	10.2110
7	$Bi_2Ce_{0.28}V_{0.72}O_{5.36}$	cit-$BiCe_{0.28}VO$	3.3475	0.4195	234	10.1045

SYNTHESIS PROCEDURE

Chapter 3

Step 1: Dissolution of metal hydrates and chloride in acetic acid.

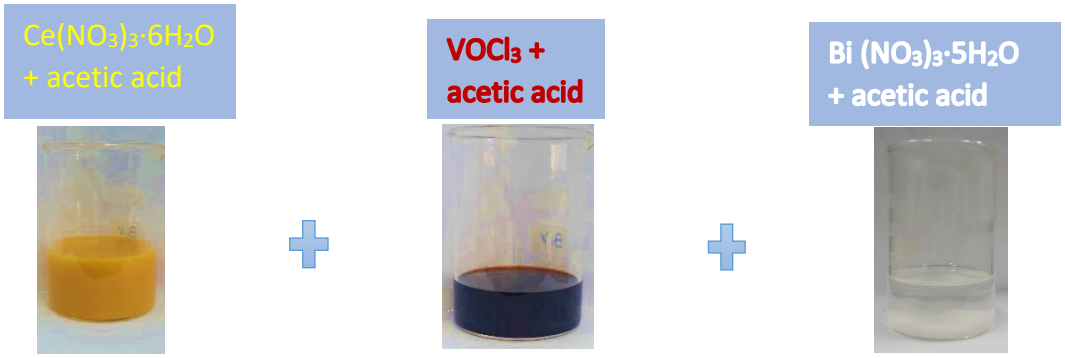

STEP 2: Mixing of all metals into one beaker.

Step 3: Gentle heating and stirring for ≈20 minutes

Step 4: Slow addition of dissolved citric acid-monohydrate.

Citric acid

Step 4: Evaporation of acetic acid.

3.2.2 Synthesis of sol-$BiCu_{0.10}VO$ and sol-$BiCu_{0.10}Ce_{0.10}VO$ samples.

Sigma-Aldrich V_2O_5, CeO_2, CuO and Bi_2O_3 chemicals were separately weighted according to table 3.2 masses and ground with a pestle, mortar and acetone individually for ≈10 minutes to produce fine powdered chemicals. Later all chemical powders where simultaneously grinded for ≈45 minutes and annelid at 700 °C for 12 hours using ceramic crucibles in the furnace three times with intermediate 45 minutes grinding after each annealing process.

Table 3.2.: Weighed masses for the synthesis of sol-$BiCu_{0.10}VO$ and sol-$BiCu_{0.10}Ce_{0.10}VO$ using the solid-state method.

No.	*Targeted composition*	*Sample*	*Bi_2O_3 /(g)*	*CuO /(g)*	*CeO_2 /(g)*	*V_2O_5 /(g)*
1	$Bi_2Cu_{0.10}V_{0.90}O_{5.35}$	sol-$BiCu_{0.10}VO$	1.8276	0.0156	0.0	0.3210
2	$Bi_2Cu_{0.10}Ce_{0.10}O_{5.35}$	sol-$BiCu_{0.10}Ce_{0.10}VO$	1.6356	0.0140	0.0302	0.2873

3.2.3 PXRD measurement and Rietveld refinement.

The Bruker D2 phaser X-ray diffractometer fitted with a Co K_α = 1.7903 Å X-ray tube operating at 30 kV and 10 mA was used for PXRD measurements. Data was taken in 2θ degree values from 5 ° – 90 ° with steps of 0.026 ° and the total scanning time was set at 29 minutes. A 25 mm diameter silicon sample holder was used where each sample was press down the shallow well of the sample holder with a flat glass and any extra sample outside the well was removed with propanol and paper towel. The Bruker D8_Advance X-ray diffractometer fitted with a Cu kα = 1.5406 Å X-ray tube operating at 40 kV and 40 mA was employed for variable temperature XRD (VT-XRD) measurements. Samples were heated from 30° C - 780° C in steps of 30° C intervals under air atmosphere and cooled back to room temperature at 30° C intervals.

The Diffra.EVA v4.2.1 program was used to identify the samples crystal phases and the samples Crystallographic Information Files (cif) were downloaded from the Inorganic Crystal Structure Database (ICSD). Below are the two cif files which were used in this work.

Cif for β*-phase*	*Cif for* α*-phase*
Chemical name systematic: Tetrabismuth divanadate	Chemical name systematic : Bismuth vanadate
Chemical formula structural: $Bi_2VO_{5.5}$	Chemical formula structural: $BiVO_4$
Space group = Amam	Space group = I112/b
Orthorhombic	Monoclinic
Database code ICSD: 98434	Database code ICSD: 33243

The Rietveld refinement was performed using Topas v5.0 program accordingly:

- A PXRD measurement from the Lab D2 XRD instrument was uploaded to the program.
- The background signal was fitted with a Chebyshev function with six coefficients for smoothing of the background noise.
- The instrument file was loaded to the program containing the instrument settings used to measure the PXRD.
- The two cif data files listed above were uploaded to Topas.
- The peak profile Thompson-Cox-Hastings pseudo-Voigt (pV-TCHZ) profile function was selected to model peaks.
- The monoclinic phase cif data file (α-phase) parameters were refined first since it was determined to be the minor phase then followed by the refinement of the major orthorhombic phase cif data file (β-phase).
- The unit scale and lattice parameters (*a,b,c*) were simultaneously refined together since any changes to the lattice parameter altered the unit scale.
- Either the zero point or sample height was refined since these parameters are highly correlated.
- The thermal parameter (Beq) was constrained between a minimum and a maximum value. Heavy atoms $Bi^{3+}$and V^{5+} Beq values were set between 0.05 - 1 since these atoms displacement in the crystal structure were limited compared to O^{2-} atoms Beq value which was set between 0.05 - 2.5 to account for the presence of oxygen vacancy and displacement of O^{2-} ions in the crystal structure.
- The atomic positions of O^{2-} ions were refined if necessary except for O^{2-} ions with special atomic position e.g. (x,y,z,) = (0,0,0,).
- This process was repeated multiple times until a good fit was achieved indicated by a low R_{wp} and GOF values.

3.2.4 Raman spectroscopy and STA measurement.

The Raman spectra were generated using Ar ion laser as the incident light source with the power set at 0.04 mW and 0.4 mW. The scattered radiation from the samples were measured with a Horiba LabRAM HR spectrometer coupled to an intensified photodiode array and an optical multichannel analyser. Approximately 100–200 mg of each sample was pressed between two thin glasses to about 1 mm thickness then mounted onto a sample holder and heated from 25 °C – 800 °C under oxygen atmosphere.

The Simultaneous Thermal Analyzer (STA) 6000 from PerkinElmer was used for thermal analysis. First an empty ceramic crucible was measured as a blank using the following method: Start the run by switching gases from nitrogen to air at 20.0 ml/min then heat the crucible from 100.00°C to 820.00°C at 20.00°C/min. Then Cool the crucible from 820.00°C to 100.00°C at 20.00°C/min and hold for 1.0 min at 100.00°C to switch the gas back from air to nitrogen at 20.0 ml/min. The blank results were then subtracted from the sample STA measurement during the analysis using the same method. ≈15.38 mg of each sample was weighted.

3.3 Results and discussion.

3.3.1 cit-BiVO results.

The Rietveld refinement plot of cit-BiVO after 24 hours of annealing at 780 °C is shown in Fig 3.1. cit-BiVO was determined to exhibit two phases at room temperature; the predominate phase was orthorhombic (β-phase) and the minor phase was monoclinic (α-phase). The α-phase was the undesired phase in this study due to the phase low ionic conductivity[2]. However, the α-phase has found extensive use in photocatalysis for organic pollutant degradation under visible light due to the phase narrow band gab (2.4ev) [3].It is important to highlight that cit-BiVO had two different α-phases, the first α-phase was observed due to the decomposition of the β-phase with a chemical composition of $BiVO_4$. This α-phase overshadowed the other cit-BiVO α-phase with the chemical composition of $Bi_2VO_{5.5}$. The Lab PXRD measurements were only capable of identifying the α-phase with the chemical

composition of $BiVO_4$ meanwhile the synchrotron XRD was capable of distinguishing the two phases see later. As such the α-phase of cit-BiVO referred to in this chapter has the chemical composition of $BiVO_4$

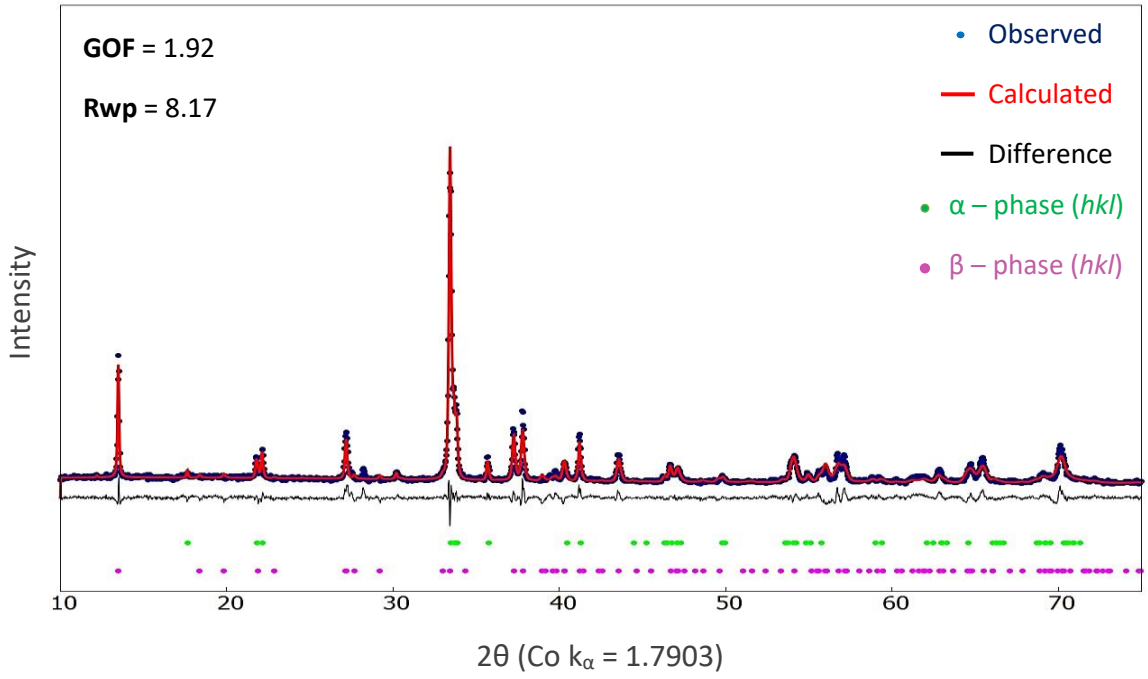

Figure 3.1: Room temperature Rietveld refinement plot of cit-BiVO. β-phase composition = 87.5 % and α-phase composition ($BiVO_4$)= 12.5 %

The STA measurement of cit-BiVO is shown in fig 3.2.An endothermic peak was observed at ≈576 °C during the heating cycle which was due to the α → β phase transition and a second endothermic peak was noted at ≈ 435 °C due to the phase transition from β → γ phase[4]. The cooling cycle had reversible phase transitions as depicted by the two exothermic peaks from γ → β → α phases.

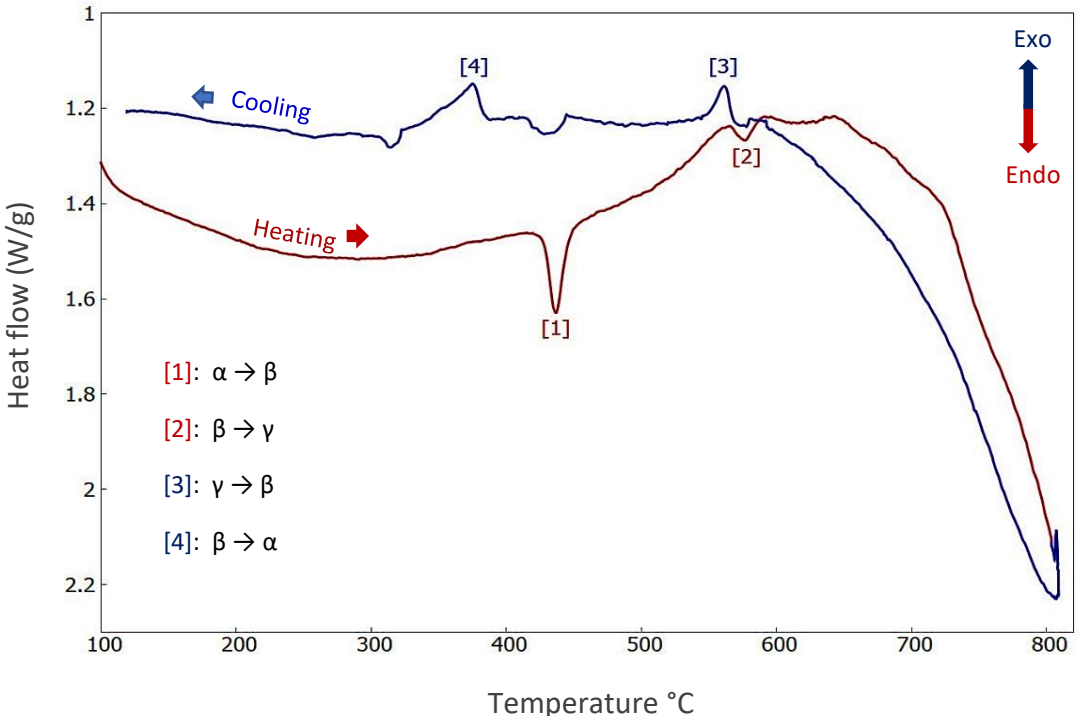

Figure 3.2: The STA diagram of cit-BiVO under oxygen atmosphere.

The Raman peaks of cit-BiVO were difficult to separate, the band at 826 cm^{-1} was observed as a result of a superposition between two peaks with similar site symmetry/phase[6]. Distinctive bands for the α-phase were assigned at 366 cm^{-1},320 cm^{-1},210 cm^{-1}, and 127 cm^{-1}. The high intense asymmetry band at 826 cm^{-1} was assigned to the β-phase with a weak band normally at 700 cm^{-1} shifted to 710 cm^{-1} also assigned to the β-phase. The band at 925 cm^{-1} indicated a higher order of VO_4 symmetry indicating an octahedra structure which can be associated to the γ-phase of cit-BiVO.

The V-O stretch mode A_g symmetric for the α-phase was observed at 826 cm^{-1} while the band at 716 cm^{-1} was assigned to V-O stretch mode B_g antisymmetric[6]. The symmetric and antisymmetric bending modes were noted at 366 cm^{-1} and 320 cm^{-1} assigned to A_g and B_g respectively. 210 cm^{-1} and 127 cm^{-1} were external modes due to translation and rotation symmetry.

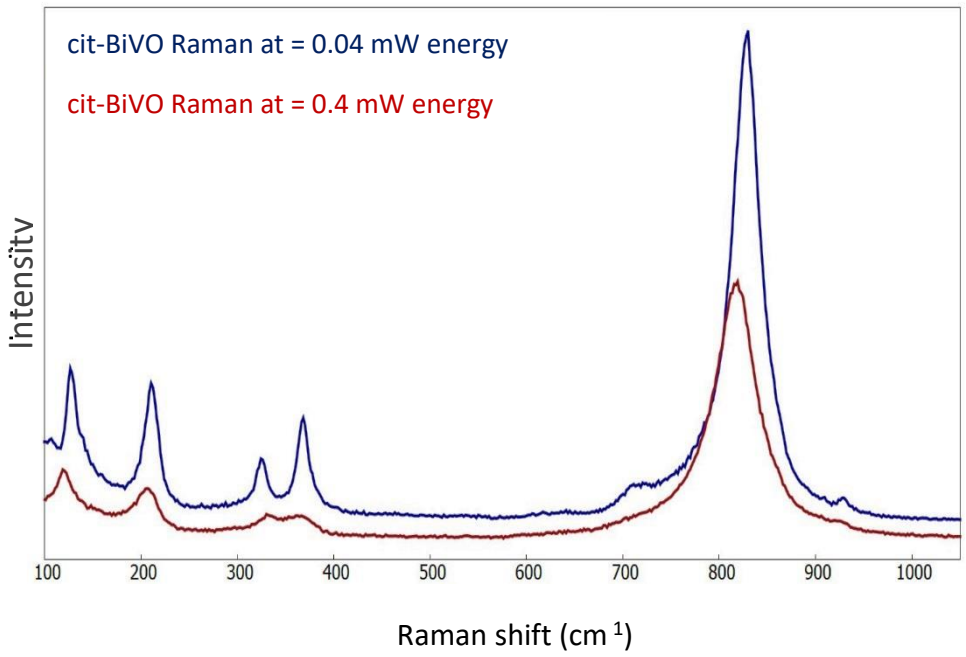

Figure 3.3: The Raman diagram of cit-BiVO at room temperature.

The variable-temperature (VT) - XRD patterns indicated a phase transition of cit-BiVO at 600 °C consistent with the β → γ phase transition. The γ-phase was determined between 600 °C - 800 °C with the gradual appearance of a singlet peak at 2θ ≈ 35 ° and the disappearance of a peak at 2θ ≈ 23 °C. It was difficult to separate the β-phase and γ-phase to some degree because these two phases have similar PXRD scattering patterns, but the peaks mentioned above are purely associated with the γ-phase.

Upon cooling the sample back to room temperature, two phase transformations were observed. The first transition was γ → β phase at 600 °C indicated by the peak reappearance at 2θ ≈ 23 ° and the disappearance of a peak at 2θ ≈ 35 °. The second phase transition was at 400 °C for β → α phase noted by the slight peak shift at 2θ from 23 ° to 22 °.

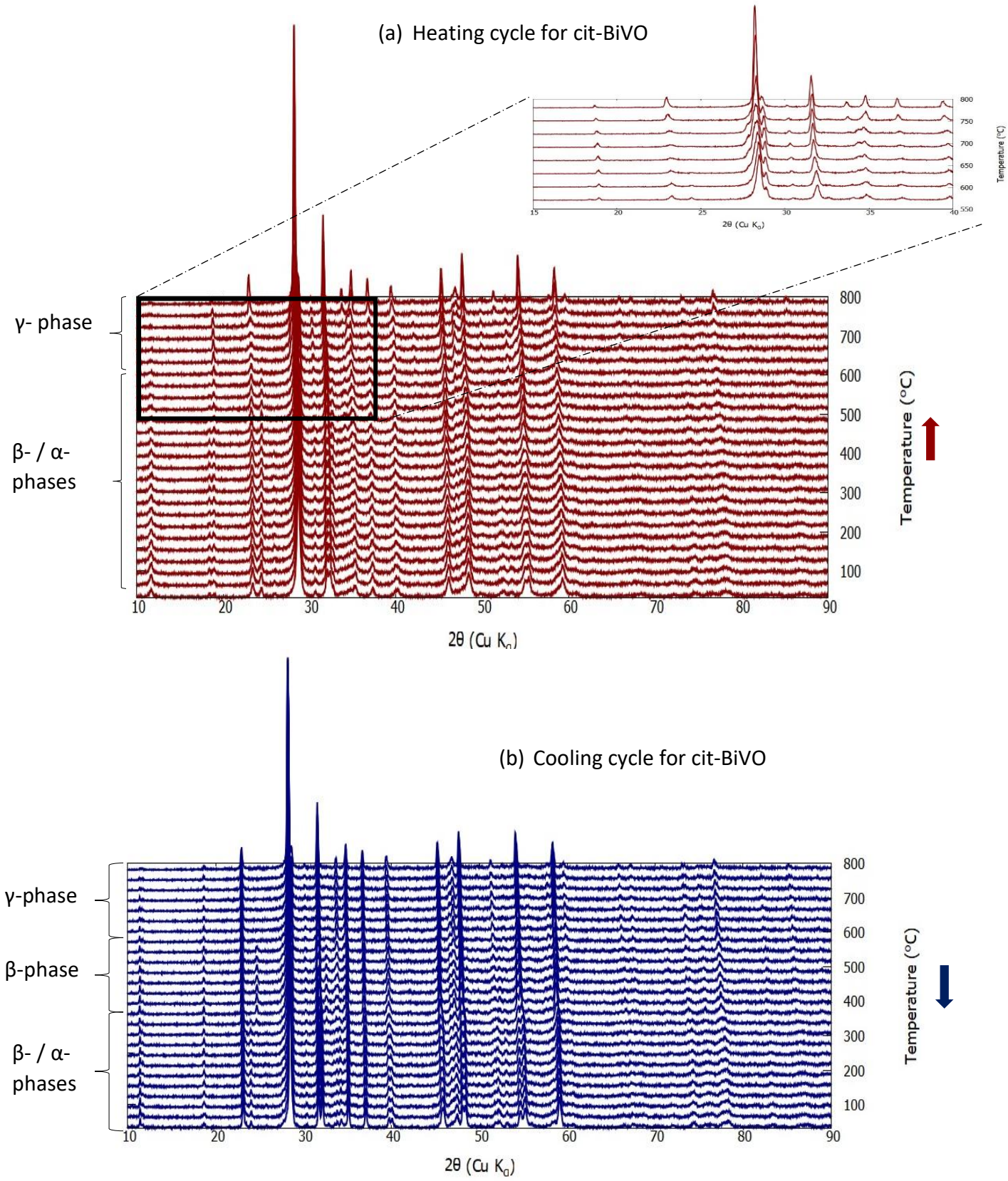

Figure 3.4: VT-XRD of cit-BiVO under air atmosphere.

The VT-XRD data together with the JEdit v5.6.0 and Topas v6.0 academia were used to determine the *a-,b-,c-* lattice parameters changes with increasing/decreasing temperatures accordingly.

- Uploaded the VT-XRD data to JEdit v5.6.0.
- Selected the XInsert node TOPAS_Durham folder.
- Selected simple Lab Rietveld refinement.
- The background signal was defined for a Chebyshev polynomial and only the zero point was refined.
- The durham_d8 option was selected under instrument settings.
- The α- and β-phases cif data files were uploaded to JEdit
- The Beq values were fixed at Bi^{3+} = 1, V^{5+} = 1 and O^{2-} = 2.5
- The atomic occupancies were also fixed at Bi^{3+} = 1, V^{5+} = 0.5 and O^{2-} = 2.75.
- The atomic positions of O^{2-} ions were refined if necessary except for atoms with special atomic position (x,y,z,) = (0,0,0,).
- This process was repeated many times until a good fit was achieved indicated by a low R_{wp} and GOF values.

The *a*- and *c*-lattice parameters changed abruptly with increasing/decreasing temperatures as a result of the reversible phase transitions from α → β → ϒ (see fig 3.5). The *b*-lattice parameter had a gradual slope with increasing temperatures indicating the stabilisation of the ϒ-phase.

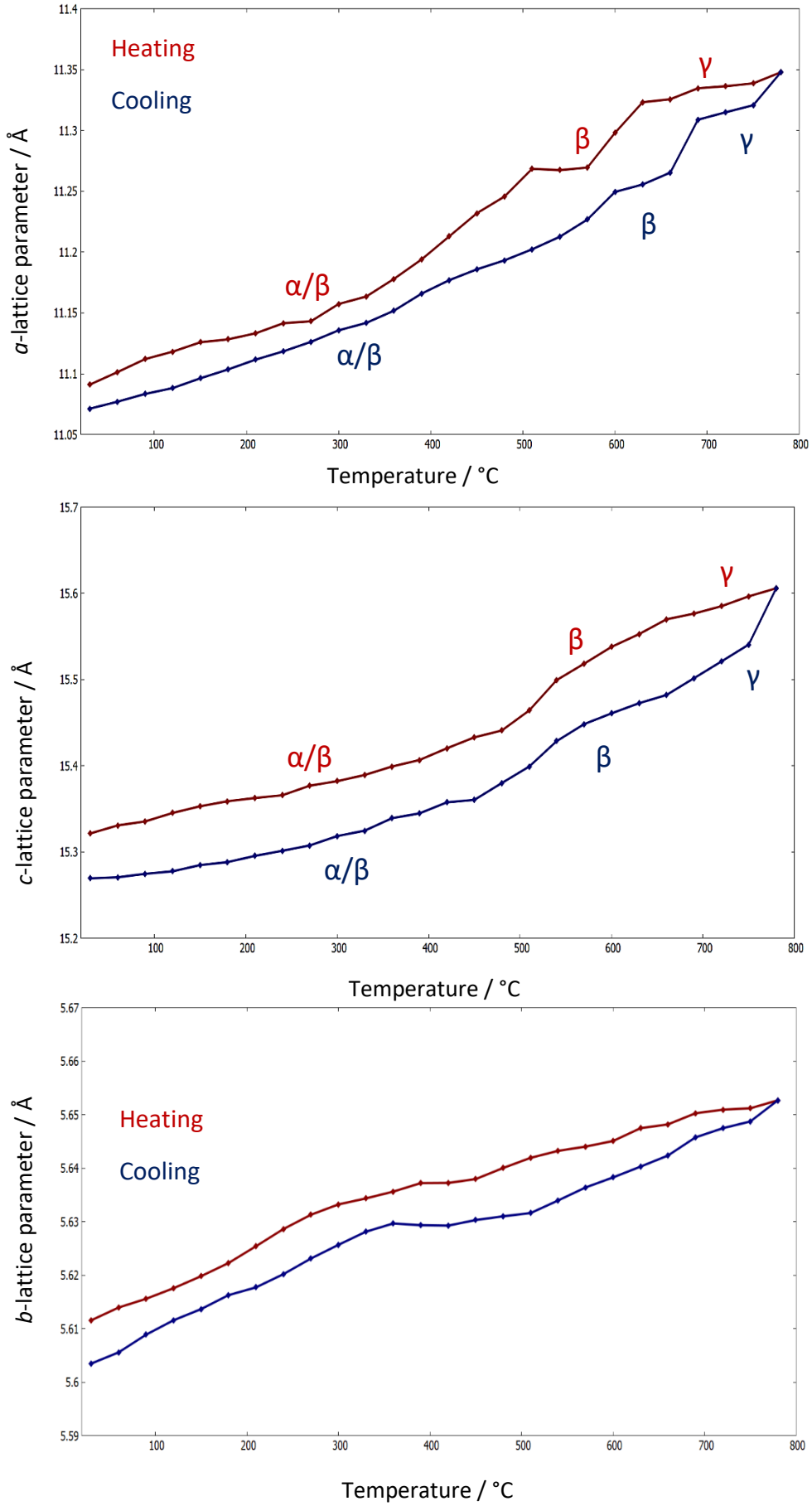

Figure 3.5: Refined lattice parameters of cit-BiVO as a function of temperature.

3.3.2 cit-$BiCe_xVO$ ($0.04 < x < 0.28$) results.

A range of different Ce^{4+} ion concentrations were selected for doping cit-BiVO using the citrate method to make cit-$BiCe_xVO$ ($0.04 \leq x \leq 0.28$) samples. It was determined that cit-$BiCe_XVO$ samples were predominantly β-phase at room temperature with a minor α-phase present. An additional step was introduced in the Rietveld refinement of cit-$BiCe_xVO$ in Topas v5.0. where a Ce element was added to the cif file of the β-phase for better fit/refinement and the Beq values and atomic positions of Ce^{4+} ions were matched with that of V^{5+} ions after determining that Ce^{4+} preferred ion substitution at V^{5+} lattice sites using the Raman data. The Rietveld refinement plots of cit-$BiCe_xVO$ ($0.04 \leq x \leq 0.28$) are presented in fig 3.6.

It was observed that by increasing the amount of Ce^{4+} concentration the doublet peak at $2\theta \approx 23^\circ$ associated with the α- phase ($BiVO_4$) gradually disappeared and for samples with higher levels of Ce^{4+} concentration ($x > 0.18$), the α-phase quantity was low. Additionally, as Ce^{4+} concentration increased the γ-phase was gradually stabilized. The room temperature phase composition plot in fig 3.7 indicated an inverse relationship between the β-phase and α-phase where one phase increases the other phase decrease as Ce^{4+} concentration increased.

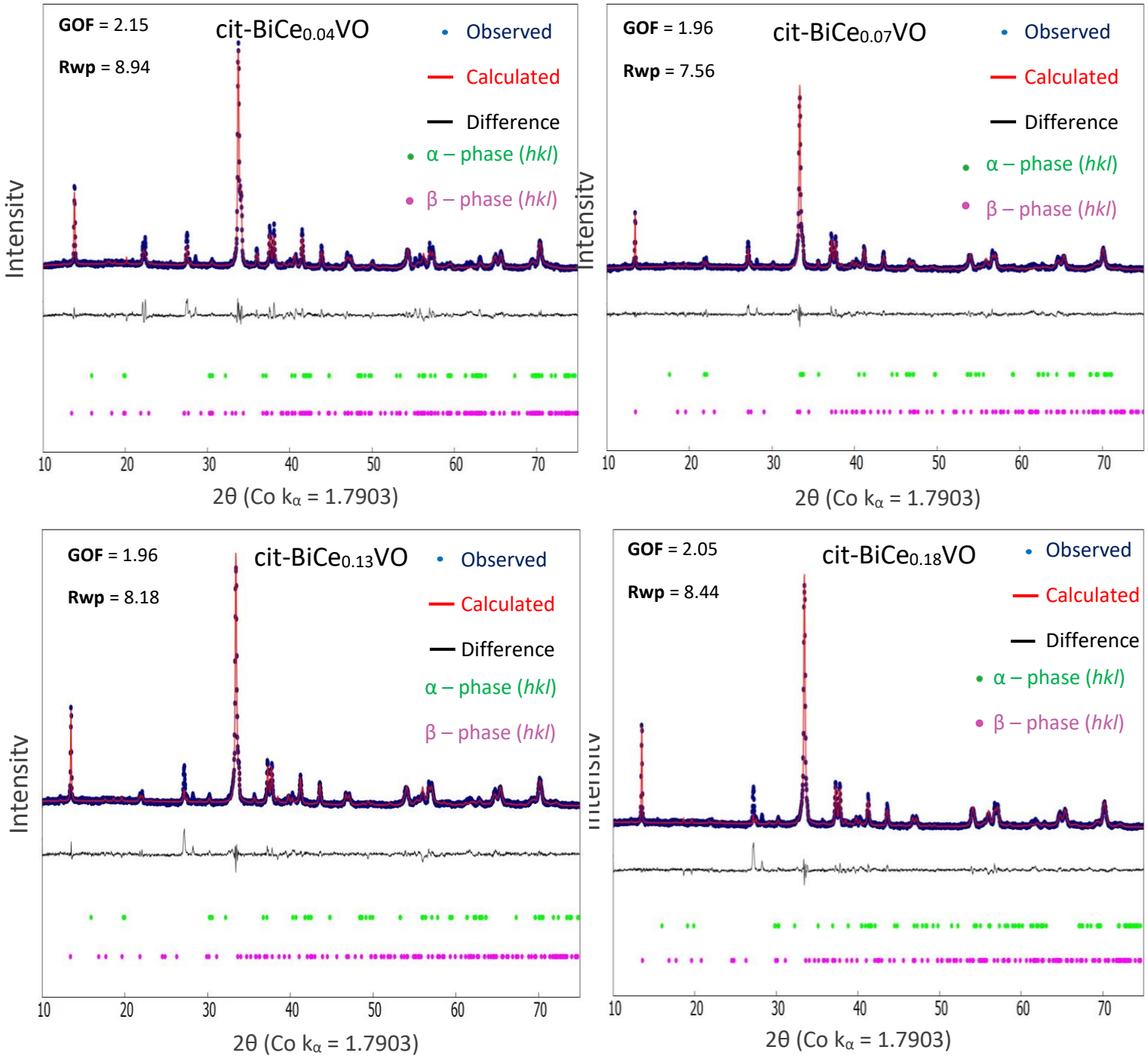
GOF = 2.15
Rwp = 8.94
cit-BiCe0.04VO
Observed
Calculated
Difference
α – phase (hkl)
β – phase (hkl)
Intensity
10 20 30 40 50 60 70
2θ (Co kα = 1.7903)
GOF = 1.96
Rwp = 7.56
cit-BiCe0.07VO
Observed
Calculated
Difference
α – phase (hkl)
β – phase (hkl)
Intensity
10 20 30 40 50 60 70
2θ (Co kα = 1.7903)
GOF = 1.96
Rwp = 8.18
cit-BiCe0.13VO
Observed
Calculated
Difference
α – phase (hkl)
β – phase (hkl)
Intensity
10 20 30 40 50 60 70
2θ (Co kα = 1.7903)
GOF = 2.05
Rwp = 8.44
cit-BiCe0.18VO
Observed
Calculated
Difference
α – phase (hkl)
β – phase (hkl)
Intensity
10 20 30 40 50 60 70
2θ (Co kα = 1.7903)

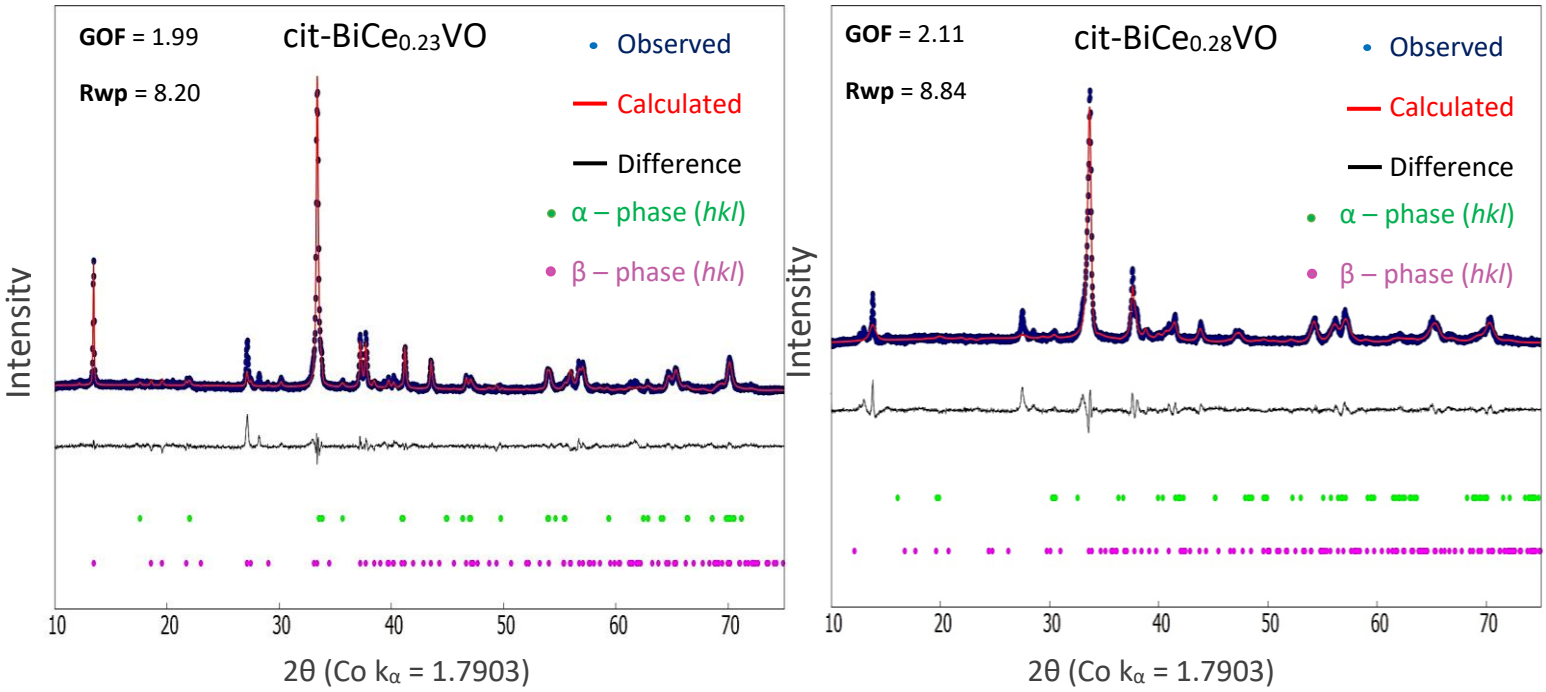

Figure 3.6: Room temperature Rietveld refinement plots of cit-BiCe$_x$VO ($0.04 \leq x \leq 0.28$).

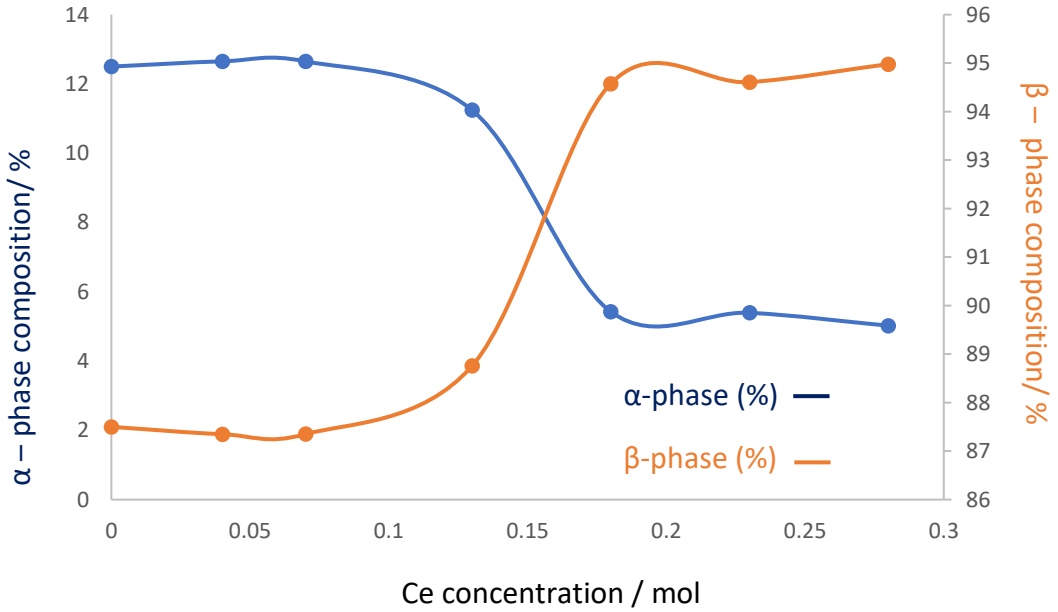

Figure 3.7: Room temperature phase composition plot of cit-BiCe$_x$VO ($0.04 \leq x \leq 0.28$) samples.

The STA diagram in fig 3.8 complemented the PXRD data, two endothermic peaks were observed consistent with the α → β → γ phase transitions which were reversible upon cooling[4]. The Pyris v13.3.1 program was used to calculate the peak area underneath the endothermic peaks which was equivalent to the change in enthalpy (ΔH). It was noticed that the ΔH for α → β transition decreased with increasing Ce^{4+} concentrations meaning that samples required less heat/energy to transition from α → β and even less heat was required for the β → γ phase transition.

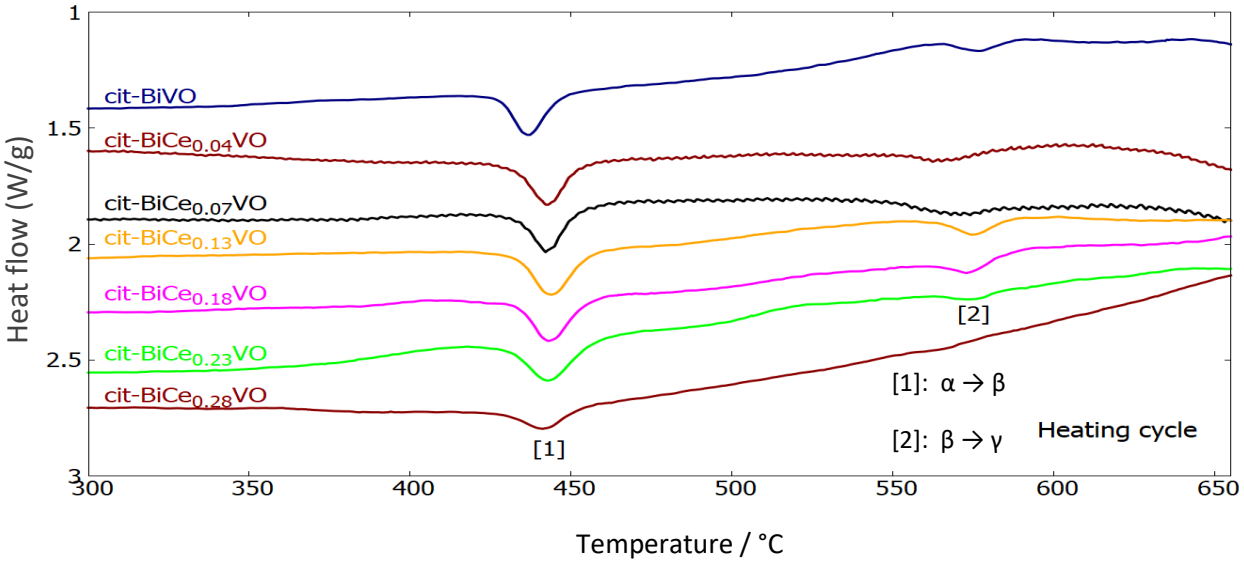

Figure 3.8: The STA diagram of cit-BiVO and cit-$BiCe_xVO$ under oxygen atmosphere.

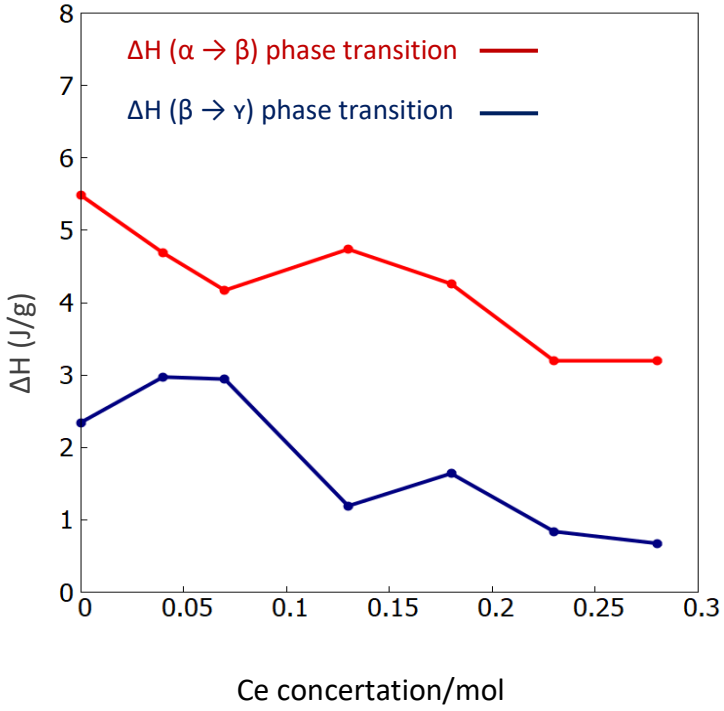

Figure 3.9: Change in enthalpy as a function of Ce^{4+} concentration plot.

The VT-XRD of cit-$BiCe_{0.13}VO$ was analysed using the JEdit v5.6.0 and Topas v6.0 academia program according to the same procedure used for the analysis of cit-BiVO with the inclusion of Ce on the β-phase cif file as describe earlier. Three different polymorphs of cit-$BiCe_{0.13}VO$ were determined, at room temperature cit-$BiCe_{0.13}VO$ had a mixture of two phases; α-phase and β-phase as shown in fig 3.10 (a) and the α-phase disappeared above 300 °C. Upon further heating the material above 540 °C another phase transition was observed related to the β → γ phase.

Fig 3.10 (c) shows the cooling cycle of cit-$BiCe_{0.13}VO$ with emphases at 2θ ≈ 20 ° and 40 ° angles to highlight the peak evolution from doublets to singlets peaks which was evident of a phase transition and stabilization of the γ-phase. At the highest temperature, the sample crystallinity and purity improved and peaks were narrower with high intensity (see fig 3.10 (a)). when the sample was cooled back to room temperature the α-phase reappeared at 350 °C

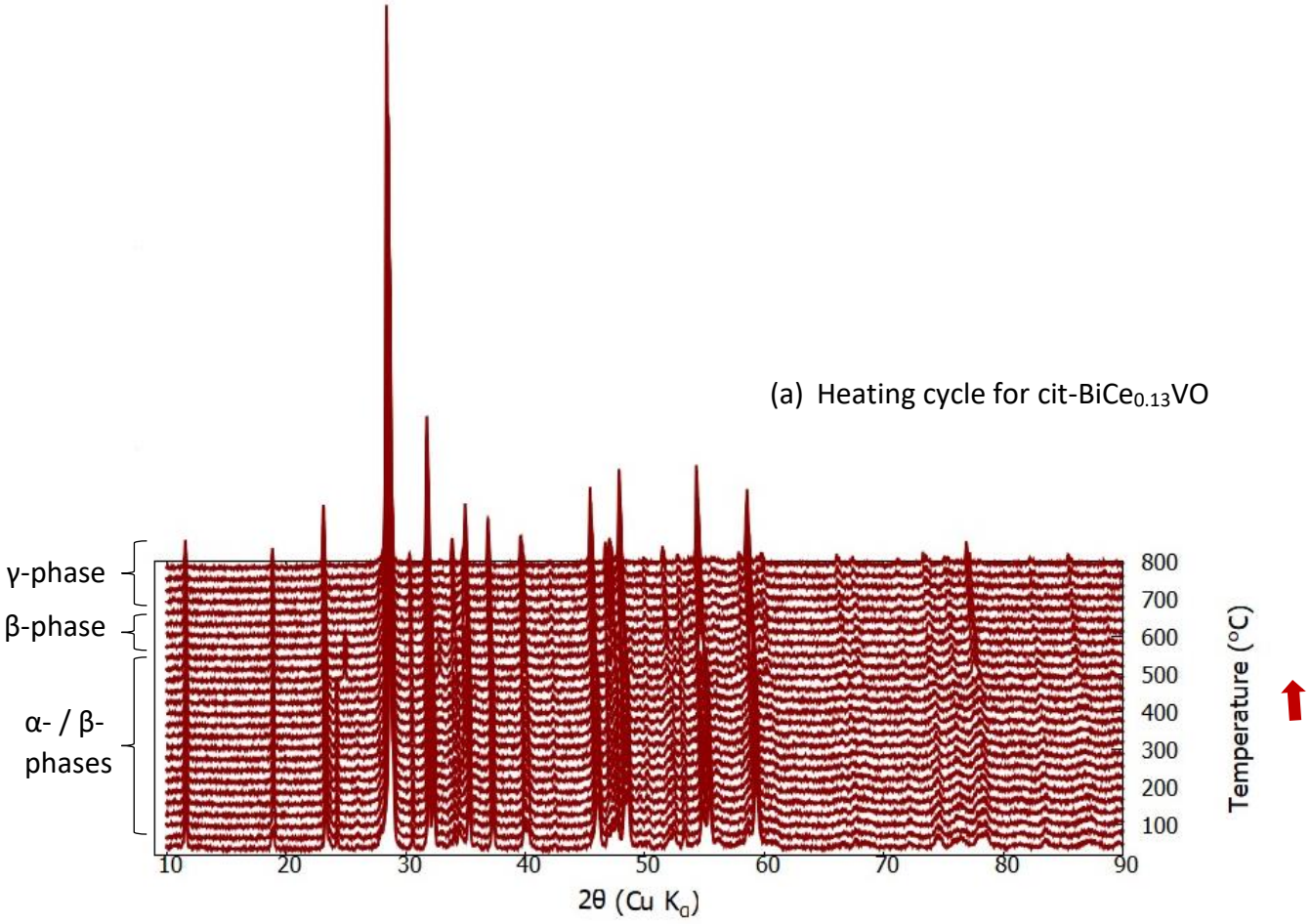

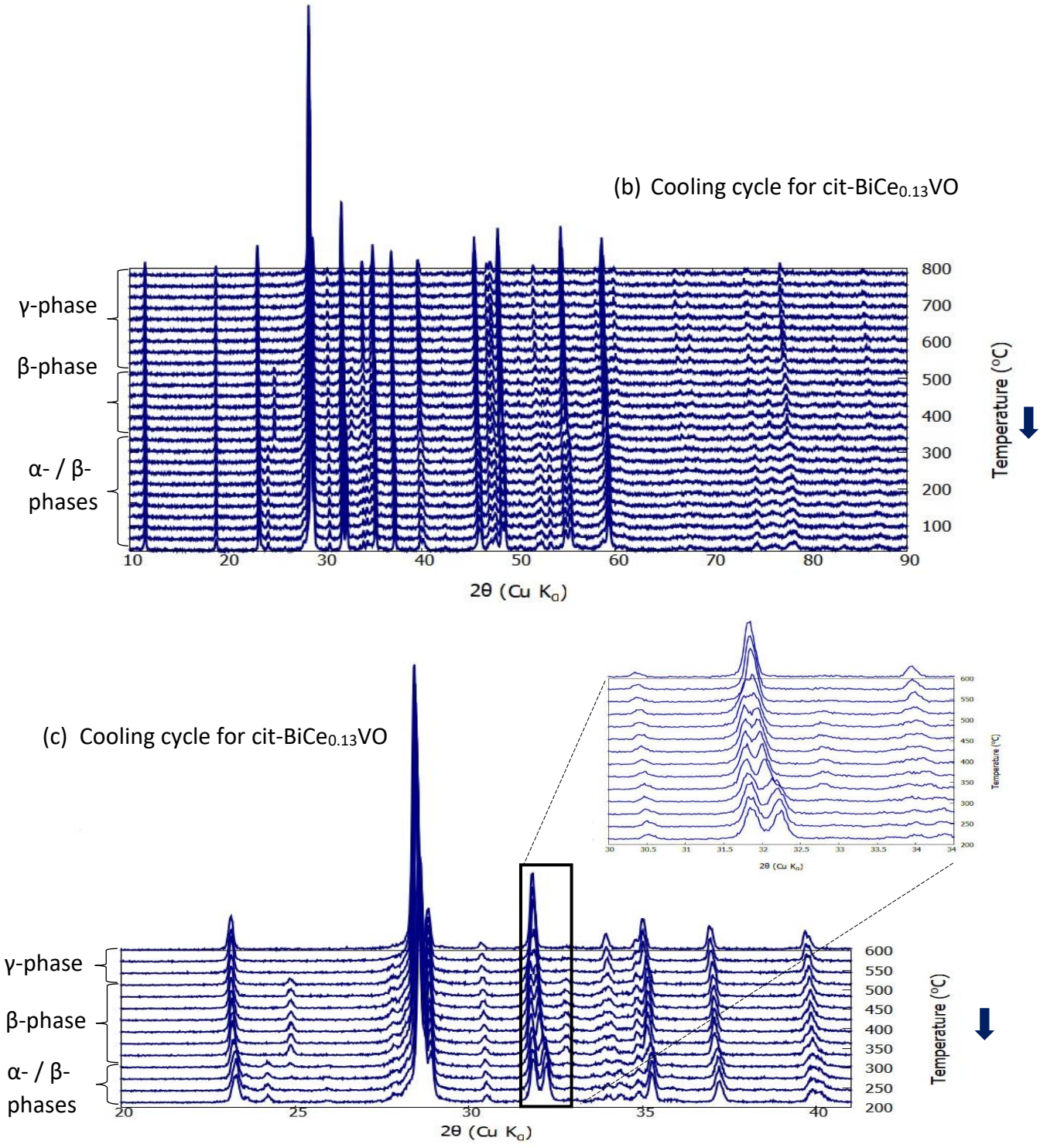

Figure 3.10: VT-XRD of cit-$BiCe_{0.13}VO$ under air atmosphere.

The a- and c-lattice parameters changed abruptly with increasing/decreasing temperatures as a result of the reversible phase transitions from α → β → ɣ (see fig 3.11). The b-lattice parameter had a gradual slope with increasing temperatures indicating the stabilisation of the ɣ-phase.

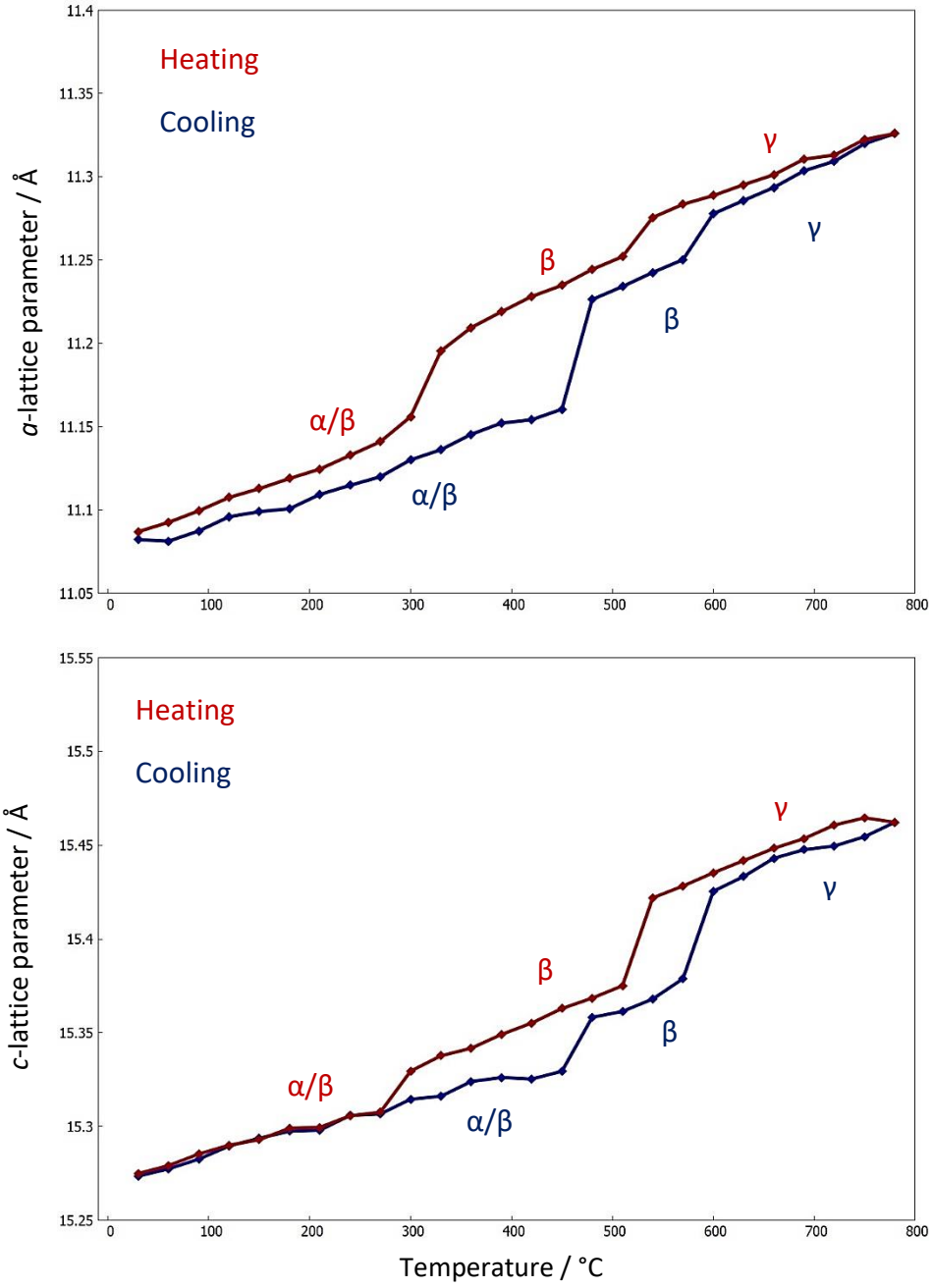

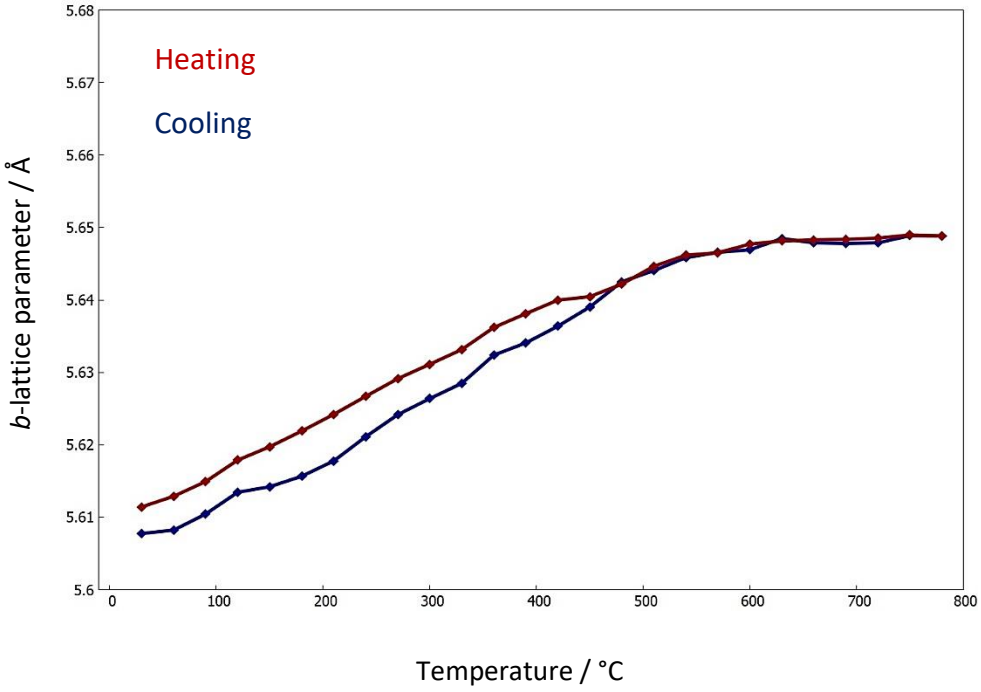

Figure 3.11: Refined lattice parameters of cit-$BiCe_{0.13}VO$ as a function of temperature.

The Raman spectra in fig 3.12 shows different V-O bond and coordination symmetries in cit-$BiCe_{0.13}VO$ and cit-$BiCe_{0.28}VO$ samples. It was observed that due to doping the Ce-O bonds affected neighbouring V-O vibrations and produced complex Raman spectra. The α-phase bands were observed at 366 cm^{-1}, 300 cm^{-1} and 137 cm^{-1} for both samples meanwhile the intense asymmetry band at 826 cm^{-1} and 915 cm^{-1} provided evidence of the β-phase. Usually, one or two Raman bands are observed between 700 cm^{-1} – 900 cm^{-1} associated with VO_4 tetrahedra structures but due to Ce^{4+} doping multiple peaks were observed indicating that Ce^{4+} substituted for V^{5+} lattice sites in the crystal structure.

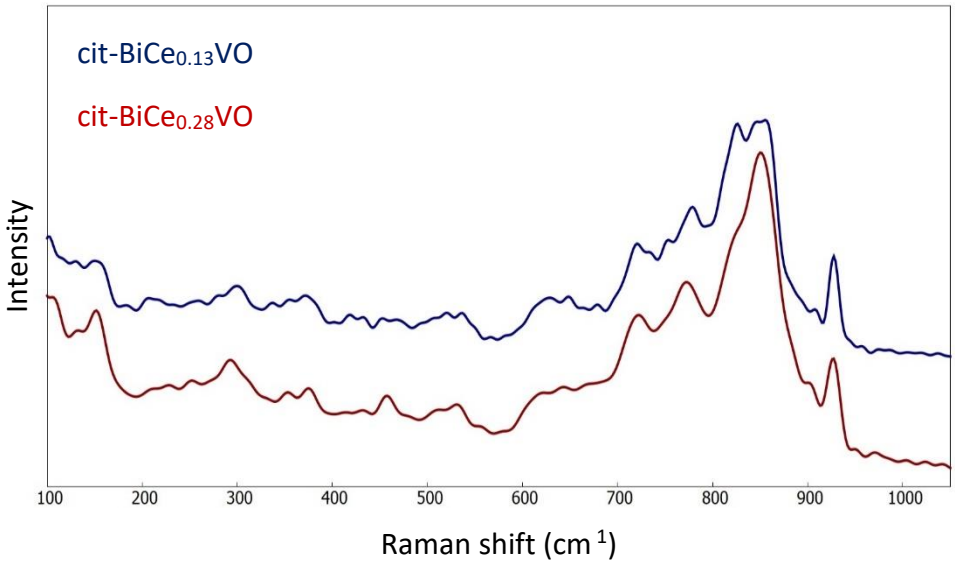

Figure 3.12: Raman spectra of cit-$BiCe_{0.13}VO$ and cit-$BiCe_{0.28}VO$ at room temperature (laser power 0.04 mW).

The variable temperature Raman data of cit-$BiCe_{0.18}VO$ is presented in fig 3.13 revealing the α-phase bands at 300 cm^{-1} and 250 cm^{-1} gradually disappearing with increasing temperatures. The shift of the band at 900 cm^{-1} which gradually merged with the intense peak at 820 cm^{-1} was a characteristic feature that showed the formation of the γ-phase.

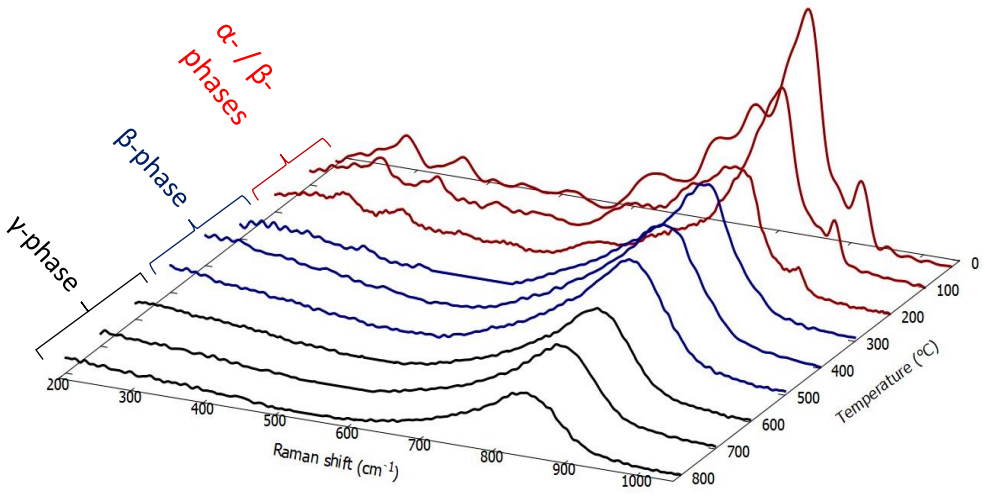

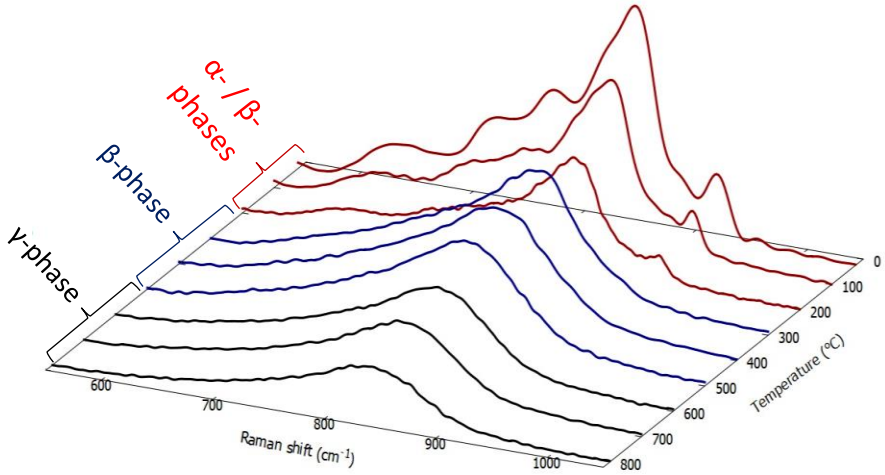

Figure 3.13: VT-Raman spectrum of cit-$BiCe_{0.18}VO$ under oxygen atmosphere.

3.3.3 sol- $BiCu_{0.10}VO$ and sol-$BiCu_{0.10}Ce_{0.10}VO$ results

The PXRD patterns of sol-$BiCu_{0.10}VO$ and sol-$BiCu_{0.10}Ce_{0.10}VO$ samples are shown in fig 3.14 illustrating the annealing process of both samples using the solid-state method. It was determined that both samples peak shapes and intensities improved with each heat treatment (HT) which lasted for ≈12 hours at 700 °C in the furnace with intermediate 45 minutes grinding of the sample. Both materials had quite similar PXRD patterns with minor differences like the β-phase of sol-$BiCu_{0.10}VO$ had sharper and intense peaks compared to sol-$BiCu_{0.10}Ce_{0.10}VO$. It was clear that doping sol-$BiCu_{0.10}VO$ with Ce^{4+} had resulted in the local structural disturbance that poorly affected sol-$BiCu_{0.10}VO$ crystallinity.

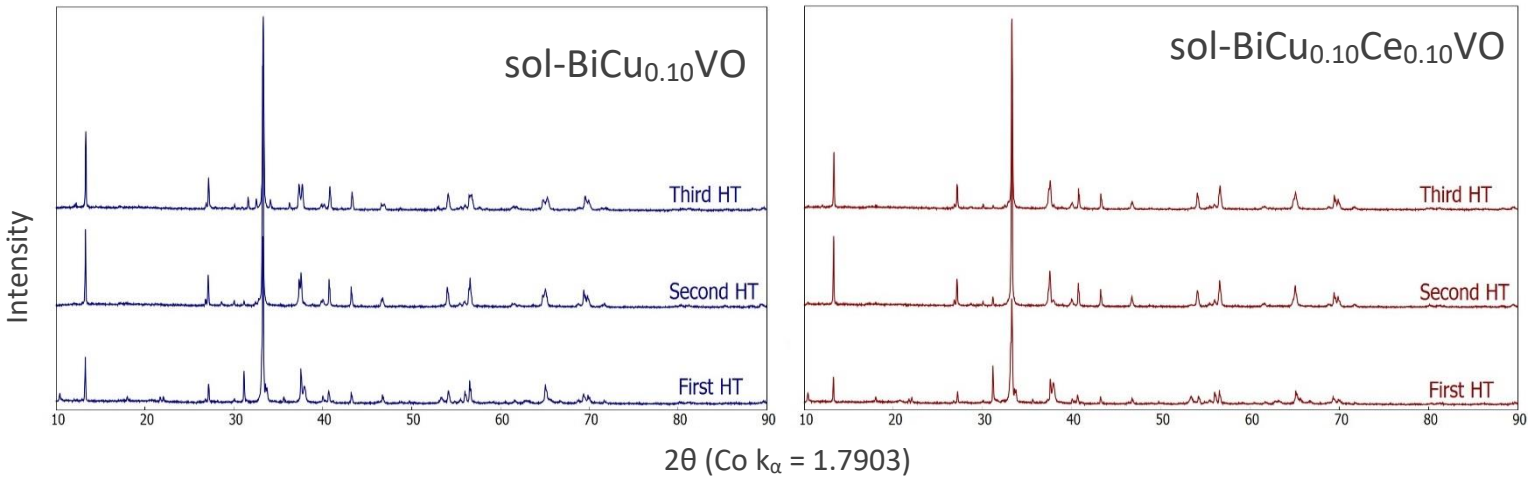

Figure 3.14: Solid-state annealing process of sol-$BiCu_{0.10}VO$ and sol-$BiCu_{0.10}Ce_{0.10}VO$.

The Rietveld refinement of sol-$BiCu_{0.10}VO$ at room temperature is shown in fig 3.15. It was determined that both samples were mostly β-phase at room temperature with no detection of the α-phase present (with the chemical composition of $BiVO_4$). In addition, the γ-phase was identified but overlapped with the β-phase peaks making it difficult to distinguishing between the β- and γ- phases separately.

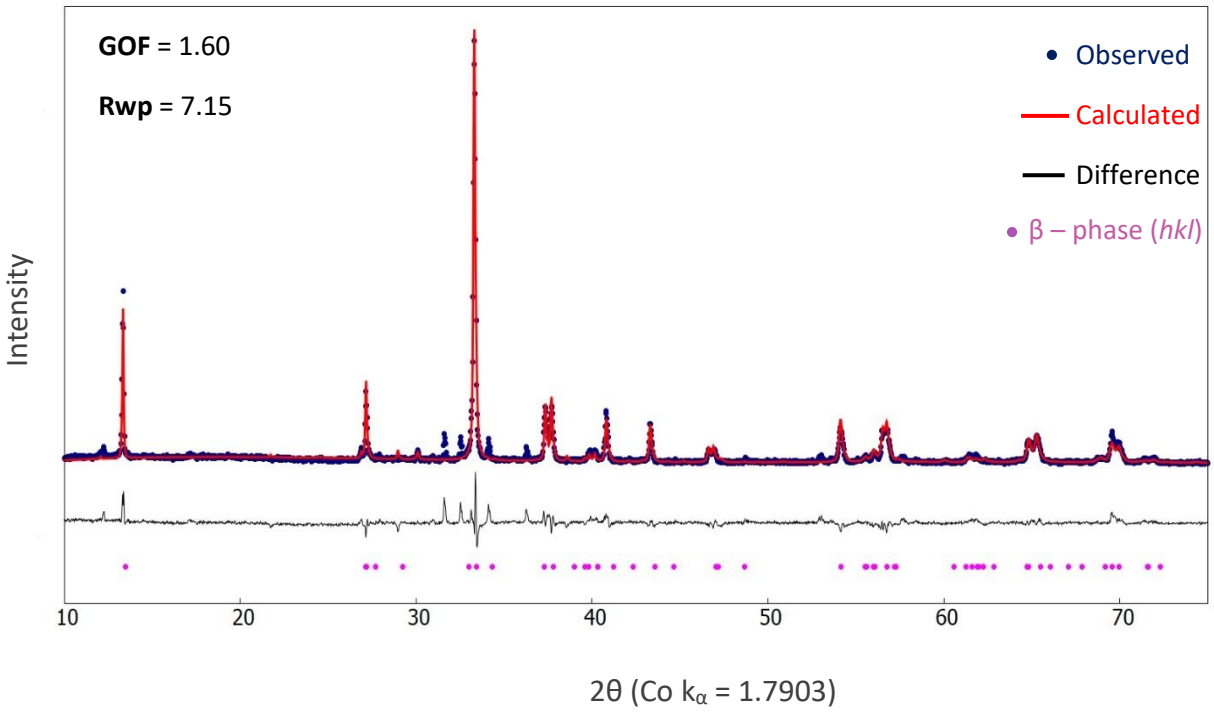

Figure 3.15: Room temperature Rietveld refinement plot of sol-$BiCu_{0.10}VO$.

It was suspected that the absences of the α-phase in sol-$BiCu_{0.10}VO$ and sol-$BiCu_{0.10}Ce_{0.10}VO$ samples was due to using the solid-state method. As such the citrate (sol-gel) method was employed to prepare cit-$BiCu_{0.10}VO$ and cit-$BiCu_{0.10}Ce_{0.10}VO$ samples and table 3.3 shows the weighed masses for the synthesis.

Table 3.3: Weighed masses for the synthesis of cit-$BiCu_{0.10}VO$ and cit-$BiCu_{0.10}Ce_{0.10}VO$ using the citrate method.

Targeted composition	*Sample*	*$Bi(NO_3)_3{\cdot}5H_2O$ /(g)*	*$Ce(NO_3)_3{\cdot}6H_2O$ /(g)*	*$Cu(NO_3)_2{\cdot}3H_2O$ /(g)*	*$VOCl_3$ /(µl)*	*Citric acid /(g)*
$Bi_2Cu_{0.10}V_{0.90}O_{5.35}$	cit-$BiCu_{0.10}VO$	1.9026	0.0	0.0424	166	10.1210
$Bi_2Cu_{0.10}Ce_{0.10}V_{0.80}O_{5.35}$	cit-$BiCu_{0.10}Ce_{0.10}VO$	1.6356	0.0762	0.0474	148	10.3873

As anticipated the α-phase peaks were detected in cit-$BiCu_{0.10}VO$ and cit-$BiCu_{0.10}Ce_{0.10}O$ denoted with asterisks on fig 3.16 PXRD data. Moreover, the α-phase peaks became more prominent after annealing the samples at 780 °C for 12 hours illustrating that the synthesis of sol-$BiCu_{0.10}VO$ and sol-$BiCu_{0.10}Ce_{0.10}VO$ using the solid-state method significantly reduced the formation of the α- phase.

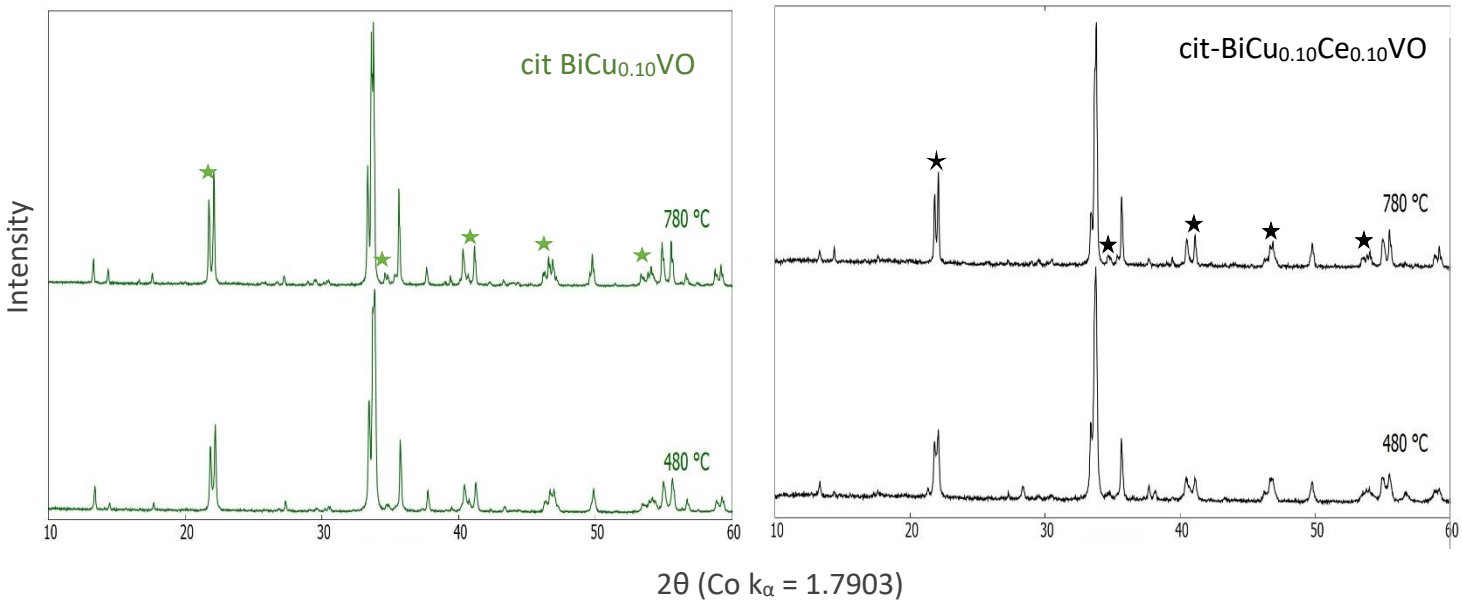

Figure 3.16: Room temperature PXRD patterns of cit-$BiCu_{0.10}VO$ and cit-$BiCu_{0.10}Ce_{0.10}VO$ using the sol-gel method.

The STA diagrams of sol-$BiCu_{0.10}VO$ and sol-$BiCu_{0.10}Ce_{0.10}VO$ had peaks at ≈420 °C which according to previous studies indicate a β → γ phase transition or γ' → γ phase transition. The γ' → γ phase transition is from ordered oxygen vacancies to distorted oxygen vacancies. In this study, the STA peaks were interpreted as the β → γ phase transition considering that the samples were predominantly β-phase at room temperature and not γ'-phase.

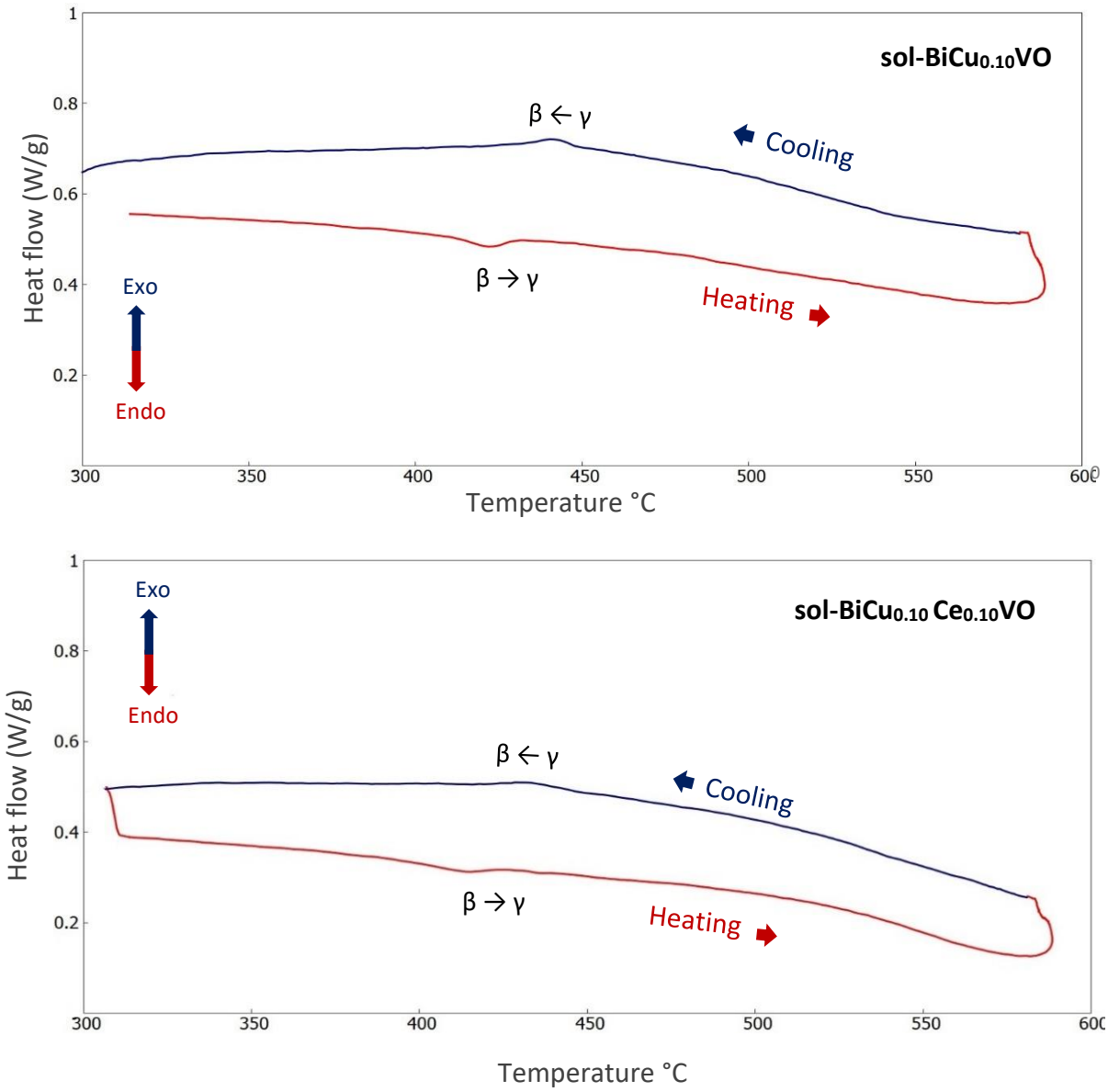

Figure 3.17: STA diagram of sol-$BiCu_{0.10}VO$ and sol-$BiCu_{0.10}Ce_{0.10}VO$ under oxygen atmosphere.

The Raman spectra of sol-$BiCu_{0.10}VO$ at room temperature had low frequency shift of the V-O stretch at 855 cm^{-1} usually this band is positioned at 820 cm^{-1}. The two bands at 120 cm^{-1} and 300 cm^{-1} were V-O bonds assigned to the bending modes. The Raman bands which were visible within sol-$BiCu_{0.10}VO$ sample disappeared with 10% mol Ce^{4+} doping as a result of the high distortion of the VO_4 stretch modes.

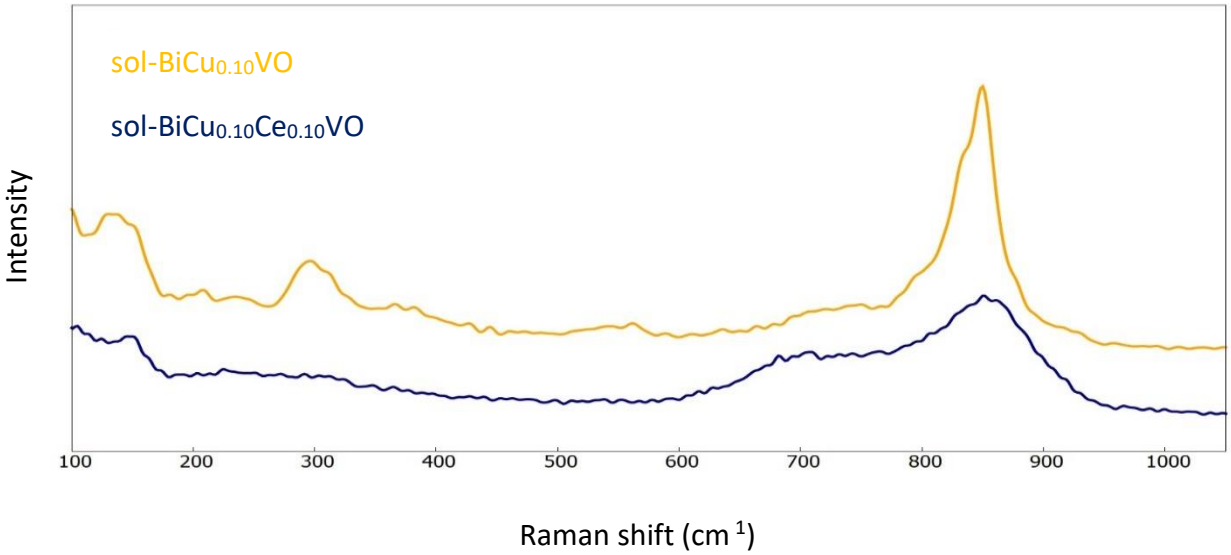

Figure 3.18: Raman spectrum of sol-$BiCu_{0.10}VO$ and sol-$BiCu_{0.10}Ce_{0.10}VO$ at room temperature (laser power = 0.04mW).

3.4 Conclusion

In conclusion, it was determined that cit-BiVO was a multi-phase material with two different α-phases one due to the decomposition of the β-phase with a chemical composition of $BiVO_4$ and this α-phase overshadowed the other cit-BiVO α-phase with the chemical composition of $Bi_2VO_{5.5}$. It was also determined that by doping cit-BiVO with increasing Ce^{4+} concentration the α-phase gradually disappeared and the γ-phase was stabilized at higher temperatures (>600°C). It is common to find the α-phase ($BiVO_4$) in any BiMeVOx material since the α-phase is the natural mineral of bismuth vanadate thus likely to be the preferred phase. It was also established that it required less energy to transition from the α→β phase with increasing Ce^{4+} concentration and even far less energy was required for β→γ phase transition. The Raman spectroscope confirmed that Ce^{4+} ions substituted for V^{5+} lattice sites and did not deposit as coating on cit-BiVO.

The VT-XRD data showed that in terms of the phase transition, the *a*- and *c*-lattice parameters were the most affected lattice parameters with changing temperatures compared to the *b* lattice parameter giving some insight in the mechanism of phase transition in these materials.

It was further proven that by doping sol-$BiCu_{0.10}VO$ with 10% mol Ce^{4+} the crystal structure of sol-$BiCu_{0.10}VO$ was poorly affected and the sol-gel method increased the formation of the α-phase.

Chapter 4

Determination of oxide-ion conductivity.

4.1 Introduction and outline.

In chapter 4, electrochemical impedances was conducted on synthesized samples at different temperatures. As previously mentioned that a good ionic conductor/electrolyte is able to transport O^{2-} ions from the cathode to the anode in SOFCs at low temperatures through oxygen vacancies. In this study, cit-BiVO and sol-$BiCu_{0.10}VO$ samples were doped with different concentrations of Ce^{4+} ions to increase the amount of oxygen vacancies in the materials thus improve the material ionic conductivity.

4.2 Experimental procedure.

4.2.1 Preparation of pellets.

All synthesized samples in chapter 3 were uniaxially pressed at 39.2 MPa into pellets using a 5 mm diameter die for 1 minute, then sintered at 750 °C for 24 hours using ceramic crucibles in a tube furnace. The average pellet thickness and radius were between ≈ 0.53 mm and ≈2.52 mm respectively and no polyvinyl binder was used to make the pellets.

4.2.1 EIS measurement.

The BioLogic MTZ-35 frequency response analyser coupled to a BioLogic HTF-1100 furnace - interfaced to a computer running the MT-Lab software (version 1.21) was used to measure the impedance of the pellet at increasing temperatures. The HTSH-1100 sample holder had two platinum discs of similar diameter to the pellet and the spring-loaded system was used to tighten the pellet between the platinum discs before carefully placing the sample holder inside the furnace. Prior to impedance measurement, open- and short-circuit compensations were performed to remove stray and background impedances due to cell cables and the

sample holder. The frequency range was set between 2.5 MHZ – 0.05 Hz and the amplitude was set at 10 mV. Measurements were taken every 50 °C from 250 °C–750 °C with 30 minutes dwell time at each step. EQM modelling was performed using the EC-Lab v11.21 program equipped with the zfit analytical tool.

The impedance data from the BioLogic MTZ-35 measured the bulk and grain boundary resistances of each sample at a certain temperature and those resistance values were used to calculate the bulk (G) and grain boundary (GB) ionic conductivity using the following formulas.

$$\sigma_G = \frac{4e}{\pi d^2 R_G}$$ Bulk ionic conductivity

$$\sigma_{GB} = \frac{4e}{\pi d^2 R_{GB}}$$ Grain boundary ionic conductivity

$$\sigma_{Tot} = \frac{4e}{\pi d^2 (R_G + R_{GB})}$$ Total ionic conductivity

Where *e* represents the pellet thickness (mm), d is the pellet diameter (mm), R_G is the bulk resistance and R_{GB} is the grain boundary resistance.

The activation energies of each sample was determined using the Arrhenius equation by rearranging the equation into a linear function. The y-axis represented the log of conductivity and the x-axis represented 1/T with the slope being $-Ea/K_b$. The activation energy was the slope of the line divided by the Boltzmann constant = 1.38 x 10^{-23} J/K.

$$\sigma = \sigma_o e^{\left(\frac{-E_a}{K_b T}\right)}$$ Arrhenius equation

$$In(\sigma) = \left(\frac{-E_a}{K_b}\right) T + In(\sigma_o)$$ Arrhenius linear equation

Chapter 4

4.3 Results and discussion.

4.3.1 cit-BiVO and cit-$BiCe_{0.13}VO$ results.

The Nyquist plots in fig 4.1 shows the measured impedance of cit-BiVO, cit-$BiCe_{0.13}VO$ and cit-$BiCe_{0.28}VO$ pellets at increasing temperatures from 250 °C – 750 °C . It was observed at 350 °C that the Nyquist plots for cit-BiVO and cit-$BiCe_{0.13}VO$ samples had two semicircles, the first semicircle at high frequency was due to the bulk impedance of the sample and the second semicircle at low frequency was impedance due to the grain boundary of the sample[2]. However, the two semicircles (bulk and grain) overlapped with each other as temperature increased. Cit-$BiCe_{0.28}VO$ had only one semicircle at 350 °C indicating the bulk impedance of the sample and as temperature increased a curved line known as the diffusion line was observed.

Upon further increasing the temperature in the furnace and still measuring impedance the two semicircles of cit-BiVO and cit-$BiCe_{0.13}VO$ disappeared and a curved diffusion line was observed above 550 °C. The diffusion line was impedance due to the motion of O^{2-} ions through the electrolyte/pellet and the line slowly curved downwards at 750 °C as a result of the bounded nature of the system where O^{2-} ions mobility in the pellet were limited beyond the electrodes.

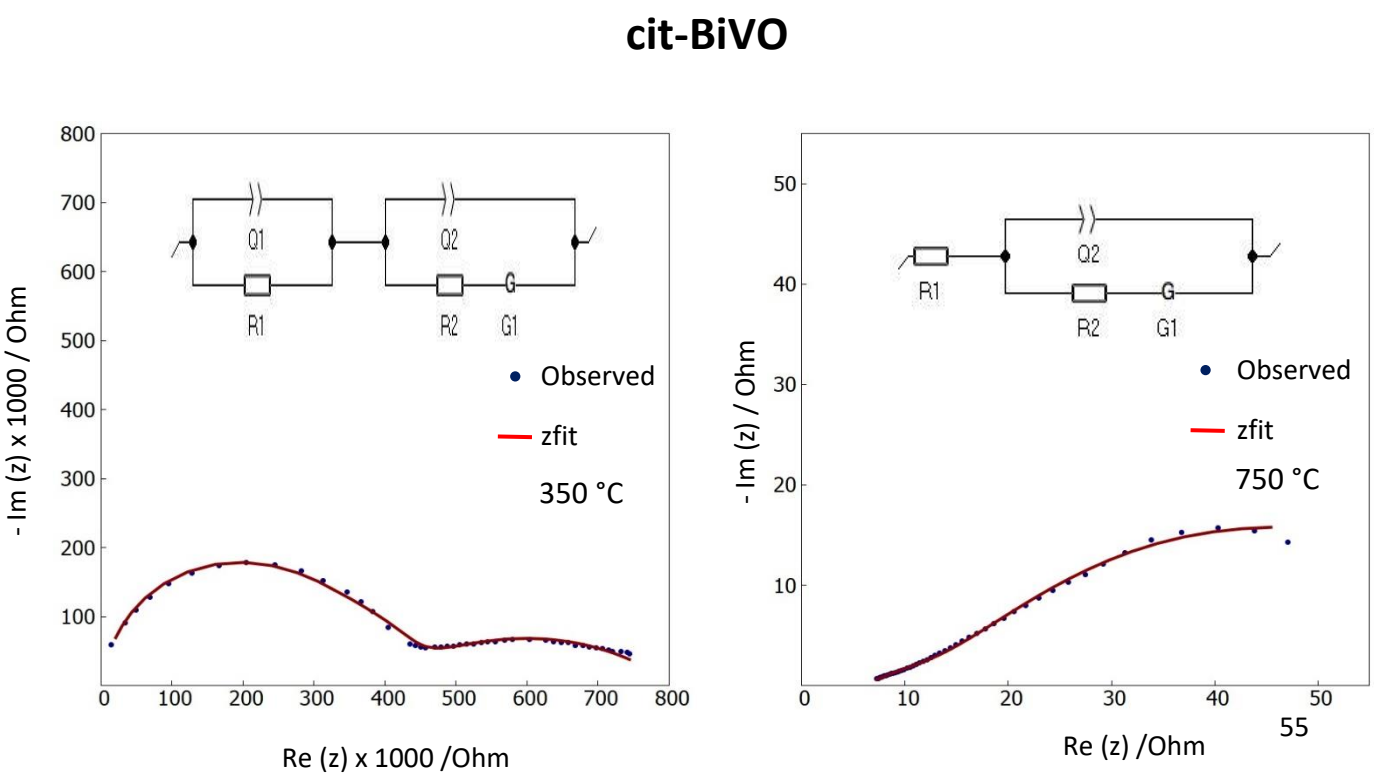

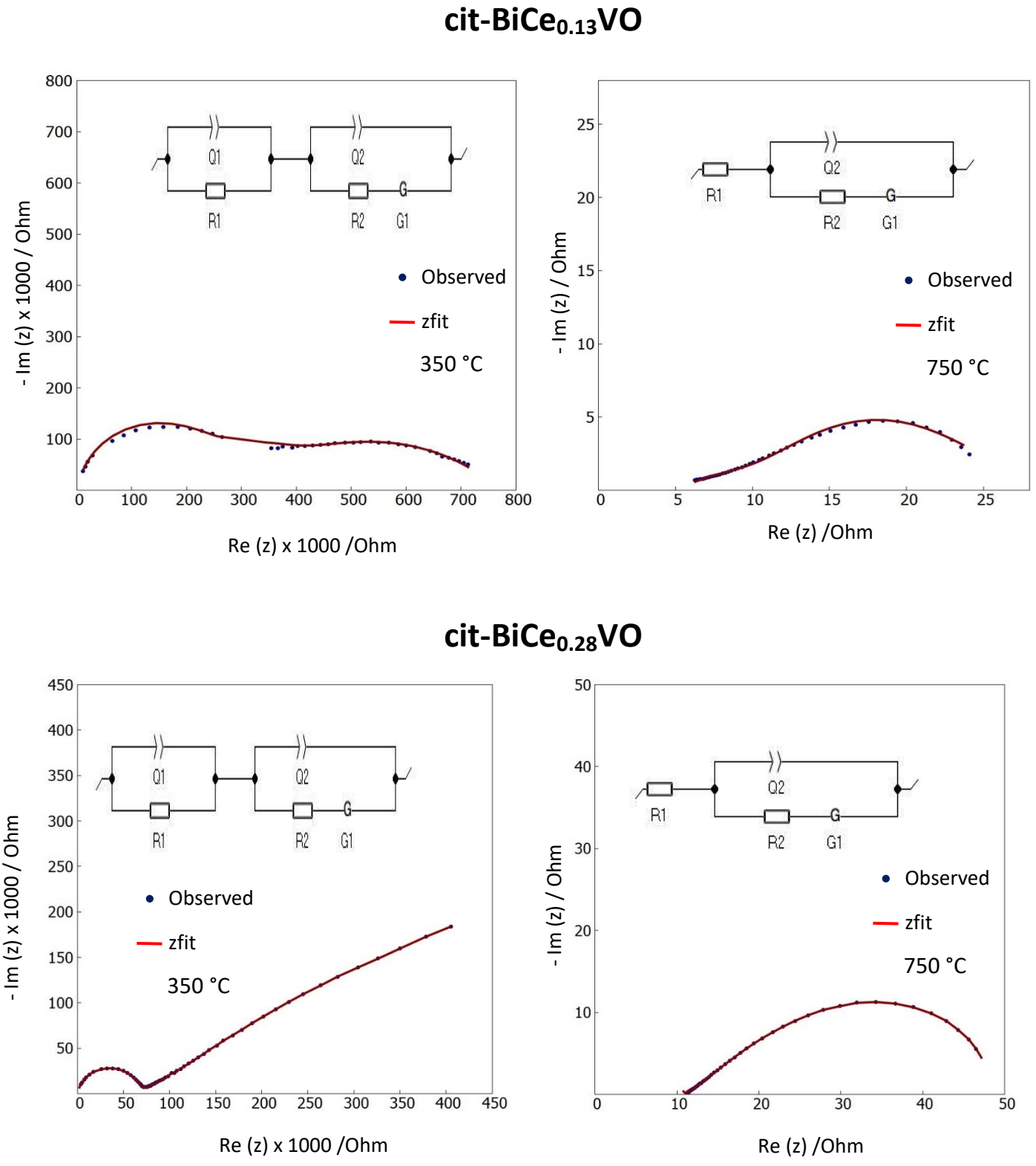

Figure 4.1: The Nyquist plots of cit-BiVO, cit-BiCe$_{0.13}$VO and cit-BiCe$_{0.28}$VO at 350 °C - 750 °C.

The electric equivalent circuits (EQCs) between 250 °C and 550 °C were modelled with a two-part circuit in series (see figure 4.1): R1 stands for the bulk resistance of the sample and R2 represents the grain boundary resistance of the sample. Q1 and Q2 stands for the constant phase element representing the capacitance behaviour in the bulk and grain boundary respectively. The constant phase element (CPE) replaced the capacitance (C) element in the circuit since the two semi-circles were depressed and it accounted for the charge transfer. G1 represented the Gerischer impedance and shows the ionic diffusion and accounted for the downward curvature of the diffusion line in Nyquist plots.

The EQCs between 600 °C and 750 °C were modelled without the Q1 component since the capacitance of the bulk sample disappeared only showing the resistive behaviour of the sample. Fig 4.2 shows the Arrhenius plots for the thermal cycle of cit-BIVO. Three main different regions were determined on the graph having different activation energies as a result of the phase transformation from α → β → γ phases.

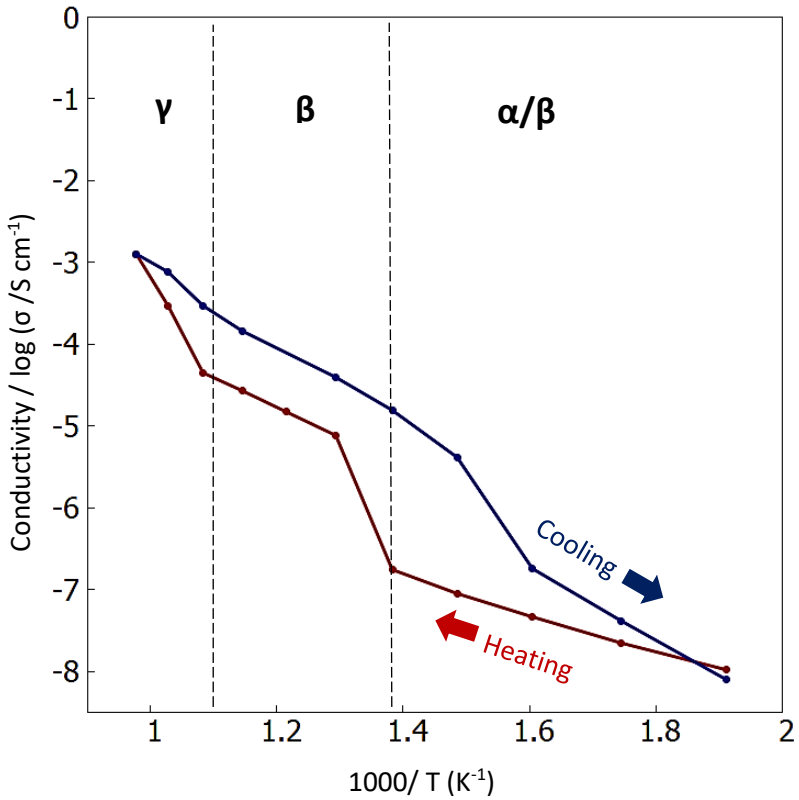

Figure 4.2: Arrhenius plot of cit-BiVO.

The phase transition from α → β → γ was also observed for doped samples (cit-$BiCe_xVO$). However, doped samples Arrhenius plot exhibited a curved-like feature. The ionic conductivity of cit-$BiCe_xVO$ was model using the same EQCs as cit-BiVO. In this study, it was declared that ionic conductivity would increase with increasing Ce^{4+} dopant concentrations since the sample would have more oxygen vacancies but according to the Arrhenius plots in fig 4.3 this trend held except for cit-$BiCe_{0.18}VO$.

It was suspected that the conductivity of cit-$BiCe_{0.18}VO$ might have deviated from the trend since cit-$BiCe_{0.18}VO$ had the biggest bulk resistance compared to other samples. cit-$BiCe_{0.18}VO$ was treated as an outlier in this study and more work must be conducted to investigate this outcome.

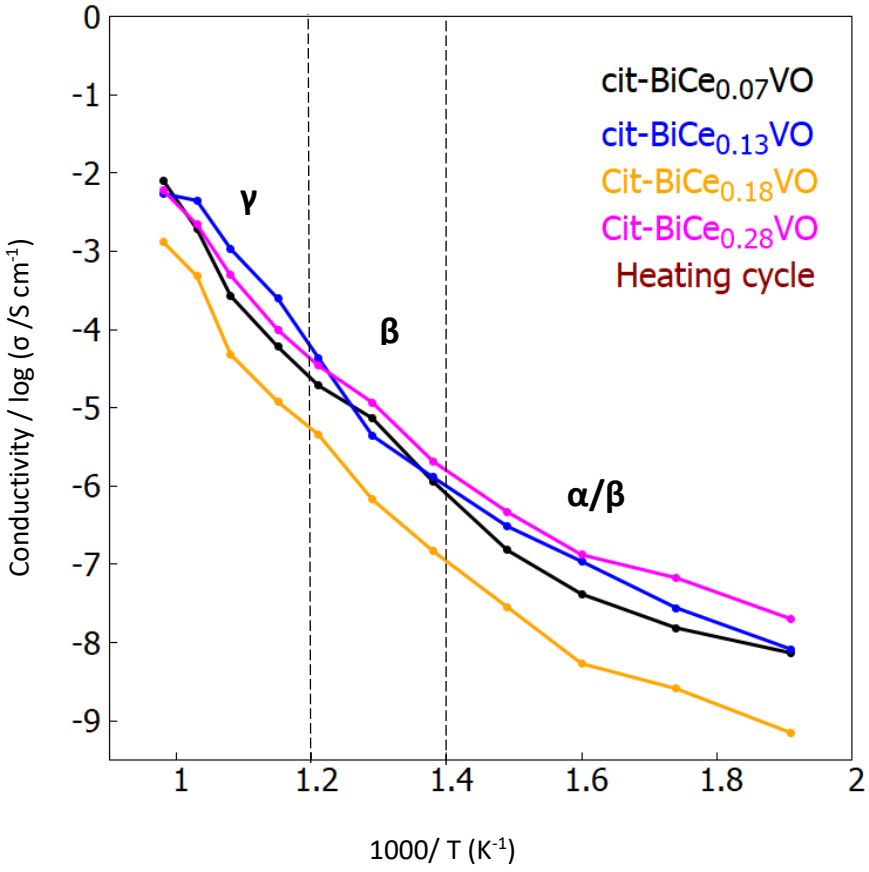

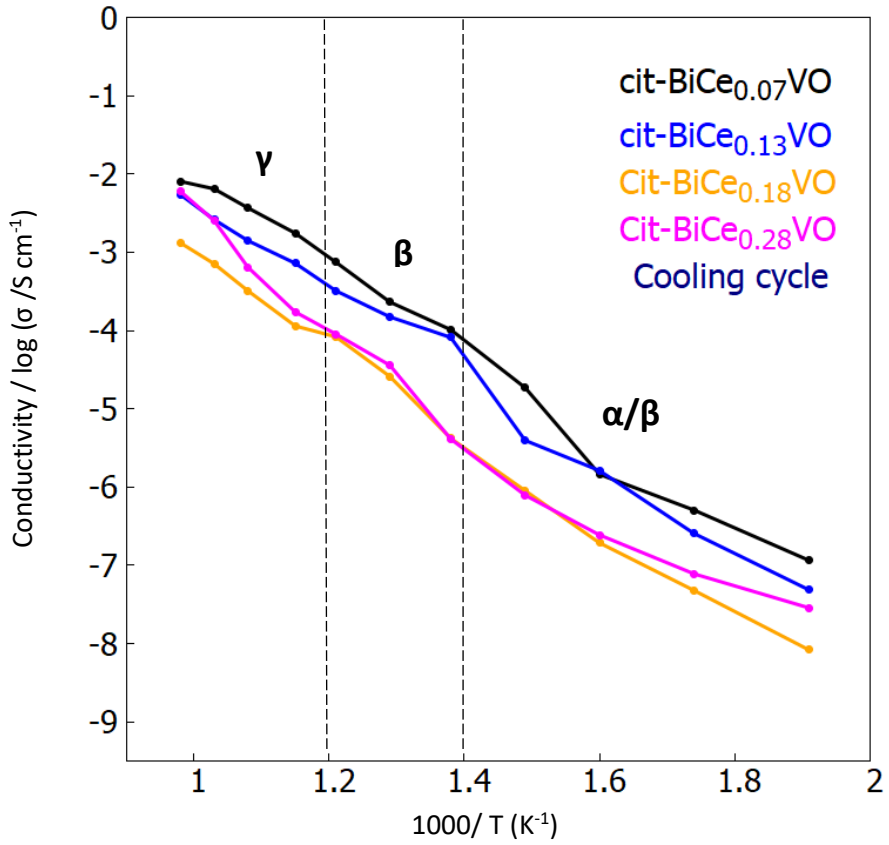

Figure 4.3: Arrhenius plots of cit-$BiCe_xVO$ ($0.07 \leq x \leq 0.28$).

The activation energy (E_a) gives information about the mobility and amount of free oxygen vacancies in the material including the different mechanism of conductivity[6]. At lower temperatures (< 500 °C) the E_a is required to free vacancies in the structure and at higher temperatures the E_a energy is required for the mobility of vacancies[6]. Table 4.1 shows the E_a of different pellets and the goodness of fit (R^2). It was determined that the E_a changed with increasing temperatures due to the phase transition from α → β → γ phases. As the concentration of Ce^{4+} increased, the E_a for the β → γ phase transition decreased see table below.

Table 4.1: Calculated activation energies of pellets during the heating cycle.

sample	Ea / eV (250 °C– 450 °C)	R^2	Ea / eV (500 °C– 600 °C)	R^2	Ea / eV (650 °C– 750 °C)	R^2
cit- BiVO	0.25	0.998	0.39	0.999	1.78	0.998
cit- $BiCe_{0.07}VO$	0.42	0.998	0.57	0.999	1.50	0.999
cit- $BiCe_{0.13}VO$	0.44	0.990	0.72	0.992	1.36	0.991
cit-$BiCe_{0.18}VO$	0.42	0.999	0.65	0.998	1.46	0.998
cit- $BiCe_{0.28}VO$	0.39	0.995	0.64	0.995	1.40	0.996

4.3.2 sol-$BiCu_{0.10}VO$ and sol-$BiCu_{0.10}Ce_{0.10}VO$ results

The Nyquist plots of sol-$BiCu_{0.10}VO$ and sol-$BiCu_{0.10}Ce_{0.10}VO$ samples are shown in figure 4.4. The plot for sol-$BiCu_{0.10}VO$ only showed the diffusion line indicating the material good ionic conductivity and the plot for sol-$BiCu_{0.10}Ce_{0.10}VO$ first had a semicircle at high frequency due to the bulk impedance and a diffusion line appeared at higher temperatures. The EQCs used to model cit-BiVO and cit-$BiCe_xVO$ ($0.04 \leq x \leq 0.28$) conductivity was applied to model sol-$BiCu_{0.10}VO$ and sol-$BiCu_{0.10}Ce_{0.10}VO$ samples.

Previously, the Raman spectra showed that the crystal structure of sol-$BiCu_{0.10}Ce_{0.10}VO$ was highly destabilised and the Arrhenius plot in fig 4.5 confirmed this observation where the conductivity of sol-$BiCu_{0.10}Ce_{0.10}VO$ was significantly lower than sol-$BiCu_{0.10}VO$. According to literature, the fully disordered γ – phase of sol-$BiCu_{0.10}VO$ exists at very high temperatures and prior to this phase a more ordered γ′ – phase exists[2]. The combined PXRD, STA and Raman spectroscopy data were insufficient to justify the existence of the γ′ – phase but it is worth pointing it out that the step changed observed between 600 °C – 700 °C in fig 4.5 could be associated with the γ′ → γ phase transition.

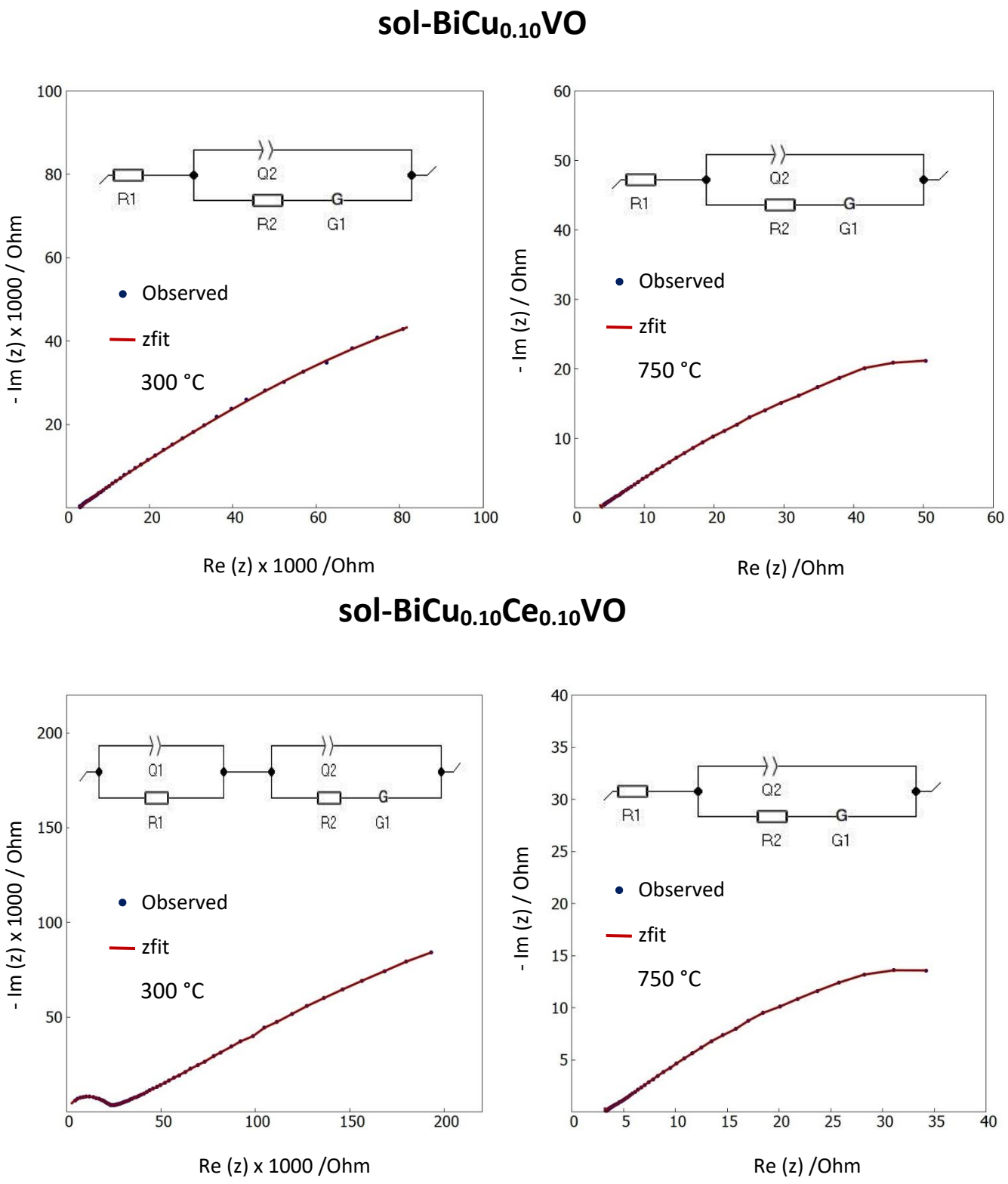

Figure 4.4: The Nyquist plots of sol-$BiCu_{0.10}VO$ and sol-$BiCu_{0.10}Ce_{0.10}VO$.

The Arrhenius plot of sol-$BiCu_{0.10}VO$ showed an increase in conductivity with increasing temperature and at 460 °C the β → γ phase transition was noted. After 600 °C the material conductivity changed and a curved line was observed (see fig 4.5). This feature was prominent in sol-$BiCu_{0.10}Ce_{0.10}VO$ and could be associated with the γ' → γ phase transition. It was determined that the ionic conductivity of sol-$BiCu_{0.10}Ce_{0.10}VO$ was ≈11% lower than sol-$BiCu_{0.10}VO$ between 300 °C – 600 °C upon heating but notice how the two samples had comparable conductivity upon cooling.

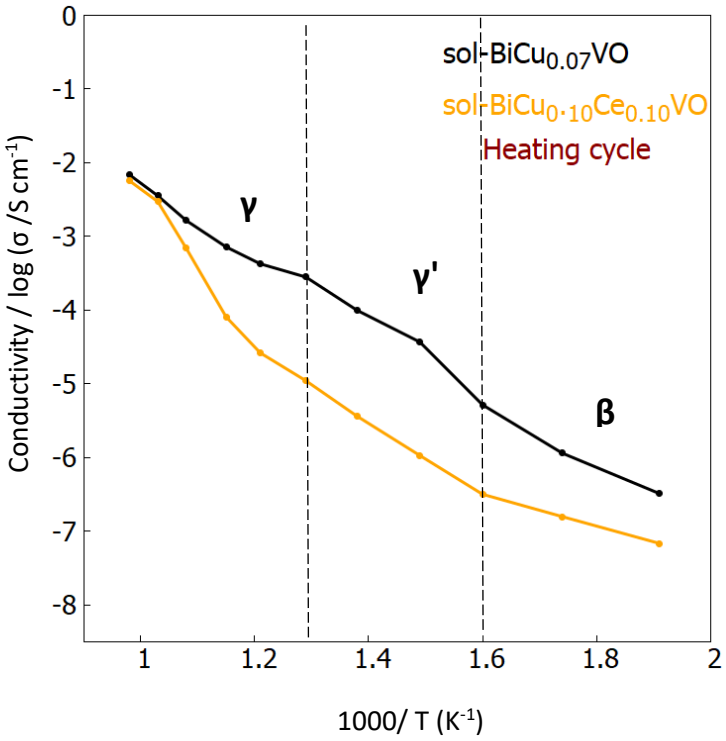

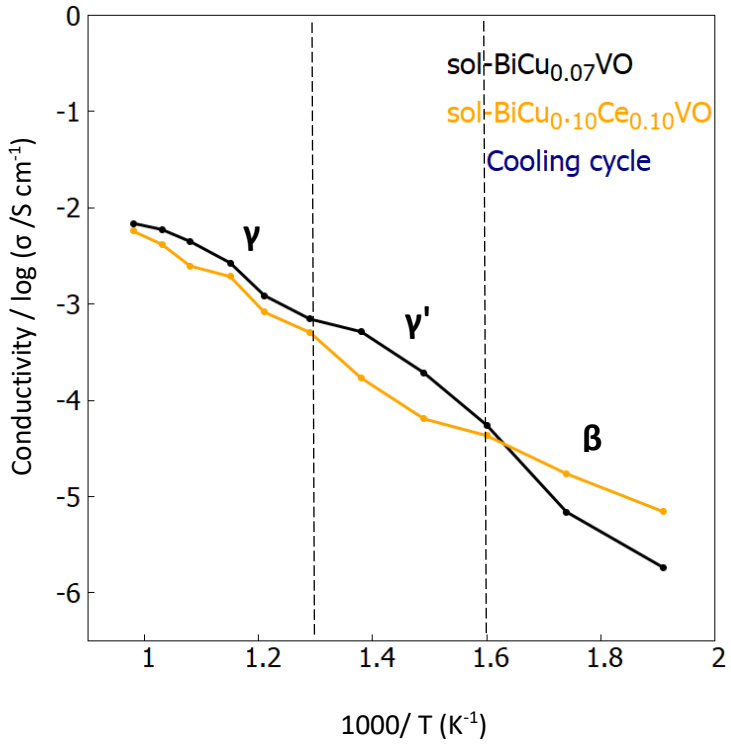

Figure 4.5: Arrhenius plots of sol-$BiCu_{0.10}VO$ and sol-$BiCu_{0.10}Ce_{0.10}VO$.

The heating cycle conductivity of sol-$BiCu_{0.10}VO$ was compared to the citrate method cit-$BiCe_{0.07}VO$ and cit-$BiCe_{0.13}VO$ pellets as seen in fig 4.6. It was observed that sol-$BiCu_{0.10}VO$ had much higher conductivity than both materials showing the advantage of the solid-state method plus doping $Bi_2VO_{5.5}$ with low dopant concentrations of Cu^{2+} compared to Ce^{4+}.

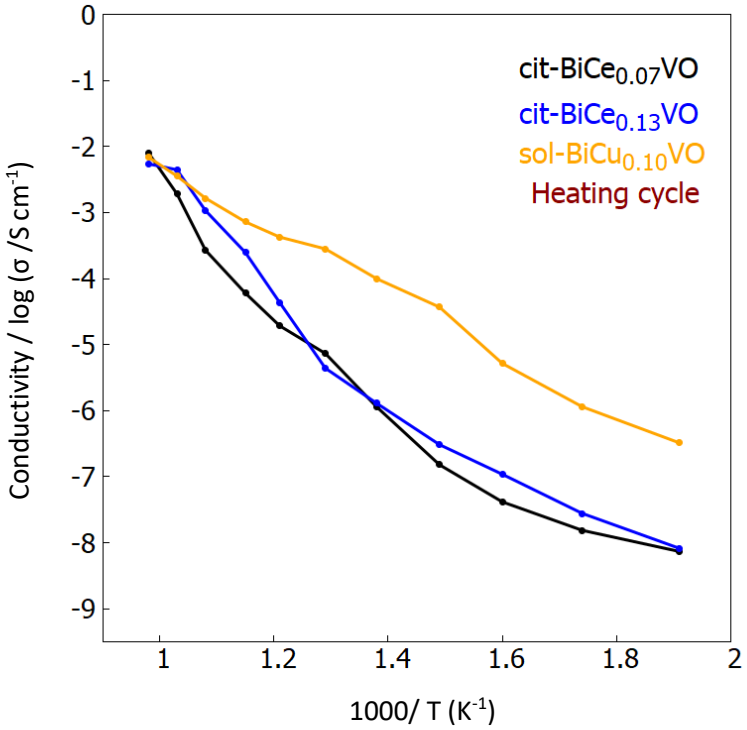

Figure 4.6: Arrhenius plots of cit-$BiCe_{0.07}VO$, cit-$BiCe_{0.13}VO$ and cit-$BiCu_{0.10}VO$.

4.4 Conclusion

In conclusion, the ionic conductivity of cit-BiVO increased with increasing Ce^{4+} dopant concentration except for cit-$BiCe_{0.18}VO$ which had a drop in conductivity possible due to the sample high bulk resistance. sol-$BiCu_{0.10}Ce_{0.10}VO$ ionic conductivity was very low compared to sol-$BiCu_{0.10}VO$ indicating the disadvantage of doping sol-$BiCu_{0.10}VO$ with 10 % mol Ce^{4+} concentration. Published studies have shown that doping sol-$BiCu_{0.10}VO$ with Ti^{4+} or Nb^{5+} had no significant improvement to the material ionic conductivity[6].Additionally, sol-$BiCu_{0.10}VO$ conductivity was very high compared to cit-$BiCe_{0.07}VO$ and cit-$BiCe_{0.13}VO$ samples possibly due to no presence of the α-phase in sol-$BiCu_{0.10}VO$.

Chapter 5

Synchrotron crystallographic data.

5.1 Introduction and outline.

A crystal unit cell arrangement has short- and long-ranged order of atoms which play an important role in the physical and chemical properties of a material[1]. The Pair distribution function (PDF) is a powerful technique that refines the local crystal structures just over a short scale length. This technique is susceptible to various errors that affect the accuracy of the refinement e.g., systematic errors such as termination and statistical errors are introduced in the processing and collection of diffraction data. As such, instrument calibration, proper data collection and reduced methods should be applied to quantify the level of systemic errors for each analysis[2].

Diffraction instruments with better statistics and low levels of background noise at higher Q (reciprocal space) have overall better PDF results even at the expense of decreased resolution[2]. Previous studies have already demonstrated the unique value of using PDF analysis for the study of local orders in polycrystalline and amorphous materials. In this chapter, the crystal data for some of the synthesised samples were analysed using X-ray total scattering and the local crystal structures were determined using the Rietveld method.

5.2 Experimental procedures.

A selected few of the samples synthesised in this study were sent for PDF measurement at the National Synchrotron Light Source II (NSLS-II) using the beamline 28-ID-1. The Small angle X-ray scattering (SAXS) setup was 74 keV, Q_{min} = 0.023 - 1.83 A^{-1} and the beamline featured a (0.25 x 0.25 mm) nominal beam size and a (200 X 200 µm) pixel PerkinElmer area detector used to collect the PXRD data. The sample to detector distance was in the range (204 - 3000 mm) and Tesla superconducting magnet between (0 - 5 T) was used to generate X-ray

wavelength of ~0.1671 Å. Analyses was conducted at room temperature with Teflon capillary tubes used as sample holders. Data was collected as an image on the 2D detector (Ref: fig 2.2) and integrated from 2D into 1D using Fit2D. The Integrated data was a normal powder pattern which in the case of long range analysis was refined. The data was optimized for PDF analysis by further processing into S(Q), then F(Q) and then into G(r). Data acquisition was performed using Python for integration and processing and the Rietveld refinement was performed using Topas v6.0 academia program accordingly.

- XPDFsuite software was employed to remove the background noise, modify the r-min/r-max, r-steps and Qmax/Qmin parameters.
- A Python script was used to convert the G(r) PDF file to xy format then uploaded into JEdit v5.6.0.
- Inside JEdit v5.6.0, the XInsert node TOPAS Durham folder was selected to do a simple Lab Rietveld refinement.
- The background was defined for a Chebyshev polynomial and the zero point parameter was refined.
- The synchrotron wavelength of 0.1671 Å was entered under instrument settings.
- Three cif data files were uploaded to JEdit and Ce^{4+} or Cu^{2+} ions were added respectively with the correct atomic occupancy depending on the sample.
- The Beq values were fixed at Bi^{3+} = 1, V^{5+} = 1, Ce^{4+} = 1, Cu^{2+} = 1 and O^{2-} = 2.5
- The atomic position of O^{2-} ions were refined except for atoms with special atomic position (x,y,z,) = (0,0,0,) if necessary.
- This process was repeated many times until a good fit was achieved shown by a low R_{wp} and GOF values.

5.3 Results and discussion.

5.3.1 **cit-BiVO results.**

The PDF data was collected between 1 Å - 30 Å because below 1 Å it is difficult to observe any well-defined peaks. It was determined using the PDF data that cit-BiVO sample major

phase at room temperature was the β-phase whichwas visualized using VESTA v 4.5.0 (see fig 5.1).

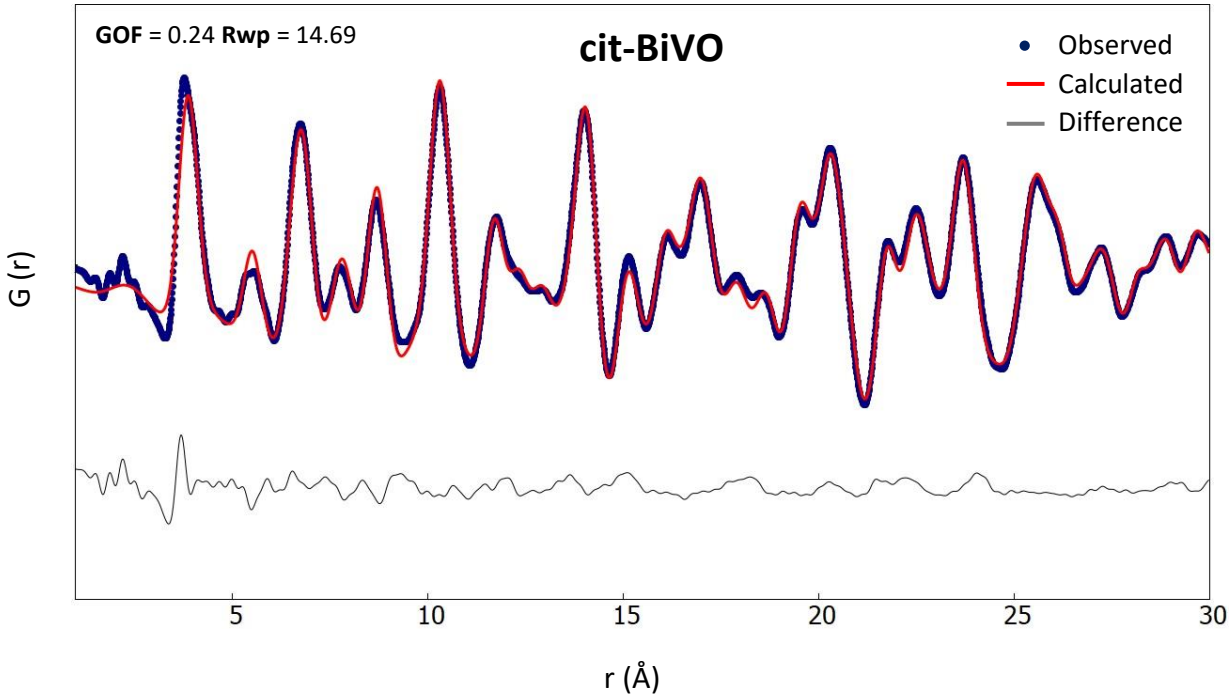

Figure 5.1: PDF analysis of cit-BiVO sample at room temperature.

The interatomic distance density increased with bond length between atoms and it was difficult to identify individual atom-atom pairs past ≈ 5 Å. Cit-BiVO had broad peaks due to the peak overlapping/disorder caused by the sample exhibiting two different phases α- and β-phase at room temperature. The local crystal structure of cit-BiVO β-phase is shown in fig 5.2. Previous studies have depicted the structure of $Bi_2VO_{5.5}$ β-phase consisting of alternating layers of $(Bi_2O_2)^{2+}$ sandwiched between $(VO_6)^{2-}$ sheets which was confirmed in this work (see the diagram below).

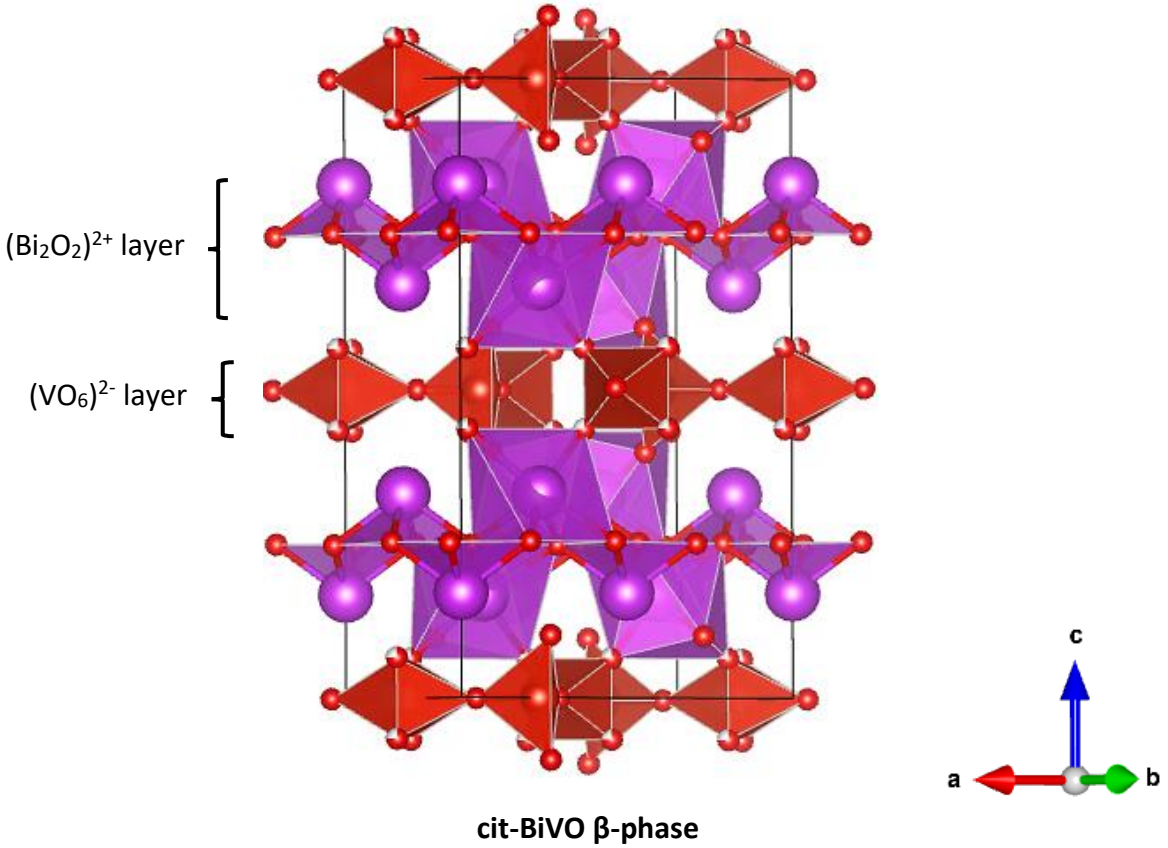

Figure 5.2: Crystal structure of cit-BiVO. The red/white spheres represent oxygen vacancy.

The synchrotron XRD pattern of cit-BiVO sample had better peak resolution and each phase was easily identified compared to the Lab D2 XRD (Ref: fig.3.1).. The distinctive doublet peak associated with the α-phase at 2θ ≈ 2° was clearly visible in synchrotron XRD (see fig 5.3) and this peak gradually disappeared with increasing Ce^{4+} dopant concentration. As mentioned early that cit-BiVO had two different α-phases with different chemical compositions. The $BiVO_4$ α-phase overshadowed the other cit-BiVO α-phase, but the synchrotron XRD was capable of distinguishing the two phases (see fig 5.3).

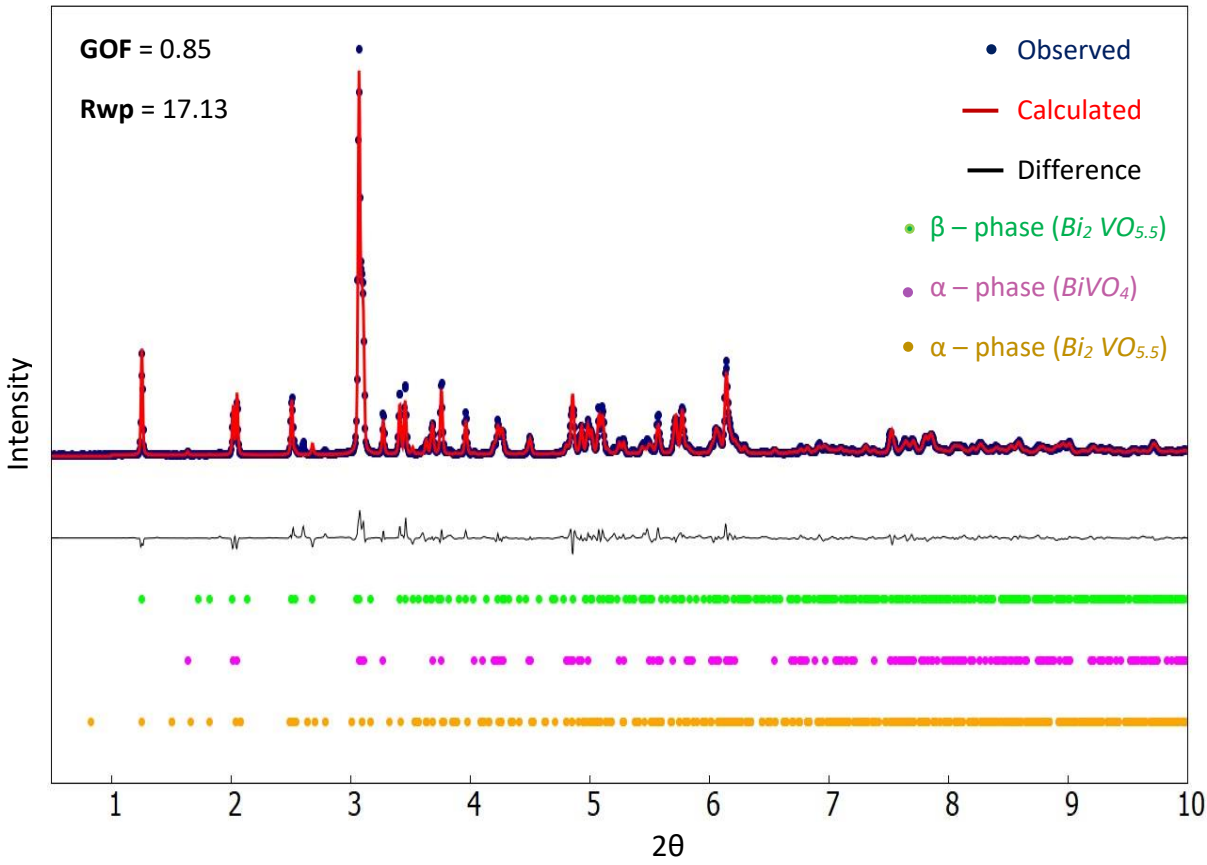

Figure 5.3: Synchrotron Rietveld refinement of cit-BiVO at room temperature.

5.3.2 cit-BiCe$_x$VO results

The PDF fits for cit-BiCe$_x$VO ($0.07 \leq x \leq 0.28$) samples had disorders and/or varying co-ordination. This is why the PDF fits were not particularly good and the local structures were not very representative of the average structure. The PDF data confirmed that the β-phase was the predominate and most stable phase at room temperature for doped samples. A much worser PDF fit was seen for cit-BiCe$_{0.07}$VO sample due to the discrepancy in the local structure variation or the presence of another phase (see fig 5.4).

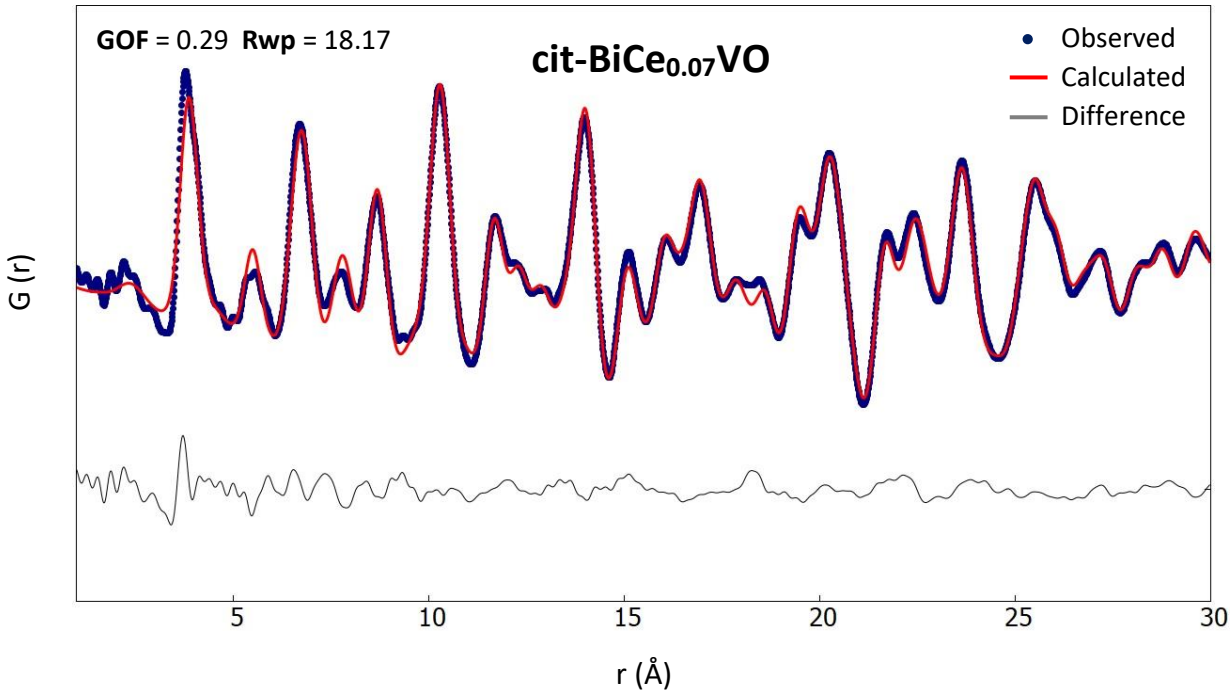

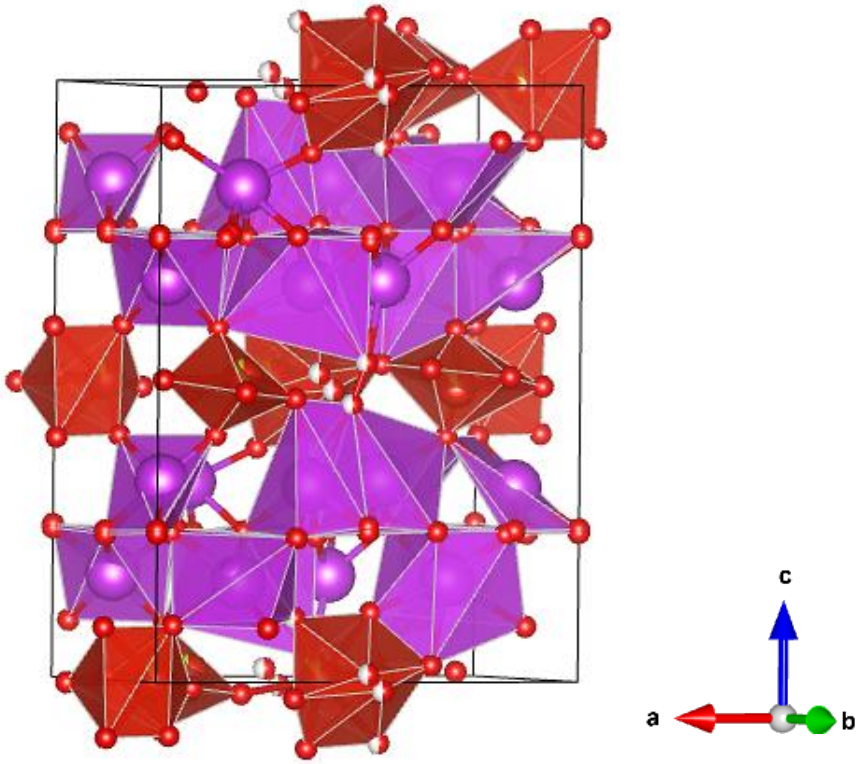

cit-BiCe$_{0.07}$VO β-phase

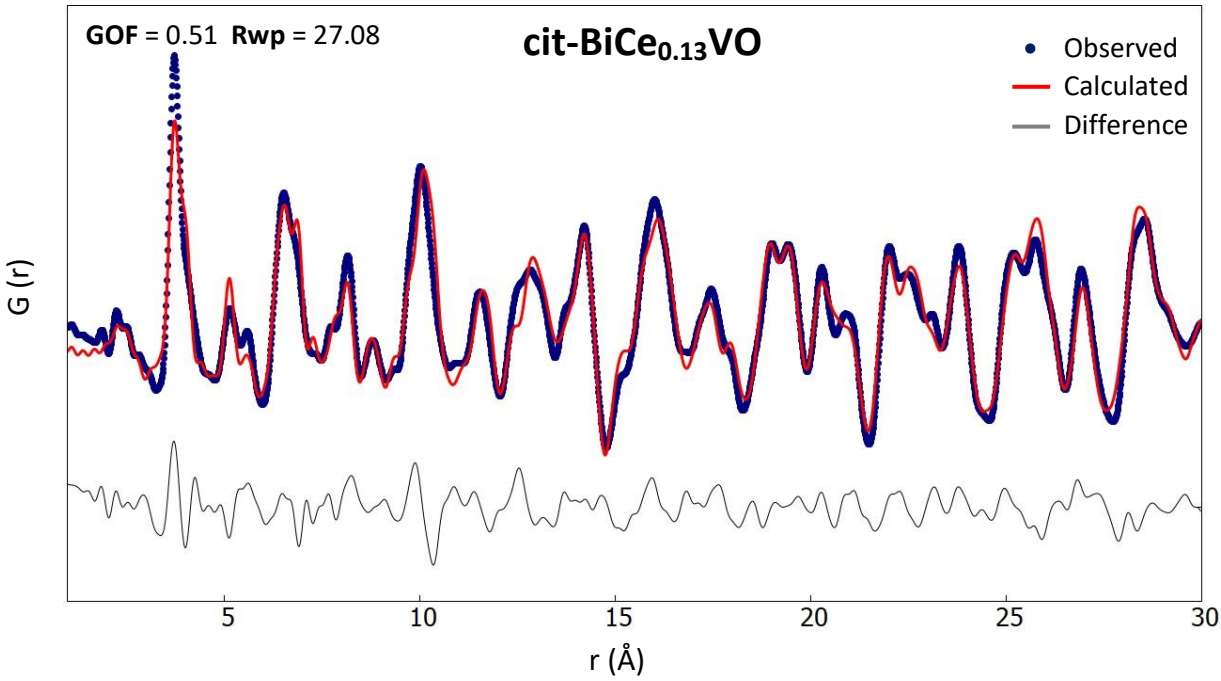

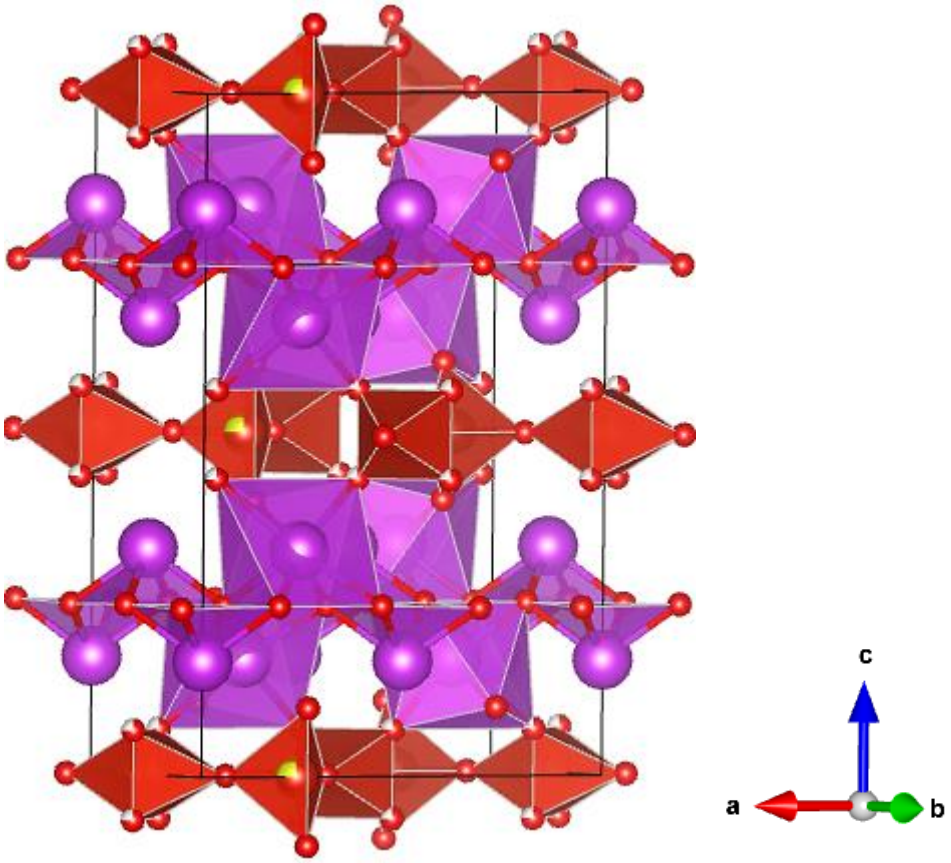

cit-$BiCe_{0.13}VO$ β-phase

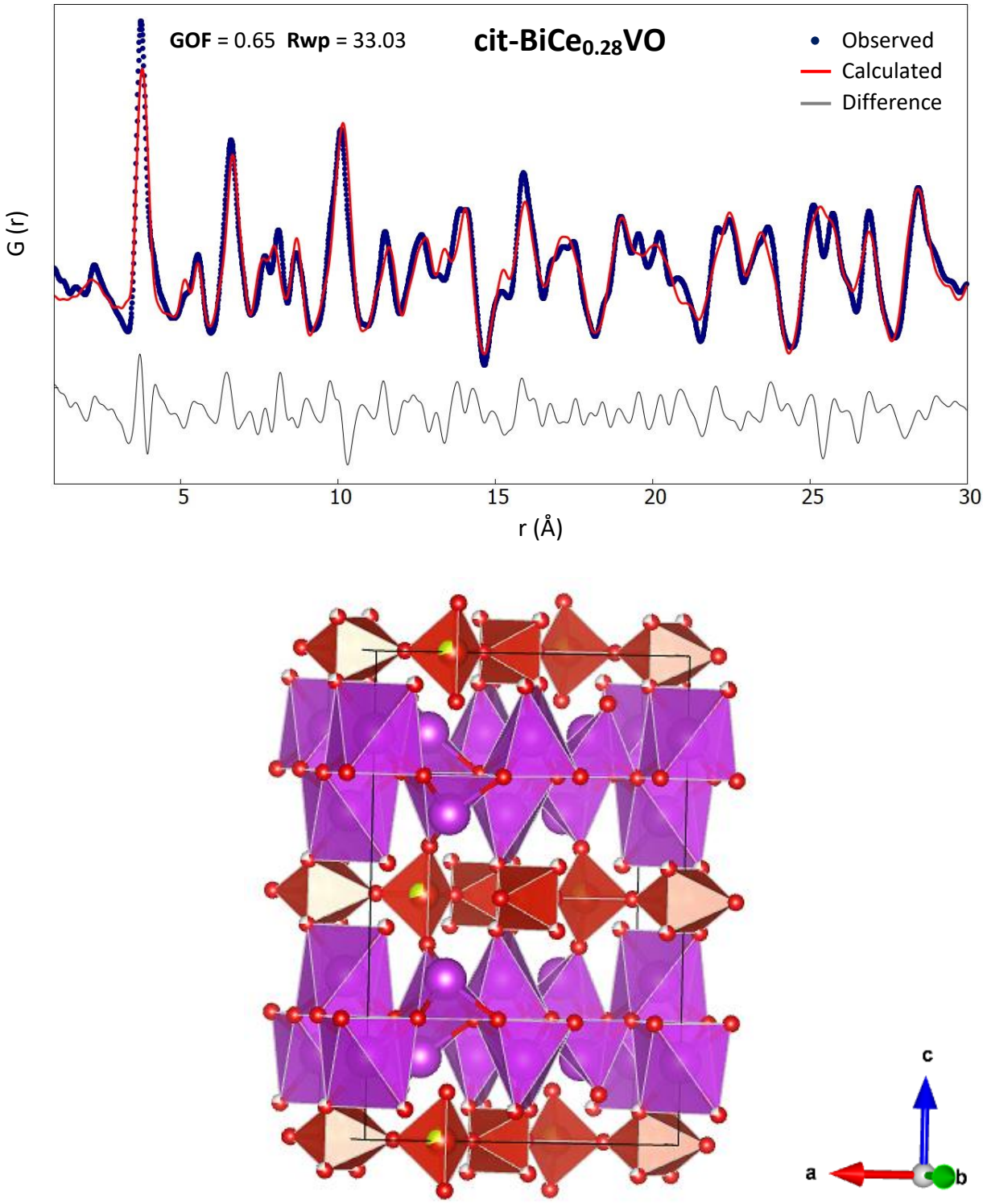

Figure 5.4: PDF patterns and crystal structures of cit-$BiCe_xVO$ (x = 0.07, 0.13 and 0.28) samples. The red/white spheres represent oxygen vacancy and red/yellow sphere represent V^{5+}/Ce^{4+} substitution.

Chapter 5

It was determined prior in chapter 3 using Lab PXRD patterns (Ref: fig.3.6) that the α-phase in cit-BiCe$_x$VO samples disappeared with increasing Ce^{4+} dopant concentrations. The synchrotron XRD data for cit-BiCe$_x$VO samples indicated a characteristic peak of the α-phase at 2θ ≈ 2° disappearing as Ce^{4+} concentration increased (see fig 5.6). The diagram in fig 3.7 shows the phase composition of cit-BiCe$_x$VO samples changing with increasing Ce^{4+} concentration.

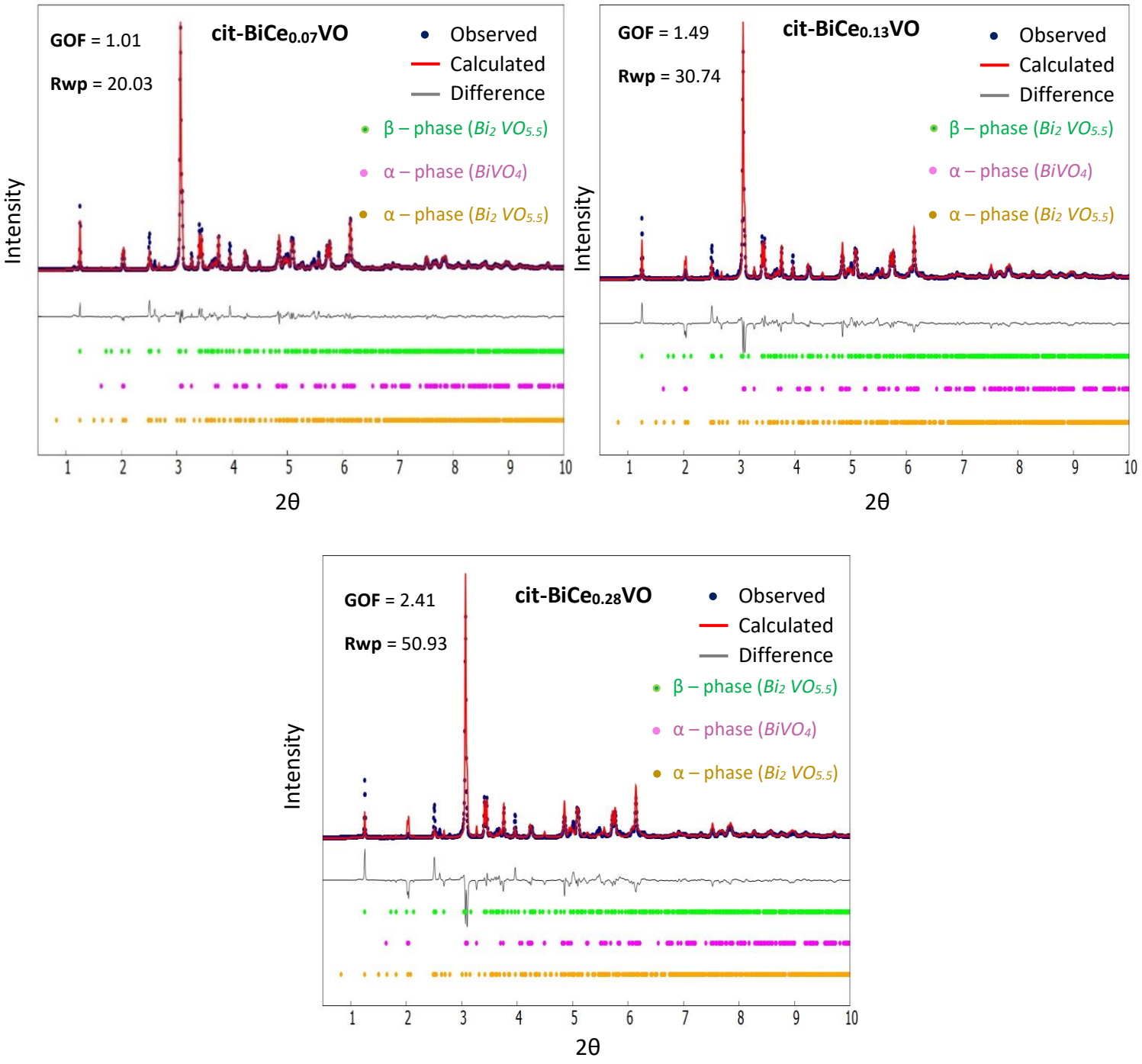

Figure 5.5: Synchrotron XRD patterns of cit-BiCe$_x$VO (0 ≤ x ≤ 0.28) samples.

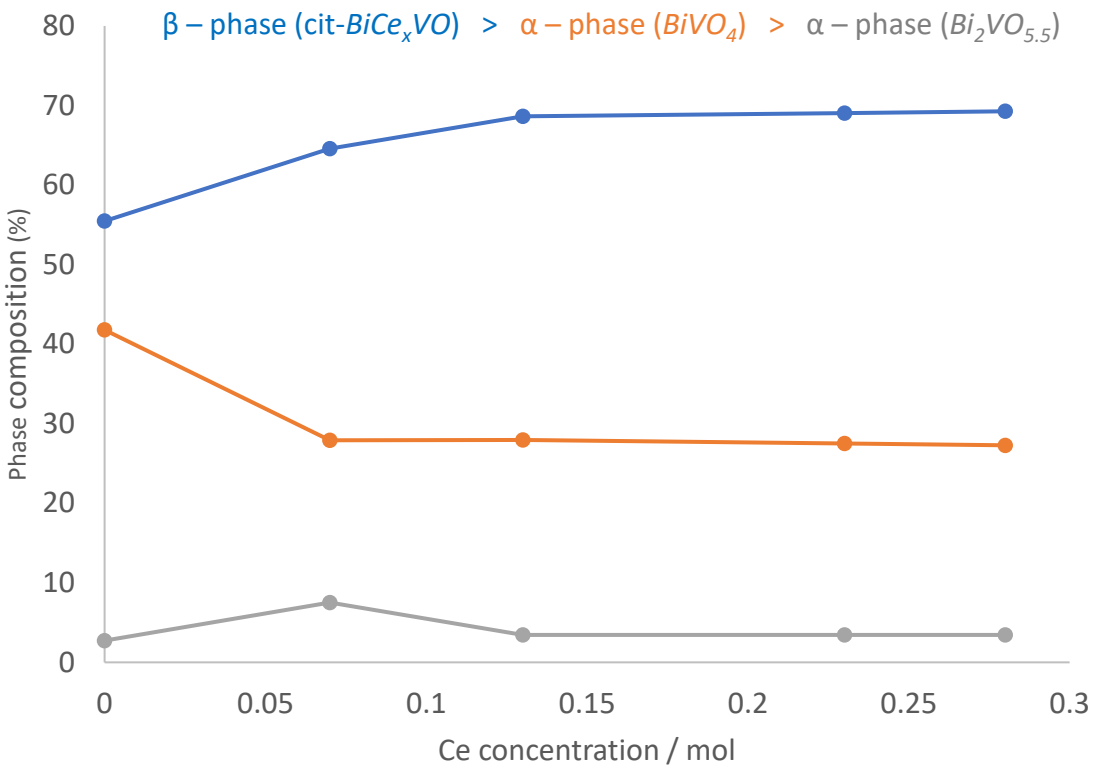

Figure 5.6: Synchrotron XRD showing room temperature phase composition of cit-$BiCe_xVO$ ($0.04 \leq x \leq 0.28$) samples with increasing Ce^{4+} concentration.

5.3.2 sol-$BiCu_{0.10}VO$ and sol-$BiCu_{0.10}Ce_{0.10}VO$ results

Previous chapters in this work have indicated that Ce^{4+} doping destabilized the crystal structure of sol-$BiCu_{0.10}VO$ and the Raman spectrum showed that sol-$BiCu_{0.10}Ce_{0.10}VO$ had high distortion of the VO_4 stretch modes and the intensity of the dominant band at 820 cm^{-1} assigned to the V-O tetrahedra structure was significantly reduced. The Arrhenius plot also showed that the ionic conductivity of the β-phase of sol-$BiCu_{0.10}VO$ was decreased by 11% between 300 °C – 600 °C when Ce^{4+} was substituted into the material.

The synchrotron XRD data assured this project an important feature which was observed that both sol-$BiCu_{0.10}VO$ and sol-$BiCu_{0.10}Ce_{0.10}VO$ samples had very negligible formation of the α-phase ($BiVO_4$) and only when these samples were synthesized using the citrate method the α-phase was detected. Fig 5.7 shows the PDF measurement of sol-$BiCu_{0.10}Ce_{0.10}VO$ which was not significantly different to sol-$BiCu_{0.10}VO$.

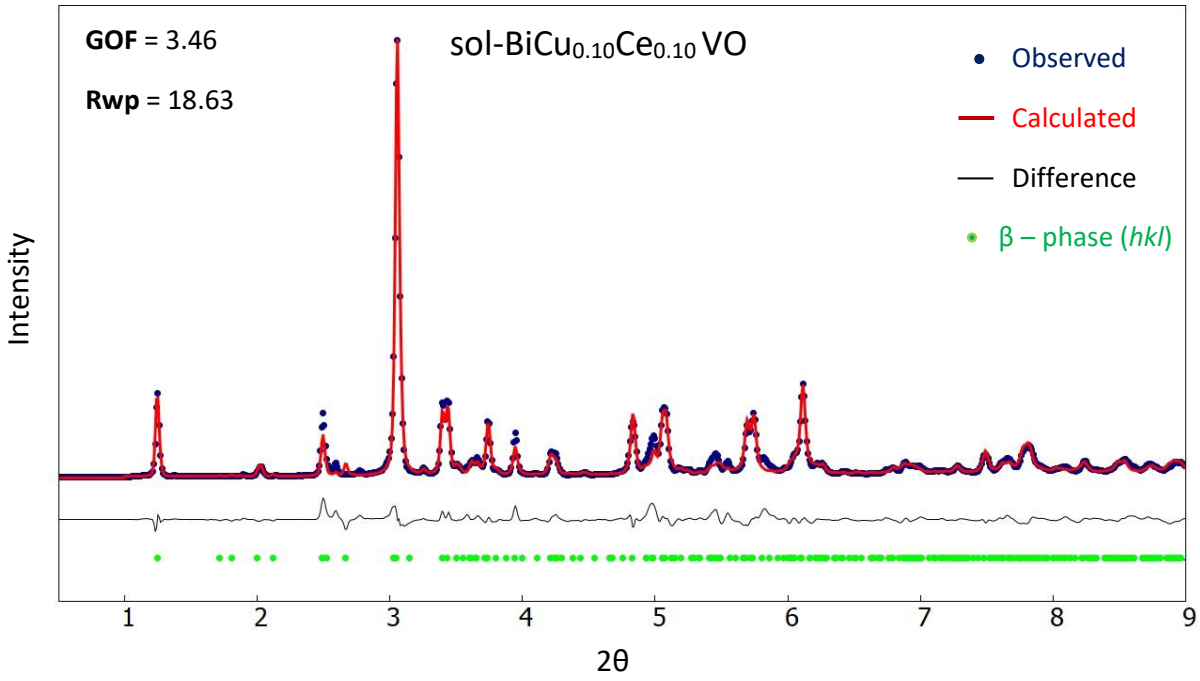

Figure 5.7: Synchrotron XRD Rietveld refinement of cit-$BiCu_{0.10}Ce_{0.10}VO$ at room temperature.

The PDF measurement of sol-$BiCu_{0.10}Ce_{0.10}VO$ was difficult to refine and in general all local structures are complex and difficult to refine. Fig 5.8 shows the PDF of sol-$BiCu_{0.10}Ce_{0.10}VO$ and the local crystal structure determined.

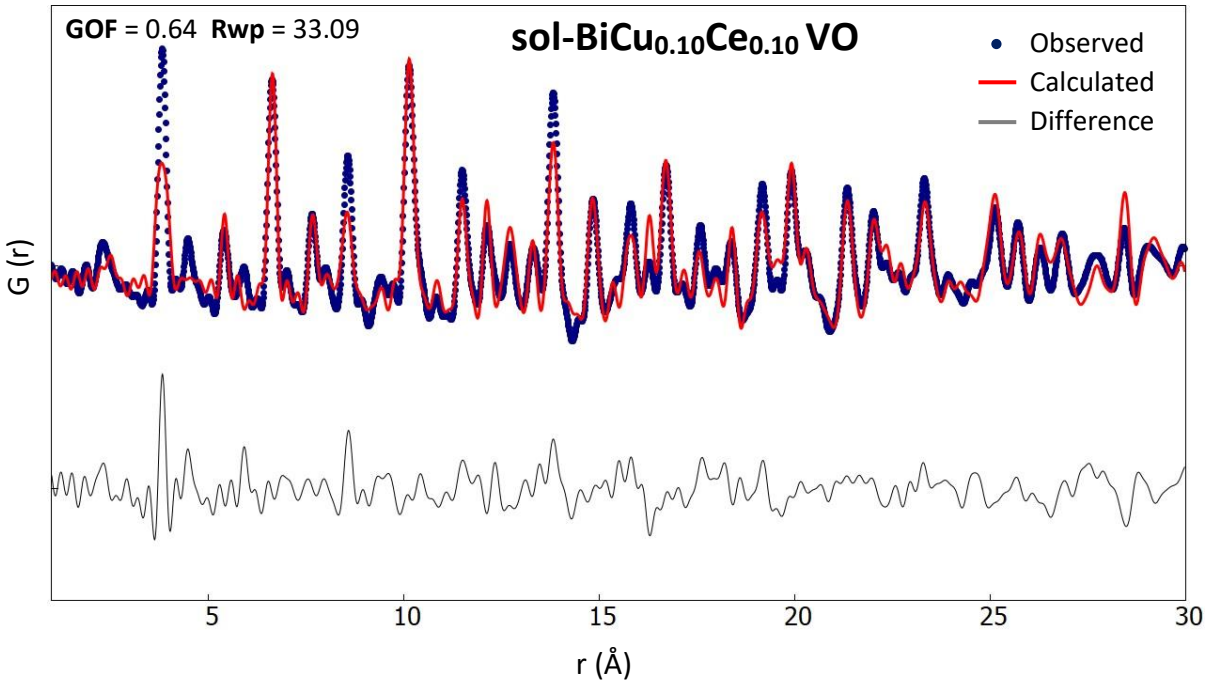

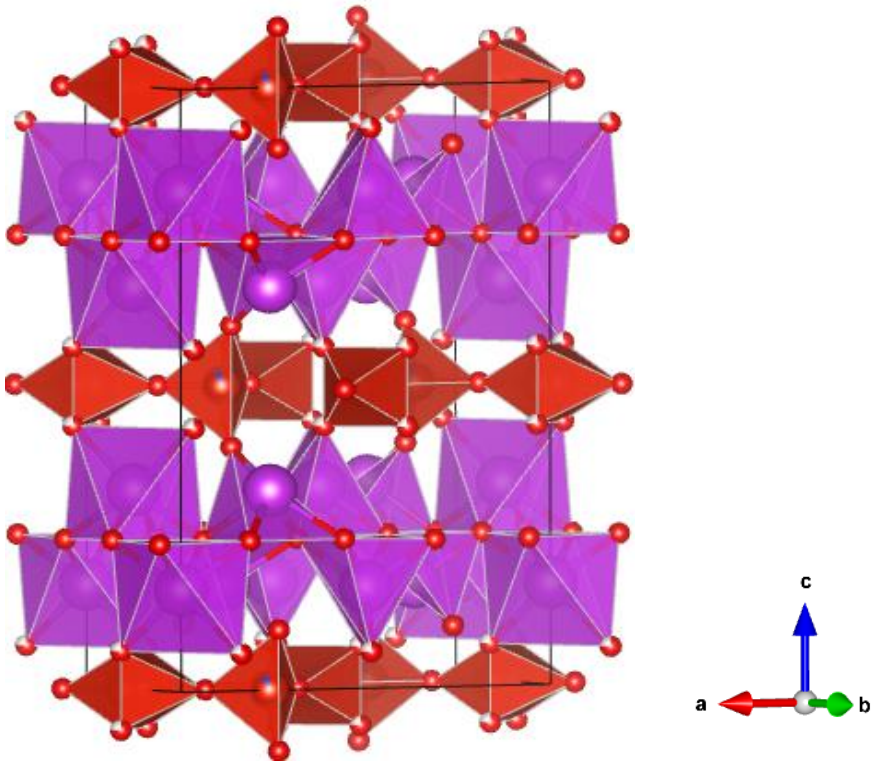

sol-$BiCu_{0.10}Ce_{0.10}VO$ β-phase

Figure 5.8: PDF analysis and crystal structure of sol-$BiCu_{0.10}Ce_{0.10}VO$. The red/white spheres represent oxygen vacancy and red/blue spheres represent V^{5+},Cu^{2+} and Ce^{4+} substitution.

5.4 Conclusion.

In conclusion, the synchrotron XRD data complemented the Lab D2 XRD data and detected some features which were not observed with the Lab D2 XRD such as the presence of the α-phase with the chemical composition of $Bi_2VO_{5.5}$. Cit-$BiCe_{0.07}VO$ sample had the worse PDF fit due to the high discrepancy in the local structure variation or the presence of another phase. In general, the local crystal structures were fairly estimated and reflected the average structures to some extent. Sol-$BiCu_{0.10}VO$ had better ionic conductivity compared to sol-$BiCu_{0.10}Ce_{0.10}VO$ due to the sample poor crystallinity and even though the two local crystal structure are remarkably similar, there is a factor that affect sol-$BiCu_{0.10}Ce_{0.10}VO$ poor conductivity other than the sample poor crystallinity.

Chapter 6

Conclusion.

cit-BiVO sample was determined to exhibit two phases at room temperature the α- and β-phases. The α-phase was the undesired phase due to the material low ionic conductivity. Additional, two different α-phases were identified with different chemical compositions $BiVO_4$ and $Bi_2VO_{5.5}$ using synchrotron radiation XRD data. It was also noted that cit-BiVO had reversable phase transitions from α → β → γ phases with thermal cycles.

When cit-BiVO was doped with increasing amount of Ce^{4+} concentrations to produce cit-$BiCe_xVO$ samples, the α-phase gradual disappeared and the γ-phase was stabilized. The STA indicated that doped samples also had reversible phase transition from α → β → γ phases with heating/cooling cycles and even less energy was required to transition from the β → γ phase. It was determined that the γ-phase was only stabilized at higher temperatures (>600 °C) and the *c*- and *a*-lattice parameters were the most affected compared to the *b*-lattice parameter.

The hypothesis for this study was proven to be correct, doping Ce^{4+} into cit-BiVO improved the electrolyte ionic conductivity (see fig 6.1). In the diagram, cit-$BiCe_xVO$ ($0.04 \leq x \leq 0.28$) samples had higher conductivity than undoped cit-BiVO except for cit-$BiCe_{0.18}VO$ which was treated as an outlier and more work needs to be done. In addition, it was observed that sol-$BiCu_{0.10}Ce_{0.10}VO$ and sol-$BiCu_{0.10}VO$ samples had comparable conductivity on the cooling cycle.

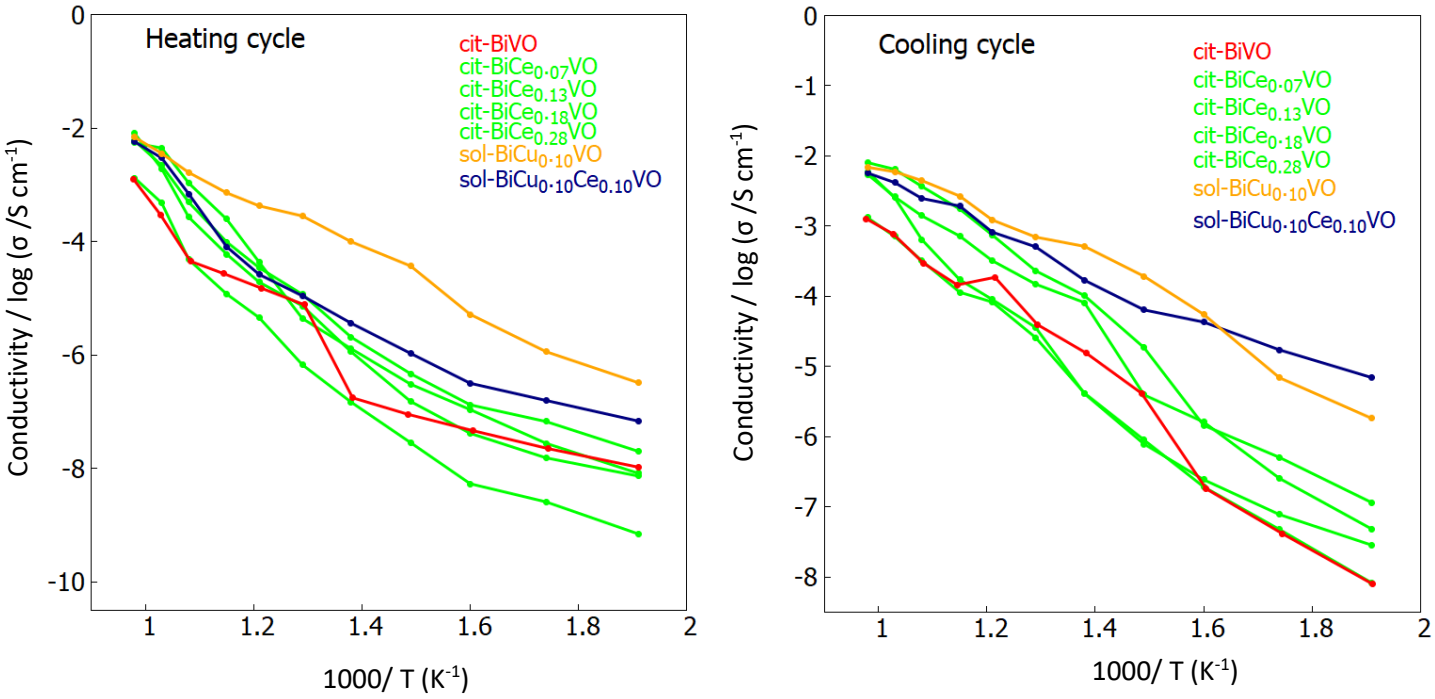

Figure 6.1: Arrhenius plots of cit-BiVO, cit-$BiCe_xVO$ ($0.07 \leq x \leq 0.28$), sol-$BiCu_{0.10}VO$ and sol-$BiCu_{0.10}Ce_{0.10}VO$ samples.

$Bi_2Cu_{0.10}V_{0.95}O_{5.5}$ was doped with 10% mol Ce^{4+} using the solid-state method to improve the material ionic conductivity. The solid-state procedure proved to reduce the presence of the formation of the α-phase ($BiVO_4$). The Raman and Arrhenius plots indicated that sol-$BiCu_{0.10}Ce_{0.10}VO$ had reduced conductivity and poor crystalline showing that sol-$BiCu_{0.10}VO$ was already a good ionic conducting material and any further doping either will reduce or have no effect on the material conductivity.

The effect of doping Ce^{4+} into cit-BiVO and sol-$BiCu_{0.10}VO$ samples was revealed in this project and future studies will involve doping cit-BiVO with a different rare earth metal e.g. Sm^{3+} using the solid-state method since it has been proven to minimize the presence of the unwanted phase. Techniques such as variable temperature (VT)-PDF and VT-XRD would be incorporated highly in the next project to increase our understanding in phase transition behaviour with changing temperatures.

Reference list

Chapter 1

1. Gür TM. Review of electrical energy storage technologies, materials and systems: Challenges and prospects for large-scale grid storage. *Energy Environ Sci*. 2018;11(10):2696-2767. doi:10.1039/c8ee01419a

2. www.worldometers.info. (n.d.). World Energy Statistics - Worldometer. [online] Available at: https://www.worldometers.info/energy/.

3. Taninouchi Y. High Oxide-Ion Conductivity and Phase Transition of Doped Bismuth Vanadate. *Mater Sci*. Published online 2010.

4. Chapter 4 high pressure investigation on nano. Published online 1997:102-123.

5. Sammes NM, Tompsett GA, Naefe H, Aldinger F. ChemInform Abstract: Bismuth Based Oxide Electrolytes - Structure and Ionic Conductivity. *ChemInform*. 2010;30(36):no-no. doi:10.1002/chin.199936284

6. Irshad M, Siraj K, Raza R, et al. applied sciences A Brief Description of High Temperature Solid Oxide Fuel Cell ' s Operation , Materials , Design , Fabrication Technologies and Performance. Published online 2016. doi:10.3390/app6030075

7. Zhang Y, Knibbe R, Sunarso J, et al. Recent Progress on Advanced Materials for Solid-Oxide Fuel Cells Operating Below 500 °C. *Adv Mater*. 2017;29(48). doi:10.1002/adma.201700132

8. Zhao F, Chen F, Li L, Xia C, Zhang L. Sm0.2Ce0.8O1.9/Y0.25Bi0.75O1.5 bilayered electrolytes for low-temperature SOFCs with Ag-Y0.25Bi0.75O1.5 composite cathodes. *Solid State Ionics*. 2010;192(1):557-560. doi:10.1016/j.ssi.2010.06.015

9. Li T, Liu W, Hou H, Shi Q, Han P, He S. Effects of dopant ions on the conductivity of Ce0.75Sm0.2M0.05O1.875 (M = Al, Fe, Y, Bi) electrolytes. *J Mater Sci Mater Electron*. 2018;29(14):12429-12435. doi:10.1007/s10854-018-9359-7

10. Singhal SC. Advances in SOFC technology. *Elsevier Sci*. 2000;(135):305-313.

References

11. Arora N, Deo G, Wachs IE, Hirt AM. Surface Aspects of Bismuth – Metal Oxide Catalysts. 1996;13(0058):1-13.

12. Dunstan MT, Halat DM, Tate ML, Evans IR, Grey CP. Variable-Temperature Multinuclear Solid-State NMR Study of Oxide Ion Dynamics in Fluorite-Type Bismuth Vanadate and Phosphate Solid Electrolytes. *Chem Mater*. 2019;31:1704-1714. doi:10.1021/acs.chemmater.8b05143

13. Mairesse G, Roussel P, Vannier RN, Anne M, Pirovano C, Nowogrocki G. Crystal structure determination of α, β and γ-Bi4V2O11 polymorphs. Part I: γ and β-Bi4V2O11. *Solid State Sci*. 2003;5(6):851-859. doi:10.1016/S1293-2558(03)00015-3

14. Wachs IE, Jefferson DA. Vanadium (V) Investigation Environments in Bismuth Vanadates : A Structural Using Raman Spectroscopy and Solid State 51V NMR. Published online 1991:194-210.

15. Beg S, Haneef S. Synthesis , phase stability and oxide ion conductivity of Ce (IV)– Cd (II) double substituted bismuth vanadate. *Phase Transitions*. 2015;88(11):1074-1085. doi:10.1080/01411594.2015.1039008

16. Baidya T, Bera P, Kröcher O, et al. Understanding the anomalous behaviour of Vegard's law in Ce1-: XMxO2 (M = Sn and Ti; 0 < x ≤ 0.5) solid solutions. *Phys Chem Chem Phys*. 2016;18(20):13974-13983. doi:10.1039/c6cp01525e

17. Beg S, Al-Areqi NAS. Composition dependence of polymorphism and electrical conductivity in Ce(IV)-doped Bi4V2O11. *Philos Mag*. 2009;89(15):1279-1294. doi:10.1080/14786430902939396

18. Donaldson, E.C., Alam, W. and Begum, N. (2013). Hydraulic Fracturing Explained. Hydraulic Fracturing Explained, pp.1–22.

Chapter 2

1. Liu X. Defect Structure in Yttrium , Niobium and Lead Substituted Bismuth Oxide Solid Electrolytes. 2009;(September).

References

2. Investigation S. A Mössbauer Spectroscopy Investigation of Fe enriched WC-Co Adeleke Wasiu Sufianu. Published online 2016.

3. Vogel S, Ehm L, Knorr K, Braun G. Automated processing of 2D powder diffraction data. *Adv X-ray Anal*. 2002;45(c):31-33. http://www.dxcicdd.com/01/PDF/D-012.pdf

4. Tripathy D, Pandey A. Studies on structural and optical properties and its correlation with the ionic conductivity of the Bi 2 VO 5 . 5 – based oxide ionic conductors. *Solid State Ionics*. 2019;341(July):115038. doi:10.1016/j.ssi.2019.115038

5. Stortelder JK. Ionic Conductivity in Yttria-Stabilized Zirconia Thin Films grown by Pulsed Laser Deposition. *Inorg Mater Sci*. 2005;(August). http://www.utwente.nl/tnw/ims/people/formerMSc/Jetske Stortelder.pdf

6. Bafrooei HB, Ebadzadeh T. MgAl2O4 nanopowder synthesis by microwave assisted high energy ball-milling. *Ceram Int*. 2013;39(8):8933-8940. doi:10.1016/j.ceramint.2013.04.089

7. Wachs IE, Jefferson DA. Vanadium (V) Investigation Environments in Bismuth Vanadates : A Structural Using Raman Spectroscopy and Solid State 51V NMR. Published online 1991:194-210.

8. Spectroscopy XIR. Xi. raman spectroscopy. Published online 2002:1-34.

9. Ferraro JR, Nakamoto K, Brown CW. *Introductory Raman Spectroscopy: Second Edition*.; 2003. doi:10.1016/B978-0-12-254105-6.X5000-8

10. Bordet P. Local structure studies using the pair distribution function. *EPJ Web Conf*. 2015;104. doi:10.1051/epjconf/201510401003

11. Petkov V, Billinge SJL, Larson P, et al. Structure of nanocrystalline materials using atomic pair distribution function analysis: Study of (formula presented). *Phys Rev B - Condens Matter Mater Phys*. 2002;65(9):1-4. doi:10.1103/PhysRevB.65.092105

12. Page K. Atomic Pair Distribution Function Analysis. *Phys Rev B*. 2007;76.

13. pdf “Analysis Chart.doc”.pdf. 2019;(July)

14 L. B. McCusker, a. R. (1999). Rietveld refinement guidelines. *J. Appl. Cryst.*, 36-50.

References

Chapter 3

1. Taninouchi Y. High Oxide-Ion Conductivity and Phase Transition of Doped Bismuth Vanadate. *Mater Sci*. Published online 2010.

2. Gu S, Li W, Wang F, Li H, Zhou H. Substitution of Ce(III,IV)ions for Bi in BiVO4and its enhanced impact on visible light-driven photocatalytic activities. *Catal Sci Technol*. 2016;6(6):1870-1881. doi:10.1039/c5cy01412c

3. Zhou D, Pang LX, Guo J, et al. Influence of Ce substitution for Bi in BiVO4 and the impact on the phase evolution and microwave dielectric properties. *Inorg Chem*. 2014;53(2):1048-1055. doi:10.1021/ic402525w

4. Beg S, Al-Areqi NAS. Composition dependence of polymorphism and electrical conductivity in Ce(IV)-doped Bi4V2O11. *Philos Mag*. 2009;89(15):1279-1294. doi:10.1080/14786430902939396

5. Bruker. DiffracPlus Topas: Topas 5 User Manual. Published online 2014.

6. Wachs IE, Jefferson DA. Vanadium (V) Investigation Environments in Bismuth Vanadates : A Structural Using Raman Spectroscopy and Solid State 51V NMR. Published online 1991:194-210.

7. Beg S, Haneef S. Synthesis , phase stability and oxide ion conductivity of Ce (IV)– Cd (II) double substituted bismuth vanadate. *Phase Transitions*. 2015;88(11):1074-1085. doi:10.1080/01411594.2015.1039008

8. Merupo VI, Velumani S, Ordon K, Errien N, Szade J, Kassiba AH. Structural and optical characterization of ball-milled copper-doped bismuth vanadium oxide (BiVO4). *CrystEngComm*. 2015;17(17):3366-3375. doi:10.1039/c5ce00173k

Chapter 4

1. Sammes NM, Tompsett GA, Naefe H, Aldinger F. ChemInform Abstract: Bismuth Based Oxide Electrolytes - Structure and Ionic Conductivity. *ChemInform*. 2010;30(36):no-no. doi:10.1002/chin.199936284

References

2. Beg S, Al-Areqi NAS. Composition dependence of polymorphism and electrical conductivity in Ce(IV)-doped Bi4V2O11. *Philos Mag*. 2009;89(15):1279-1294. doi:10.1080/14786430902939396

3. Guo X, Waser R. Electrical properties of the grain boundaries of oxygen ion conductors: Acceptor-doped zirconia and ceria. *Prog Mater Sci*. 2006;51(2):151-210. doi:10.1016/j.pmatsci.2005.07.001

4. Stortelder JK. Ionic Conductivity in Yttria-Stabilized Zirconia Thin Films grown by Pulsed Laser Deposition. *Inorg Mater Sci*. 2005;(August). http://www.utwente.nl/tnw/ims/people/formerMSc/Jetske Stortelder.pdf

5. Tripathy D, Pandey A. Studies on structural and optical properties and its correlation with the ionic conductivity of the Bi 2 VO 5 . 5 – based oxide ionic conductors. *Solid State Ionics*. 2019;341(July):115038. doi:10.1016/j.ssi.2019.115038

6. Beg S, Haneef S. Synthesis , phase stability and oxide ion conductivity of Ce (IV)– Cd (II) double substituted bismuth vanadate. *Phase Transitions*. 2015;88(11):1074-1085. doi:10.1080/01411594.2015.1039008

7. EC-Lab software, Analysis S, Process D. Software Analysis and Data Process. 2017;(January).

Chapter 5

1. Bordet P. Local structure studies using the pair distribution function. *EPJ Web Conf*. 2015;104. doi:10.1051/epjconf/201510401003

2. Toby BH, Egami T. Accuracy of pair distribution function analysis applied to crystalline and non-crystalline materials. *Acta Crystallogr Sect A*. 1992;48(3):336-346. doi:10.1107/S0108767391011327

3. Highlights O. xPDFsuite - an end-to end software solution for atomic pair distribution function analysis To request a license to download and use this so ware , please click on " Express Licensing ", create an account / log in if you do not have an account / are not lo. :1-3.

References

4. Bruker. DiffracPlus Topas: Topas 5 User Manual. Published online 2014.

5. Beg S, Al-Areqi NAS. Composition dependence of polymorphism and electrical conductivity in Ce(IV)-doped Bi4V2O11. *Philos Mag*. 2009;89(15):1279-1294. doi:10.1080/14786430902939396.